

Fatigue Failure Theory for Lithium Diffusion Induced Fracture in Lithium-Ion Battery Electrode Particles

Nima Noii^{a,1}, Dejan Milijasevic^b, Haim Waisman^c, Amirreza Khodadadian^{d,e}

^a Deutsches Institut für Kautschuktechnologie (DIK e.V.)
Eupener Straße 33, 30519 Hannover, Germany

^b Institute of Applied Mathematics
Leibniz Universität Hannover, Welfengarten 1, 30167 Hannover, Germany

^c Computational Mechanics Group
Department of Civil Engineering & Engineering Mechanics,
Columbia University, New York, USA

^d School of Computer Science and Mathematics
Keele University, Staffordshire, UK

^e Research Unit Machine Learning
Technische Universität Wien, Vienna, Austria

Published on 30th May 2024

Computer Methods in Applied Mechanics and Engineering

doi: <https://doi.org/10.1016/j.cma.2024.117068>

Volume 428, 1 August 2024, 117068

¹Corresponding author.

E-mail addresses: noii@ikm.uni-hannover.de (N. Noii); dejan.milijasevic@hotmail.de (D. Milijasevic); waisman@civil.columbia.edu (H. Waisman). a.khodadadian@keele.ac.uk (A. Khodadadian)

Fatigue Failure Theory for Lithium Diffusion Induced Fracture in Lithium-Ion Battery Electrode Particles

Nima Noii^{a,2}, Dejan Milijasevic^b, Haim Waisman^c, Amirreza Khodadadian^{d,e}

^a Deutsches Institut für Kautschuktechnologie (DIK e.V.)
Eupener Straße 33, 30519 Hannover, Germany

^b Institute of Applied Mathematics
Leibniz Universität Hannover, Welfengarten 1, 30167 Hannover, Germany

^c Computational Mechanics Group
Department of Civil Engineering & Engineering Mechanics,
Columbia University, New York, USA

^d School of Computer Science and Mathematics
Keele University, Staffordshire, UK

^e Research Unit Machine Learning
Technische Universität Wien, Vienna, Austria

Abstract

To gain better insights into the structural reliability of lithium-ion battery electrodes and the nucleation as well as propagation of cracks during the charge and discharge cycles, it is crucial to enhance our understanding of the degradation mechanisms of electrode particles. This work presents a rigorous mathematical formulation for a *fatigue failure theory for lithium-ion battery electrode particles* for lithium diffusion induced fracture. The prediction of fatigue cracking for lithium-ion battery during the charge and discharge steps is an particularly challenging task and plays an crucial role in various electronic-based applications. Here, to simulate fatigue cracking, we rely on the phase-field approach for fracture which is a widely adopted framework for modeling and computing fracture failure phenomena in solids. The primary goal here is to describe a variationally consistent energetic formulation for gradient-extended dissipative solids, which is rooted in incremental energy minimization. The formulation has been derived as a coupled system of partial differential equations (PDEs) that governs the gradient-extended elastic-chemo damage response. Additionally, since the damage mechanisms of the lithium-ion battery electrode particles result from swelling and shrinkage, an additive decomposition of the strain tensor is performed. Several numerical simulations with different case studies are performed to demonstrate the correctness of our algorithmic developments. Furthermore, we investigate the effect of randomly distributed micro cavities (voids) and micro notches on fracture resistance.

Keywords: Lithium-ion batteries, electrode particles, phase-field fracture, fatigue cracking, chemo-elasticity, multi-physics.

²Corresponding author.

E-mail addresses: noii@ikm.uni-hannover.de (N. Noii); dejan.milijasevic@hotmail.de (D. Milijasevic); waisman@civil.columbia.edu (H. Waisman). a.khodadadian@keele.ac.uk (A. Khodadadian)

Contents

1. Introduction	4
2. Phase-field modeling of fracture in lithium-ion battery electrode particles	10
2.1. Primary fields for the multi-field problem	11
2.2. Thermomechanical framework: Dissipation inequality and constitutive relations	12
2.3. Constitutive energy density functions for chemo-elasticity	14
2.3.1. Elastic contribution	14
2.3.2. Lithium-ion contribution	15
2.3.3. Fracture contribution	16
2.3.4. Energy quantities	17
2.4. Potential energy of the external loading	17
2.5. Dissipation for the rate of minimization principle	17
2.5.1. Lithium-ion concentration dissipation	18
2.5.2. Damage dissipation	19
2.6. Incremental energy, dissipation and load functionals for the reduced incremental minimization principle	24
2.6.1. Incremental energy	25
2.6.2. Incremental potential of external loading	25
2.6.3. Incremental dissipation-potential for lithium-ions diffusion	25
2.6.4. Incremental dissipation-potential for fracture	26
2.7. Variational equations through reduced incremental energy functional	27
2.7.1. Lithium-ion concentration flow	27
2.7.2. Elasticity	28
2.7.3. Damage	29
2.8. Variational formulations derived for the coupled multi-field problem	29
3. Numerical examples	30
3.1. Example 1: Lithium diffusion induced crack driven for single notch	32
3.2. Example 2: Lithium diffusion-induced crack driven for single notch with distributed micro cavities	33
3.3. Example 3: Lithium diffusion-induced crack driven for distributed micro notches	35
3.4. Example 4: Three-dimensional Lithium diffusion-induced crack driven for multiple distributed notches	38
3.4.1. Evaluation of using different multi-CPUs on computational time	41
4. Conclusion	49

1. Introduction

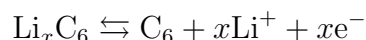
Lithium-ion batteries have been of great interest in both academia [1, 2], and industry [3, 4], due to their impressive combination of high energy density storage, rechargeable, low self-discharge rate, and versatility to use in various shapes and sizes to fit specific applications. These types of batteries are extensively utilized across a diverse range of electronic devices and systems, while their superior capacity to store and deliver energy efficiently makes them essential components in various applications.

The major applications for lithium-ion batteries cover different systems including portable electronic devices such as smartphones, laptops, and tablets, where compact and efficient power sources are crucial. Additionally, they play an important role in powering electric vehicles, providing the necessary energy storage for sustainable and eco-friendly transportation [5]. Furthermore, lithium-ion batteries find application in renewable energy systems, storing harvested energy from sources like solar panels for later use [6]. Their versatile nature extends to medical devices, aerospace technology, and numerous other fields where reliable and efficient power solutions are highly demanding [7].

In a lithium-ion battery, lithium-ions Li^+ transfer from the *anode* and diffuse through the electrolyte towards the *cathode* during *charge* and when the battery is *discharged*, the respective electrodes change their roles. We note that in the context of the lithium-ion battery the anode and cathode are the two electrodes that facilitate the flow of electric current during the processes of charging and discharging, see Figure 1.

In the charging process [8, 9] the following steps are essential:

- During the charging phase of a Lithium-ion battery, the Li^+ moves from the anode to the cathode.
- The anode is typically made of a material that can host Li^+ , such as graphite. For instance, Graphite, Lithium Titanate ($\text{Li}_4\text{Ti}_5\text{O}_{12}$), Silicon (Si), silicon alloys, and metal oxides (e.g., SnO_2 , Fe_3O_4) are among the materials that can be used for anode electrode [10]. When the battery is connected to an external voltage source, lithium atoms in the anode material lose electrons, forming Li^+ ions. Typical, chemical reactions that take place at the anode electrodes are:



We note that left to right indicates discharge while right to left indicates charge process.

- These Li^+ ions move through the electrolyte, which is usually a lithium salt dissolved in a solvent (commonly a mixture of ethylene carbonate and dimethyl carbonate). The electrolyte acts as a medium that allows the transport of ions.
- Next, the diffusion of Li^+ ions through the electrolyte will be occurred. This follows with a moment of Li^+ ions through the electrolyte due to a concentration gradient, in which the diffusion process is influenced by the type of electrolyte, and temperature.
- Then, the transport process through the separator material will happen. We note that, the electrolyte is separated from the cathode by a permeable material known as

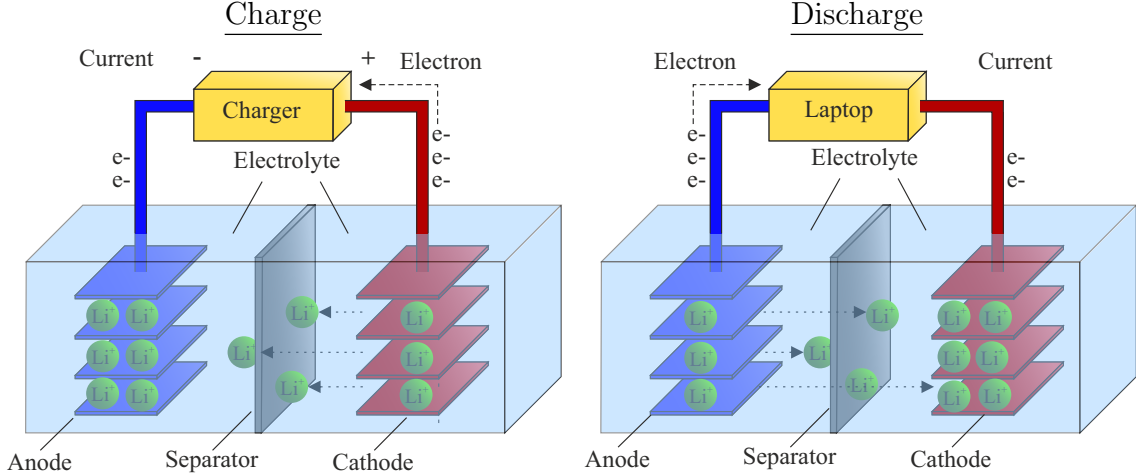
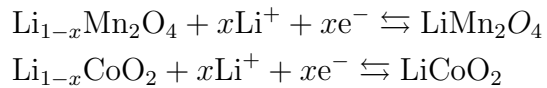


Figure 1: Charge/discharge process in lithium-ion battery. (i) During the charging process, lithium-ions (green circles) flow from the positive electrode (red) to the negative electrode (dark blue) through the electrolyte (light blue) and separator (gray). Electrons also flow from the positive electrode to the negative electrode. Electrons and ions combine at the negative electrode and deposit lithium there. (ii) When no more ions flow, the battery is fully charged and ready for use. (iii) During discharge, ions flow back through the electrolyte from the negative electrode to the positive electrode. Electrons flow through the negative electrode to the positive electrode and charge the laptop. When ions and electrons combine at the positive electrode, lithium is deposited there. (iv) When all the ions have flown back, the battery is completely discharged and needs to be recharged.

the separator (such as ceramic coated separators, polyethylene (PE), and polypropylene (PP)). Thus this prevents direct contact between the anode and cathode, avoiding short circuits [10]. So, Li^+ moves through the separator by the electric field created by the voltage difference between the anode and cathode. For instance, the typical chemical reactions that take place at the cathode electrodes are:



Similarly, left to right indicates discharge while right to left indicates charge process.

- In the final step, Li^+ will be reached to the cathode electrode thus we have cathode reactions. cathode material can be named as Lithium Cobalt Oxide (LiCoO_2), Lithium Manganese Oxide (LiMn_2O_4), and Lithium Iron Phosphate (LiFePO_4). In this step, Li^+ accepts electrons and then electrical energy in the form of chemical energy will be stored. The cathode is typically composed of a material capable of incorporating lithium-ions, such as lithium cobalt oxide (LiCoO_2) or lithium iron phosphate (LiFePo_4).

When the battery is discharging, the process is reversed. Li^+ ions move from the anode back to the cathode through the electrolyte and separator. At the anode, the material releases lithium-ions and electrons, then electrons flow through the external circuit, creating an electric current.

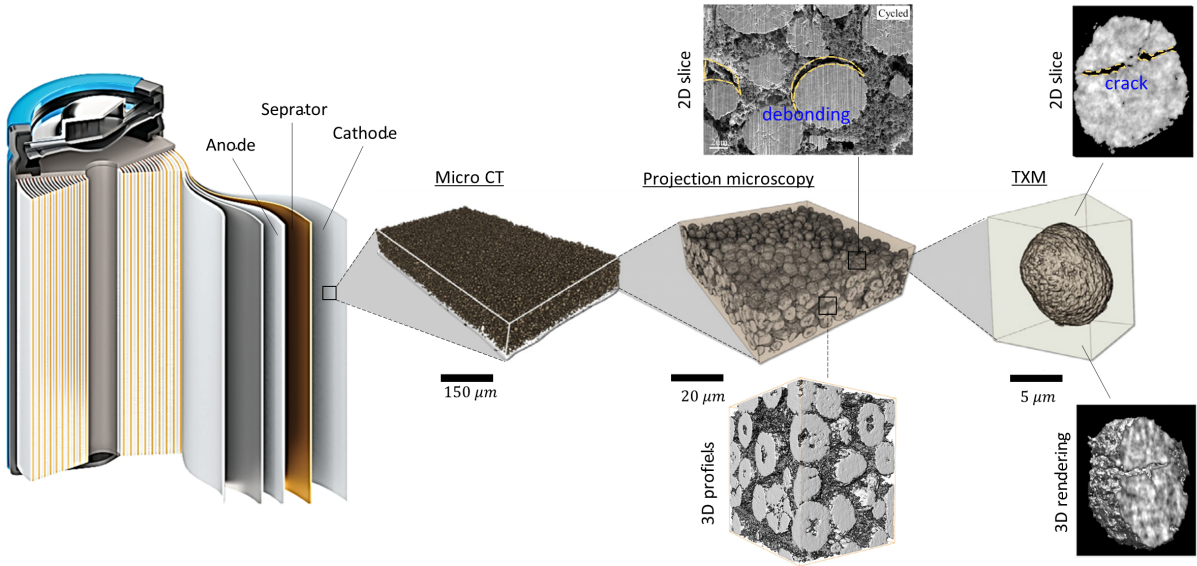


Figure 2: Multiple scales for cylindrical electrochemical cell illustrating the tomographic data from the composite film up to a unit active particle. By means of the stress concentration of lithium-ion over the electrode particle surface the cracks could be observed. The images are reproduced partly through [17, 18].

The degradation mechanisms induced by the process of lithiation pose a significant challenge for lithium-ion batteries, particularly those equipped with high-capacity electrodes such as silicon (Si). These degradation mechanisms, over time, have the potential to curtail the overall lifespan of the batteries [11]. The major issue lies in the fact that the lithiation process, while enhancing the battery's capacity, concurrently initiates mechanisms that can compromise its long-term durability and performance [12]. Addressing and mitigating these degradation factors is an important concern to enhance the longevity and reliability of lithium-ion batteries, especially those utilizing high-capacity materials.

A key factor contributing to the degradation mechanisms of electrochemical systems is the damage caused by electrode particles [13]. This fracture is a result of the stresses arising from the uneven expansion and contraction of electrode materials during the insertion and extraction of lithium-ions [14]. The fractures occurring in electrode particles have an important impact on battery performance and its efficiency. Firstly, the breakage disrupts the electronic connectivity between particles. This disruption leads to a decrease in the effective amount of active material available within a cell. This has a direct impact on the overall capacity and efficiency of the battery. Secondly, the fractures expose fresh surfaces on the electrode particles. These newly exposed surfaces become sites for additional parasitic side reactions [15]. One specific observation of this phenomenon is the formation and growth of the solid electrolyte interphase (SEI). The SEI is a layer that forms on the electrode surface and can detrimentally affect the performance of the battery [16]. So, the available amount of lithium within the system diminishes over time due to these additional reactions, further impacting the battery's overall efficiency and longevity.

A major degradation mechanism arises through *fatigue cracking* in lithium-ion battery electrode particles refers to the development of cracks within the electrode material over repeated charging and discharging cycles [19, 20]. This phenomenon is often observed

in high-capacity electrode materials, such as silicon, and it poses a significant challenge to the overall performance and lifespan of lithium-ion batteries. The repeated insertion and extraction of lithium-ions during charge and discharge processes cause significant volume changes in the electrode materials. In the case of silicon electrodes, for example, the material undergoes substantial expansion and contraction as it takes in and releases lithium-ions. This cyclic expansion and contraction can lead to mechanical stress and strain on the electrode particles [21]. Over time, the accumulated stress can surpass the material's structural tolerance, resulting in the initiation and propagation of microscopic cracks, known as fatigue cracks [20]. Figure (2) shows the fatigue cracking due to the stress concentration of lithium-ion over the electrode particle surface for a unit active particle through tomographic data from the composite film. These cracks can compromise the structural integrity of the electrode particles, leading to a decline in the overall capacity and efficiency of the battery.

The consequences of fatigue cracking in lithium-ion batteries are important aspects which have to be investigated. Firstly, the cracks create pathways for the electrolyte to penetrate deeper into the electrode material, increasing the risk of undesired side reactions and impairing the overall electrochemical performance of the battery. Secondly, the fractured particles may become detached from the electrode, leading to a loss of active material and a reduction in the overall capacity of the battery. Therefore, in the present study, fatigue failure theory for lithium diffusion induced fracture in lithium-ion battery electrode particles is investigated.

In the literature, often experimental investigation considering fracture-induced lithium concentration for lithium-ion battery electrode particles have been performed. The fracture pattern poses different crack nucleation and propagation due to micro cavities induced by lithium concentration, see Figure 3. Kabir et al. [22] offer a classification of degradation mechanisms and modes, accompanied by a brief overview of essential experimental techniques. Meanwhile, Hapuarachchi et al. [23] concentrate extensively on in situ experimental methods for evaluating anode degradation. The authors discussed that X-ray techniques furnish details on phase transformations, alterations in chemical states, and the creation of metastable phases within a Li^+ -ion battery. Concurrently, optical techniques unveil insights into the chemical composition of electrodes, and scanning probe microscopy techniques aid in tracking physical alterations within the electrodes. Accordingly, to predict the fracture mechanism in lithium-ion battery and further investigation numerical simulations are required.

In the literature, there are different numerical methods to perform degradation mechanisms due to lithiation or delithiation processes. Xu et al. [11] investigated on the application of cohesive zone models for the lithiation process of electrodes, wherein the crack path was predefined. Notably, these models have so far been employed solely for the examination of electrode particles during a singular charge or discharge step, neglecting the scenario in which these particles undergo cyclic loading and leads to fatigue damage. Ryu et al. [29] employed a linear fracture mechanics approach to examine the degradation behavior of silicon nanowires (Si-NWs) throughout the lithiation/delithiation process. Their study incorporated the analysis of substantial deformations related to lithiation, taking into account the influence of pressure gradients on the diffusion of lithium. Zhu et al. [30] investigated on the diffusion-induced stress and crack behaviour of Li^+ ion electrode particles were analyzed through the XFEM approach to study crack

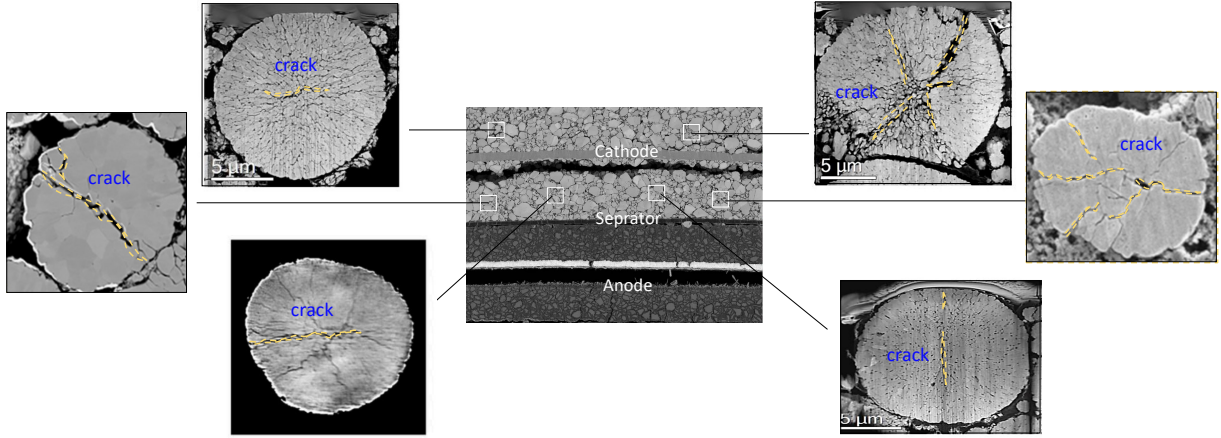


Figure 3: Zooming into the rolling cross-section of a lithium-ion battery reveals three key components: the cathode, separator, and anode. This visualization, captured using scanning electron microscopy (SEM) [24], depicts the intricate structure of the battery’s internal layers. By magnifying a virtual slice of this cross-section, complex cracking patterns in different directions can be observed, suggesting lithium diffusion within the cathode electrode itself. Cross-sectional SEM images for cathode electrode particles are reprinted from [25, 26, 27, 28].

propagation of primary particle. Thus, the stress degradation mechanisms due to the diffusion driven approach and chemical potential driven are considered.

The variational approach to fracture by Francfort and Marigo and the related regularized formulation [31], which is also commonly referred to as a phase-field model of fracture, see e.g., the review paper [32, 33, 34], is a widely accepted framework for modeling and computing the fracture failure phenomena in elastic solids. Thus, since the computational modeling of such complex behavior for fatigue cracking for lithium-Ion battery electrode particles is required, in this study the phase-field method of failure is used. Phase-field modeling is based on the regularization of sharp crack discontinuities by introducing an additional scalar field, which smoothly represents the transition between intact and cracking states, avoiding the use of complex discretization methods for crack discontinuities. Furthermore, it has shown great ability to describe crack initiation, propagation, branching and merging. Thus, it provides a powerful paradigm for computational fracture mechanics. The origin of the phase-field method is the variational formulation of the Griffith’s fracture [35] and its following regularization [36], in which the crack propagation is coupled with a critical value of the energy release rate. Based on this, many modifications have been developed with regard to special applications. The wide variety of phase-field fractures include for example thermal shocks and thermo-elastic-plastic solids [37, 38, 39], pressurized fractures [39, 40, 41, 42, 43], proppant-filled fractures [44], fluid-filled fractures [45, 46, 47, 48, 49, 50, 51], dynamic fracture [52, 53, 54, 55], ductile fracture [56, 57, 58, 59], cohesive fracture [60, 61, 62], fractures in functionally graded materials, composites [63, 64], and providing detailed programming implementation code for phase-field fracturing [65, 66, 67, 68, 69].

As an alternative approach, phase-field modeling of fracture is used to model degradation mechanism due to lithiation process in lithium-ion battery. Zhao et al. [70] investigated into the electrochemical reactions in lithium-ion batteries by employing a fracture-

coupled anisotropic Cahn-Hilliard-type diffusion in their phase-field model of fracture. Zhang et al. [71] formulated a chemo-mechanical coupled computational framework to capture large plastic deformation induced by diffusion and phase-field model for silicon (Si) electrodes. Xu et al. [72] explored the fracture mechanisms of cylindrical electrode particles, employing a finite strain phase-field model of fracture model that considered phase segregation and electrochemical reactions on both particle and fracture surfaces. Recently, Rezaei et al. [73] investigated a cohesive phase-field fracture model for chemo-mechanical environments in battery materials. In their study, the role of different coupling terms and their impact on the obtained results is investigated while the influence of the stress field as well as the damage variable on the flux vector due to concentration-dependent fracture properties is presented.

Despite many investigations on degradation mechanisms of lithium diffusion induced fracture for lithium-ion battery electrode, fatigue cracking has seldom been considered. Nonetheless, it is still not clear how the development of cracks within the electrode material over repeated charging and discharging cycles has to be predicted. So, the present contribution is aimed at investigating a rigorous mathematical formulation for *fatigue failure theory in lithium-ion battery electrode particles* for lithium diffusion induced fracture. The prediction of fatigue cracking for lithium-ion battery during the charge and discharge step is an intriguingly challenging task and plays an extremely important role in various electronic-based applications. In this study, we present a variational formulation for the charge and discharge cyclic process, based on variational principles, rooted in incremental energy minimization, for gradient-extended dissipative solids [74]. So, the first objective here, is to describe a variationally consistent energetic formulation has been derived to a coupled system of PDEs that governs the gradient-extended elastic-chemo damage response. In fact, this study is an extension of the previous work given in [20] toward presenting fatigue cracking by a variationally consistent energetic formulation for gradient-extended dissipative solids, which is rooted in incremental energy minimization in lithium-ion battery electrode particles. Additionally, here logarithmic non-negative fatigue degradation function as compared to the asymptotic version given in [20] for fatigue formulation has been used. It is trivial that, the asymptotic formulation delivers an asymptotically vanishing value while the latter logarithmic one vanishes for a finite value. Also, the slope of the logarithmic function used here can be tuned by varying giving a further degree of freedom when simulating real material behaviors. Additionally, based on the gradient theories of standard dissipative solids in chemo-elasticity media, the first-order spatial gradient of the primary fields that describe the evolving dissipative mechanism are further elaborated. These constitutive functions results in a compact variational formulation, thus yielding in a theoretical development of incremental minimization and saddle point principles for a class of gradient-type dissipative materials that incorporate multi-field boundary value problems.

Afterward, the governing equations are derived from rate-type variational principles, namely, the principle of virtual power. The coupling of chemical lithium concentration to the crack phase-field is achieved by a constitutive work density function, which is characterized by a degraded stored elastic energy and the accumulated dissipated energy due to lithium concentration and damage. Thus, the presented framework in this manuscript resulting in greater flexibility at the cost of a convenient mathematical structure. To accelerate fatigue crack analysis in this complex multi-field problem, we employed High-Performance Computing (HPC) with MPI parallelization. This approach distributes the

computational load across multiple cores, significantly speeding up the fatigue failure analysis. Finally, the following novelties of this manuscript can be summarized as:

- To develop new minimization and saddle point principles for the coupled problem of chemo-mechanical model undergoing fatigue failure;
- To derive rate-type mixed variational potential and reduced form to the minimization principle to a characteristic four field saddle point principle;
- To derive a variationally consistent energetic formulation rooted in incremental energy minimization, for gradient-extended dissipative solids in degraded lithium-ion battery electrode particles;
- High-performance computing is employed for fatigue response. Here, the Krylov method is used through a generalized minimal residual method (GMRES) with LU factorization as a preconditioner.
- Two- and three-dimensional boundary value problems are investigated to observe the influence of the randomly distributed micro cavities, and micro notches in electrode particles.

The paper is structured as follows. In Section 2, a mathematical formulation for fatigue cracking in lithium-ion battery electrode particles is presented in a variational setting, making use of incremental energy minimization. The degradation mechanisms resolved through phase-field modeling of fracture. The resulting framework is algorithmically described in detail. In Section 3, four numerical simulations with different case studies in two- and three-dimensional settings are performed to demonstrate the correctness of our algorithmic developments. Finally, the conclusion with some remarks and suggestions for future research are provided.

2. Phase-field modeling of fracture in lithium-ion battery electrode particles

In this part, we provide fatigue failure theory for chemo-elasticity media induced fracturing response. This includes the coupling of the deformation field, lithium diffusion, and phase-field fracture model to describe fatigue damage mechanisms. Here, the phase-field framework is aimed for regularizing sharp interfaces, consisting of incorporating a continuous field variable – the so-called order parameter – denoted by d which differentiates between multiple physical phases within a given system through a smooth transition. The coupling of elasticity to the crack phase-field is achieved by a constitutive work density function, which is characterized by a degraded stored elastic energy and the accumulated dissipated energy due to the damage.

Three governing equations corresponds to our multi-fields problem are employed to characterize the constitutive formulations for the mechanical deformation, lithium chemical potential, as well as the fracture phase-field. We describe strong and variational formulations of the coupled multi-physics system in both rate-type and incremental framework for gradient-extended standard dissipative solids.

2.1. Primary fields for the multi-field problem

Let $\mathcal{B} \subset \mathbb{R}^\delta$ be an arbitrary solid domain, $\delta = \{2, 3\}$ with a smooth boundary $\partial\mathcal{B}$ (Figure 4). We assume Dirichlet boundary conditions on $\partial_D\mathcal{B}$ and Neumann boundary conditions on $\partial_N\mathcal{B} := \Gamma_N \cup \mathcal{C}$, where Γ_N denotes the outer domain boundary and $\mathcal{C} \in \mathbb{R}^{\delta-1}$ is the crack boundary, as illustrated in Figure 4(b). The response of the fracturing solid at material points $\mathbf{x} \in \mathcal{B}$ and time $t \in \mathcal{T} = [0, T]$ is described by the displacement field $\mathbf{u}(\mathbf{x}, t)$ and the crack phase-field $d(\mathbf{x}, t)$ as

$$\mathbf{u} : \begin{cases} \mathcal{B} \times \mathcal{T} \rightarrow \mathbb{R}^\delta \\ (\mathbf{x}, t) \mapsto \mathbf{u}(\mathbf{x}, t) \end{cases} \quad \text{and} \quad d : \begin{cases} \mathcal{B} \times \mathcal{T} \rightarrow [0, 1] \\ (\mathbf{x}, t) \mapsto d(\mathbf{x}, t) \end{cases}. \quad (1)$$

Intact and fully fractured states of the material are characterized by $d(\mathbf{x}, t) = 0$ and $d(\mathbf{x}, t) = 1$, respectively. In order to derive the variational formulation, the following space is first defined. For an arbitrary $A \subset \mathbb{R}^\delta$, we set

$$H^1(\mathcal{B}, A) := \{v : \mathcal{B} \times \mathcal{T} \rightarrow A : v \in H^1(A)\}. \quad (2)$$

We also denote the vector valued space $\mathbf{H}^1(\mathcal{B}, A) := [H^1(\mathcal{B}, A)]^\delta$ and define

$$\mathcal{W}_{\bar{\mathbf{u}}}^{\mathbf{u}} := \{\mathbf{u} \in \mathbf{H}^1(\mathcal{B}, \mathbb{R}^\delta) : \mathbf{u} = \bar{\mathbf{u}} \text{ on } \partial_D^{\mathbf{u}}\mathcal{B}\}. \quad (3)$$

Concerning the crack phase-field, we define

$$\mathcal{W}^d := H^1(\mathcal{B}) \quad \text{and} \quad \mathcal{W}_{d_n}^d := \{d \in H^1(\mathcal{B}, [0, 1]) : d \geq d_n\}, \quad (4)$$

where d_n is the damage value in a previous time instant. Note that $\mathcal{W}_{d_n}^d$ is a non-empty, closed and convex subset of \mathcal{W}^d , and introduces the evolutionary character of the phase-field, incorporating an irreversibility condition in incremental form. Additionally, to formulate a chemo-mechanical model that undergoes fatigue failure, we require to define lithium concentration field $c(\mathbf{x}, t)$ and lithium chemical potential field $\mu(\mathbf{x}, t)$ as:

$$c : \begin{cases} \mathcal{B} \times \mathcal{T} \rightarrow \mathcal{R} \\ (\mathbf{x}, t) \mapsto c(\mathbf{x}, t) \end{cases} \quad \text{and} \quad \mu : \begin{cases} \mathcal{B} \times \mathcal{T} \rightarrow \mathcal{R} \\ (\mathbf{x}, t) \mapsto \mu(\mathbf{x}, t) \end{cases}. \quad (5)$$

So, the lithium chemical potential field is defined in the following space:

$$\mathcal{W}_{\bar{\mu}}^{\mu} := \{H^1(\mathcal{B}) : \mu = \bar{\mu} \text{ on } \partial_D^{\mu}\mathcal{B}\}, \quad (6)$$

and for the variation of lithium concentration mass content (or also named as the relative change of lithium concentration content), we consider the following space:

$$\mathcal{W}^c := \{H^1(\mathcal{B}) : c = \bar{c} \text{ on } \partial_D^c\mathcal{B}\}. \quad (7)$$

The gradient of the displacement field in the infinitesimally small deformation defines the symmetric strain tensor of the geometrically linear theory as

$$\boldsymbol{\varepsilon} = \nabla_s \mathbf{u} = \text{sym}[\nabla \mathbf{u}] := \frac{1}{2}[\nabla \mathbf{u} + \nabla \mathbf{u}^T]. \quad (8)$$

In view of the small strain hypothesis, the total strain tensor is additively decomposed into an elastic part $\boldsymbol{\varepsilon}^e$ and a chemical strain due to local lithium concentration part $\boldsymbol{\varepsilon}^c$ as

$$\boldsymbol{\varepsilon}(\mathbf{u}; \mathbf{x}) = \boldsymbol{\varepsilon}^e(\mathbf{u}, c; \mathbf{x}) + \boldsymbol{\varepsilon}^c(c; \mathbf{x}). \quad (9)$$

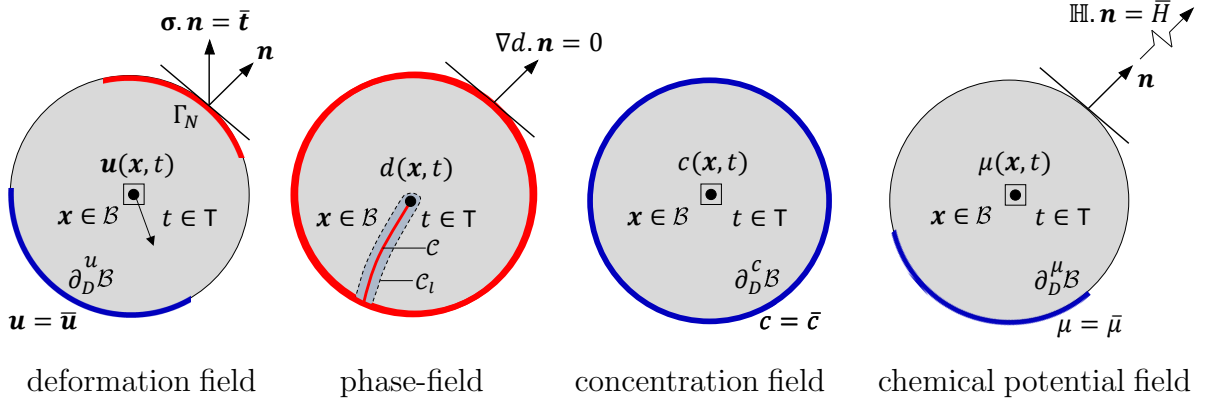


Figure 4: Multi-field problem outline and setup of the notation for chemo-elasticity coupled with phase-field fracture. The deformation field \mathbf{u} , phase-field fracture d , lithium-ion concentration c , and chemical potential field μ are defined on the solid domain \mathcal{B} .

Typically, chemical strain which is considered as a hydrostatic dilatation, is defined:

$$\boldsymbol{\varepsilon}^c(c; \mathbf{x}) := \frac{\Omega_c(c - c_0)}{3} \mathbf{I}. \quad (10)$$

Here, Ω_c refers to the lithium partial molar volume, and the term $c - c_0$ results from the consideration of the substitutional nature of lithium-ion diffusion. Here, c_0 describes the reference lithium concentration in the stress-free state which is set as zero in this study.

The solid \mathcal{B} is loaded by prescribed deformations and external tractions on the boundary, defined by time-dependent Dirichlet conditions and Neumann conditions

$$\mathbf{u} = \bar{\mathbf{u}}(\mathbf{x}, t) \text{ on } \partial_D^u \mathcal{B} \quad \text{and} \quad \boldsymbol{\sigma} \cdot \mathbf{n} = \bar{\tau}(\mathbf{x}, t) \text{ on } \partial_N^u \mathcal{B}, \quad (11)$$

where \mathbf{n} is the outward unit normal vector on the surface $\partial \mathcal{B}$. The stress tensor $\boldsymbol{\sigma}$ is the thermodynamic dual to $\boldsymbol{\varepsilon}$ and $\bar{\tau}$ is the prescribed traction vector.

Prescribed Dirichlet boundary condition and Neumann boundary condition for the lithium chemical potential can be described by:

$$\mu = \bar{\mu}(\mathbf{x}, t) \text{ on } \partial_D^\mu \mathcal{B} \quad \text{and} \quad \mathbb{H} \cdot \mathbf{n} = \bar{H}(\mathbf{x}, t) \text{ on } \partial_N^\mu \mathcal{B}, \quad (12)$$

through the lithium flux vector \mathbb{H} , the imposed lithium chemical potential $\bar{\mu}$ on the boundary surface, lithium transport \bar{H} on the Neumann boundary surface. So, the fracture in electrochemical process is due to the stress concentration of the chemical load through a concentration field of Li^+ or lithium flux.

2.2. Thermomechanical framework: Dissipation inequality and constitutive relations

In line with the theory of generalized standard materials [75], the evolution of the system is characterized by two basic energy quantities: an internal energy density and a dissipation potential. Concerning the former, we let $W := W(\boldsymbol{\varepsilon}, c, d, \nabla d, \vartheta)$ with a global field d denote a Helmholtz-type free energy density, and ϑ denoted as an ambient

temperature. The second law of thermodynamics is taken as a priori restriction, given for isothermal processes by the Clausius-Duhem inequality δ_{loc} as:

$$\delta_{loc} := \boldsymbol{\sigma} : \dot{\boldsymbol{\varepsilon}} - \eta_\vartheta \dot{\vartheta} + \mu \dot{c} - \dot{W}(\boldsymbol{\varepsilon}, c, d, \nabla d, \vartheta) - \mathbb{H} \cdot \nabla \mu - \frac{1}{\vartheta} \mathbb{Q} \cdot \nabla \vartheta \geq 0. \quad (13)$$

Here, (\mathbb{H}, \mathbb{Q}) are flux vectors dual-conjugate to (c, ϑ) . Due to the distinct nature of the dissipative processes, stronger conditions are generally employed to enforce the Clausius-Duhem inequality [76], where the *intrinsic dissipation* δ_{int} and the *chemical diffusion dissipation* δ_{dif} , and a thermal conductive part δ_{con} are enforced to be non-negative separately. In the present case, from inequality (13), one has

$$\begin{aligned} \delta_{int} &= \boldsymbol{\sigma} : \dot{\boldsymbol{\varepsilon}} - \eta_\vartheta \dot{\vartheta} + \mu \dot{c} - \dot{W}(\boldsymbol{\varepsilon}, c, d, \nabla d, \vartheta) \geq 0, \\ \delta_{dif} &= -\mathbb{H} \cdot \nabla \mu \geq 0, \\ \delta_{con} &= -\frac{1}{\vartheta} \mathbb{Q} \cdot \nabla \vartheta \geq 0. \end{aligned} \quad (14)$$

In the following, we ensured that isothermal conditions, such that $\dot{\vartheta} = 0$ and $\nabla \vartheta = 0$. So, $W(\boldsymbol{\varepsilon}, c, d, \nabla d, \vartheta) \approx W(\boldsymbol{\varepsilon}, c, d, \nabla d; \vartheta)$ which is not changed in time with respect to the temperature and from now forward, only for the sake of simplicity, the storage energy will be reduced as $W(\boldsymbol{\varepsilon}, c, d, \nabla d)$. However, we further assumed that lithium chemical storage energy solely depends on ambient temperature which kept constant. From the intrinsic dissipation inequality (14)₁, the Coleman-Noll procedure yields the constitutive relations

$$\boldsymbol{\sigma} = \frac{\partial W}{\partial \boldsymbol{\varepsilon}}(\boldsymbol{\varepsilon}, c, d, \nabla d) \quad \text{and} \quad \mu = \frac{\partial W}{\partial c}(\boldsymbol{\varepsilon}, c, d, \nabla d), \quad (15)$$

for the generalized stress tensor $\boldsymbol{\sigma}$, and lithium chemical potential μ . On the other hand, the generalized fracture driving force β^d conjugate to d read

$$\beta^d = -\delta_d \widehat{W}(\boldsymbol{\varepsilon}, c, d, \nabla d), \quad (16)$$

where, \widehat{W} is introduced to invoke the energetic-dissipative decomposition of the energy, see Section 2.5.2. We note that, this type of decomposition is already introduced in rate-dependent problem, e.g., [77]. Here, $\delta_\diamond := \partial_\diamond - \operatorname{div}[\partial_{\nabla \diamond}]$ denotes the spatial Euler-Lagrange operator. Using equations (15) and (16), the condition $\delta_{int} > 0$ yields

$$\beta^d \cdot \dot{d} \geq 0 \quad \text{in } \Omega \quad \text{and} \quad -(\mathbf{n} \cdot \partial_{\nabla d} W(\boldsymbol{\varepsilon}, c, d, \nabla d)) \cdot \dot{d} \geq 0 \quad \text{on } \Gamma. \quad (17)$$

In fact, (17) is so-called the local dissipation in the reduced form, such that the thermodynamic constraint in the fracture constitutive model is ensured by imposing a positive force $\beta^d \geq 0$ and the assumed growth condition $\dot{d} \geq 0$ of the crack phase field. For rate-independent systems, the dissipation rate δ_{int} is characterized by a thermodynamically admissible dissipation potential ϕ_{int} , a non-negative, convex 1-homogeneous function in $\{\dot{d}, \nabla \dot{d}\}$, non-differentiable and vanishing at null rates. Then, defining for notational simplicity the constitutive state as $\mathbf{c} := \{\boldsymbol{\varepsilon}, c, d, \nabla d\}$, we have

$$\delta_{int} := \phi_{int}(\dot{d}, \nabla \dot{d}; \mathbf{c}, \beta^d) \geq 0. \quad (18)$$

This follows with the definition of the energetic force s^d and the micro force through \mathbb{F} as:

$$s^d = -\frac{\partial W}{\partial d}(\boldsymbol{\varepsilon}, c, d, \nabla d) \quad \text{and} \quad \mathbb{F} = \frac{\partial W}{\partial \nabla d}(\boldsymbol{\varepsilon}, c, d, \nabla d). \quad (19)$$

Here, s^d is the energetic dual variable to the fracture phase-field d , such that $s^d - \operatorname{div}[\mathbb{F}] = \beta^d$. For a detail formulation, see Section 2.5.2.

2.3. Constitutive energy density functions for chemo-elasticity

For the variational formulation setting, it suffices to define the constitutive energy density functions W_{elas} , and W_{Li-ion} to establish the multi-field evolution problem in terms of the primary fields. As we shall recall in the sequel, such a variational structure is not always present in phase-field models for chemo-elastic media fracture, resulting in greater flexibility at the cost of a convenient mathematical structure.

2.3.1. Elastic contribution. The elastic energy density W_{elas} is expressed in terms of the effective strain energy density $\psi_e(\boldsymbol{\varepsilon}^e)$. In our formulation to preclude fracture in compression, a decomposition of the effective strain energy density into *damageable* and *undamageable* parts is employed. As already mentioned in the introduction section, a major contribution to the damage mechanisms of the lithium-ion battery electrode particles is swelling and shrinkage effects [14]. Thus, we perform additive decomposition of the strain tensor into *volume-changing* (volumetric) and *volume-preserving* (deviatoric) counterparts

$$\boldsymbol{\varepsilon}^e(\mathbf{u}, \mathbf{x}) = \boldsymbol{\varepsilon}^{e,vol}(\mathbf{u}, \mathbf{x}) + \boldsymbol{\varepsilon}^{e,dev}(\mathbf{u}, \mathbf{x}),$$

where

$$\begin{aligned} \boldsymbol{\varepsilon}^{e,vol}(\mathbf{u}, \mathbf{x}) &:= \mathbb{P}^{vol} : \boldsymbol{\varepsilon}^e, \quad \text{with} \quad \mathbb{P}_{ijkl}^{vol} := \frac{1}{3} \delta_{ij} \delta_{kl}, \\ \boldsymbol{\varepsilon}^{e,dev}(\mathbf{u}, \mathbf{x}) &:= \mathbb{P}^{dev} : \boldsymbol{\varepsilon}^e, \quad \text{with} \quad \mathbb{P}^{dev} := \mathbb{I} - \frac{1}{3} \mathbf{I} \otimes \mathbf{I} \quad \text{and} \quad \mathbb{I}_{ijkl} := \frac{1}{2} (\delta_{ik} \delta_{jl} + \delta_{il} \delta_{jk}), \end{aligned} \quad (20)$$

along with the first and second invariants of the elastic strain denoted as $I_1(\boldsymbol{\varepsilon}^e) := \text{tr}[\boldsymbol{\varepsilon}^e]$ and $I_2(\boldsymbol{\varepsilon}^e) := \text{tr}[(\boldsymbol{\varepsilon}^e)^2]$. The effective strain energy function $\psi_e(\boldsymbol{\varepsilon}^e)$ is additively decomposed into damageable and undamageable contributions:

$$\psi_e(I_1(\boldsymbol{\varepsilon}^e), I_2(\boldsymbol{\varepsilon}^e)(\mathbf{x})) = \psi_e^+(I_1, I_2) + \psi_e^-(I_1), \quad (21)$$

such that

$$\psi_e^+ = H^+[I_1] \psi_e^{vol}(I_1) + \psi_e^{dev}(I_1, I_2) \quad \text{and} \quad \psi_e^- = (1 - H^+[I_1]) \psi_e^{vol}(I_1). \quad (22)$$

Therein, $H^+[I_1(\boldsymbol{\varepsilon}^e)]$ is a *positive Heaviside function* which returns one and zero for $I_1(\boldsymbol{\varepsilon}^e) > 0$ and $I_1(\boldsymbol{\varepsilon}^e) \leq 0$, respectively. We note that in this paper the volumetric and deviatoric counterparts of the energy take the following forms:

$$\psi_e^{vol}(I_1) = \frac{K}{2} I_1^2 = \frac{K}{2} (\boldsymbol{\varepsilon}^{e,vol} : \mathbf{I})^2 \quad \text{and} \quad \psi_e^{dev}(I_1, I_2) = \mu \left(\frac{I_1^2}{3} - I_2 \right) = \mu \boldsymbol{\varepsilon}^{e,dev} : \boldsymbol{\varepsilon}^{e,dev}. \quad (23)$$

Here, $K = \lambda + \frac{2}{3}\mu > 0$ is the bulk modulus which includes the elastic Lamé's first constant denoted by λ and the shear modulus μ . The total elastic contribution to the pseudo-energy (36) finally reads

$$W_{elas}(\boldsymbol{\varepsilon}, \boldsymbol{\varepsilon}^c, d) := g(d) [\psi_e^+(I_1, I_2)] + \psi_e^-(I_1, I_2), \quad (24)$$

where $g(d)$ is the *elastic degradation function*, which takes in a simple quadratic form as:

$$g(d) = (1 - \kappa_d)(1 - d)^2 + \kappa_d, \quad (25)$$

where κ_d is the so-called ersatz material parameter (set as a very small quantity) which is used to avoid numerical instabilities, and mathematically it is also dependent on the discretization space, see [78]. So, the global mechanical form of the equilibrium equation for the solid body which is represented for the the *first* PDE through for the multi-field system as

$$\text{Div } \boldsymbol{\sigma}(\mathbf{u}, c, d) + \bar{\mathbf{f}} = \mathbf{0}, \quad (26)$$

such that dynamic motion is neglected (i.e., quasi-static response), and we denote $\bar{\mathbf{f}}$ as a prescribed body force.

We note that, the current resulting degraded stress tensor by the bulk energy is rely on the *vol/dev* decomposition. But, it is also possible to enhance (24), for the material which are sensitive to the shear fracture/rotational as it is investigated in rock-like materials, e.g. [79, 80, 81]. So, to explore different characteristic behavior of fracture which is subjected to compression and shear modes for lithium-ion battery electrode particles, we could introduce different crack phase-field driving force. This subject is open for further investigation.

2.3.2. Lithium-ion contribution. To formulate the constitutive equation for the chemo-elastics, the gradient of the chemical potential as the chemical driving force for diffusion response has to be discussed. This follows by the mass conservation for the lithium concentration which includes chemical concentration and a solid matrix within the bulk material. The lithium flux vector given in (12) can be described through the negative direction of the material gradient of the lithium chemical potential $\nabla\mu$ through the diffusivity, based on linear Onsager relationship (similar to the generalize Fick's first law [82] and Fourier's law of heat conduction) [83]:

$$\mathbb{H} := -\mathbf{K}(c, d) \nabla\mu \quad \text{in } \mathcal{B}. \quad (27)$$

Here, \mathbb{H} refers to the the lithium-ion flux vector, which will be elaborated in Section 2.5.1. Therefore, Lithium-ion move from areas of high chemical potential to regions with lower chemical potential. In (27), the concentration diffusivity tensor is given by isotropic tensor \mathbf{K} that is described based on the lithium concentration, c as well as the crack phase-field d , as follows

$$\mathbf{K}(c, d) = g(d) \frac{D}{R\vartheta} c \mathbf{I}. \quad (28)$$

Here, D denotes the lithium diffusion coefficient, R indicates the universal gas constant that is $8.314 \text{ J.K}^{-1}.\text{mol}^{-1}$, and ϑ represents the ambient temperature (see [20, 84]). So, the conservation of the lithium-ion mass which reflects the *second* PDE within chemo-mechanical fracturing media reads

$$\dot{c} = \text{Div}[\mathbb{H}], \quad (29)$$

Following [85], the lithium-Ion density function takes the following form

$$W_{Li-ion}(c; \vartheta) = \mu_0 c + R\vartheta N_L \left(\Theta_L \ln \Theta_L + (1 - \Theta_L) \ln (1 - \Theta_L) \right), \quad (30)$$

here, μ_0 is the the reference chemical potential. For the other two parameters, i.e., N_L , and Θ_L are used in $W_{Li-ion}(c; \vartheta)$, we have:

- **Number of moles of lattice sites of lithium network N_L .** The number of moles of lattice sites in the lithium metal network denoted as N_L where constant interstitial sites concentration is assumed $\nabla N_L = 0$.
- **Occupancy fraction of lithium network Θ_L .** Let low occupancy of interstitial of lithium network, thus we have $\Theta_L = c/N_L$ for $0 < \Theta_L \ll 1$.
- **Isothermal condition ϑ .** Here, we assumed that isothermal conditions for thermal effect, such that $\dot{\vartheta} = 0$ and $\nabla\vartheta = 0$.

We note that this phenomenological approach to the degradation mechanism of lithium-ion battery has some similarity to the diffusion of hydrogen and oxygen in fractured metals, where the solute becomes entrapped ahead of the crack tip [85, 86].

2.3.3. Fracture contribution. The phase-field contribution is expressed in terms of the crack surface energy density γ and the fracture length-scale parameter l_d that governs the regularization. In particular, the sharp-crack surface topology \mathcal{C} is regularized by a functional \mathcal{C}_{l_d} , as outlined in [87] and [39]. This geometrical perspective is in agreement with the framework of [36], which was conceived as a Γ -convergence regularization of the variational approach to Griffith fracture [35]. In the case of isotropic materials, the regularized functional reads

$$\mathcal{C}_{l_d}(d) = \int_{\mathcal{B}} \gamma(d, \nabla d; l_d) dV. \quad (31)$$

In line with standard phase-field models, a general surface density function for the isotropic part γ_l is defined as

$$\gamma(d, \nabla d; l_d) := \frac{1}{c_d} \left(\frac{\omega(d)}{l_d} + l_d \nabla d \cdot \nabla d \right) \quad \text{with} \quad c_d := 4 \int_0^1 \sqrt{\omega(b)} db, \quad (32)$$

where $\omega(d)$ is a monotonic and continuous *local fracture energy function* such that $\omega(0) = 0$ and $\omega(1) = 1$. A variety of suitable choices for $\omega(d)$ are available in the literature [88, 89, 90]. Here, the widely adopted linear and quadratic formulations are considered, which yield, respectively, models with and without an elastic stage. Specifically, we define

$$\omega(d) := \begin{cases} d & \Rightarrow c_d = 8/3 \\ d^2 & \Rightarrow c_d = 2 \end{cases} \quad \begin{array}{ll} \text{model with an elastic stage,} \\ \text{model without an elastic stage.} \end{array} \quad (33)$$

We note that the *active zone* within lithium-ion battery electrode particles refers to the components within the electrodes that actively participate in the electrochemical reactions during the battery's operation. These area undergo reversible changes in their composition as lithium-ions move in and out during charging and discharging cycles. On the other hand, the *deactive zone* (or dead area) within lithium-ion battery, indicates those portions of the electrodes that do not actively contribute to the electrochemical processes. Accordingly, within the active materials both the cathode and anode undergo stress during charge and discharge cycles. This stress, is often associated with volume changes (expansion and contraction), which results in mechanical degradation (so $d \rightarrow 0$). It is remarkable that inactive zones could contribute to the initiation of unwanted side reactions, and so crack nucleation could be happened.

2.3.4. Energy quantities. The coupled BVP is formulated through three specific fields (i.e., unknown solution fields) to illustrate the chemo-elasticity of lithium-ion battery electrode particles in the fracturing material by

$$\text{Global Primary Fields : } \mathfrak{U} := \{\mathbf{u}, d, c\}. \quad (34)$$

Here, \mathbf{u} is the displacement (mechanical deformation), c denotes the lithium concentration, and d is the crack phase-field ($0 \leq d \leq 1$). From the numerical implementation standpoint, to guarantee $0 \leq d \leq 1$ holds, we project $d > 1$ to 1 and $d < 0$ to 0 to avoid unphysical crack phase-field solution [91]. The constitutive formulations for the chemo-mechanical phase-field fracture model are written in terms of the following set

$$\text{Constitutive State Variables : } \mathfrak{C} := \{\boldsymbol{\varepsilon}, \boldsymbol{\varepsilon}^c, d, \nabla d, \mu, \mathbb{B}\}, \quad (35)$$

representing a combination of a first-order gradient elasticity model and a first-order gradient damage model. A pseudo-energy density per unit volume is then defined as $W := W(\mathfrak{C})$, which is additively decomposed into an elastic contribution W_{elas} , and a Lithium-ion contribution W_{Li-ion} :

$$W(\mathfrak{C}) := W_{elas}(\boldsymbol{\varepsilon}, \boldsymbol{\varepsilon}^c, d) + W_{Li-ion}(c; \vartheta). \quad (36)$$

We note that W is a state function that contains only energetic contributions. With this function at hand, a pseudo potential energy functional can be written as

$$\mathcal{E}(\mathbf{u}, d, c) := \int_{\mathcal{B}} W(\mathfrak{C}) \, dV. \quad (37)$$

2.4. Potential energy of the external loading

The macroscopic continuum domain is assumed to be loaded by macroscopic external field actions. As indicated in Figure 4, we assumed the macroscopic body force denoted by $\bar{\mathbf{f}}$ per unit volume of the domain \mathcal{B} , and traction field $\bar{\boldsymbol{\tau}}$ on the surfaces $\partial_N^u \mathcal{B}$ for the mechanical contribution. Accordingly, for the lithium-ion contribution, we consider the specific macroscopic chemical source per unit mass \bar{r} of the domain \mathcal{B} is neglected, while external chemical out-flux \bar{H} on the surfaces $\partial_N^\mu \mathcal{B}$ is applied. So, the work of external loads of the mechanical contribution reads:

$$\mathcal{E}_{ext}^u(\dot{\mathbf{u}}) := \int_{\mathcal{B}} \bar{\mathbf{f}} \cdot \dot{\mathbf{u}} \, dV + \int_{\partial_N^u \mathcal{B}} \bar{\boldsymbol{\tau}} \cdot \dot{\mathbf{u}} \, dA, \quad (38)$$

and for lithium-ion concentration contribution, we have:

$$\mathcal{E}_{ext}^\mu(\dot{H}) = - \int_{\partial_N^\mu \mathcal{B}} \bar{\mu} H \, dA. \quad (39)$$

2.5. Dissipation for the rate of minimization principle

The gradient theories of standard dissipative solids in chemo-elasticity media are governed by two scalar constitutive functions consisting of the energy storage and the dissipation functions. In the previous section, we described the internal energy storage. Thus, in

in this section the dissipative response of the material is further elaborated. The field equations of dissipative solids are related to rate-type incremental variational formulations. To do so, the first-order spatial gradient of the primary fields in which that describe the evolving dissipative mechanism are further considered. These constitutive functions results in a compact variational formulation, thus yielding in a theoretical development of incremental minimization and saddle point principles for a class of gradient-type dissipative materials that incorporate multi-field boundary value problems.

In fact, the dissipative response of the material same as the energy density functional, is additively decomposed into lithium-ion concentration flow, fracture evolution through:

$$\mathcal{D}(\mathbb{B}, \mathbb{H}, \dot{d}; d, \nabla d, \alpha) = \mathcal{D}_{Li-ion}(\mathbb{B}, \mathbb{H}; d) + \mathcal{D}_{frac}(\dot{d}; d, \nabla d, \alpha). \quad (40)$$

Here, two dual conjugated vector fields (\mathbb{B}, \mathbb{H}) , will be elaborated in the next section. Accordingly, we explain individual contributions of the dissipation potential and their ingredients.

2.5.1. Lithium-ion concentration dissipation. The canonical convective dissipation potential for lithium-ion concentration flow is assumed to be of quadratic form in terms of the gradient of lithium chemical potential field $\mu(\mathbf{x}, t)$, by

$$\widehat{\Phi}_{Li-ion}(\mathbb{B}, d) = \frac{1}{2} \mathbf{K} : (\mathbb{B} \otimes \mathbb{B}) \quad \text{with} \quad \mathbb{B} = -\nabla \mu, \quad (41)$$

here, \mathbb{B} is a lithiation driving force together with the definition of the lithium-ion flux vector \mathbb{H} as

$$\mathbb{H} = \frac{\partial \widehat{\Phi}_{Li-ion}(\mathbb{B}, d)}{\partial \mathbb{B}} = \mathbf{K} \mathbb{B} \quad \text{with} \quad \mathbb{H} \cdot \mathbb{B} \geq 0, \quad (42)$$

see dissipation inequality (14)₂. Here, the force \mathbb{B} is dual to flux \mathbb{H} . We note that the dual convective dissipation potential $\widehat{\Phi}_{Li-ion}^*$ based on the lithium flux vector can be further evaluated as:

$$\widehat{\Phi}_{Li-ion}^*(\mathbb{B}, d) = \frac{1}{2} \mathbf{K}^{-1} : (\mathbb{H} \otimes \mathbb{H}), \quad (43)$$

So, the *mixed dissipation potential functional* for lithium-ion concentration flow reads

$$\mathcal{D}_{Li-ion}(\mathbb{B}, \mathbb{H}, d) = \int_{\mathcal{B}} \left(\mathbb{B} \cdot \mathbb{H} - \widehat{\Phi}_{Li-ion}(\mathbb{B}, d) \right) dV, \quad (44)$$

which is also called an *extended dissipation potential functional*. For further theoretical details on these types of extended dissipation functional as a function of an extended set of variables, we refer interested readers to [92, 93].

This is also connected to its dual dissipation through:

$$\mathcal{D}_{Li-ion}^*(\mathbb{H}, d) = \sup_{\mathbb{B}} [\mathcal{D}_{Li-ion}(\mathbb{B}, \mathbb{H}, d)], \quad (45)$$

that is reduced to:

$$\mathcal{D}_{Li-ion}^*(\mathbb{B}, \mathbb{H}, d) = \int_{\mathcal{B}} \widehat{\Phi}_{Li-ion}^*(\mathbb{B}, d) dV. \quad (46)$$

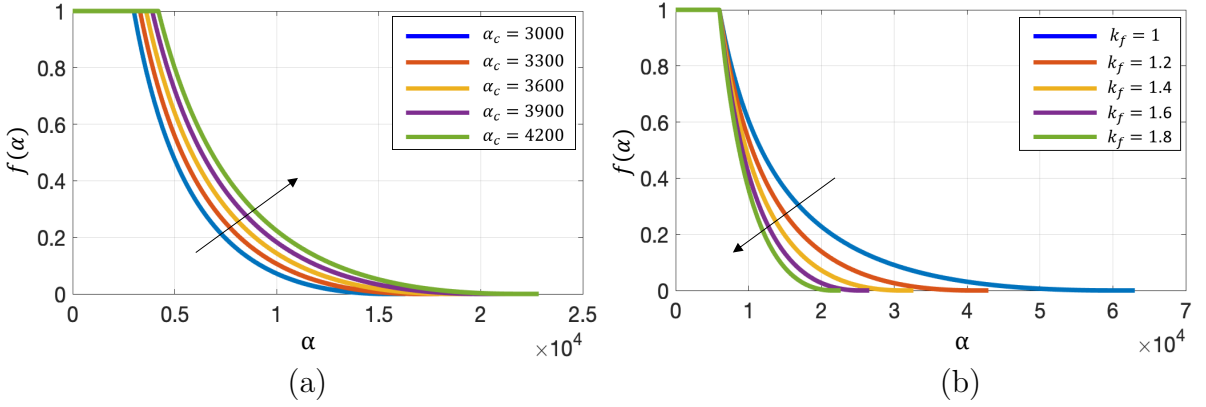


Figure 5: Fatigue degradation function (a) for different values of fatigue threshold parameter α_c at fixed $k_f = 1.4$ and (b) different values for fatigue model parameter k_f at fixed $\alpha_c = 3000$.

2.5.2. Damage dissipation. In the failure mechanism, the dissipation-potential density $\widehat{\Phi}_{frac}$ associated accounts for the evolving crack topology has to be elaborated. The formulation response has to preserve thermodynamical consistency by ensuring an irreversibility condition, i.e., $\dot{d} \geq 0$. To do so, dissipation-potential density for fracture evolution reads:

$$\widehat{\Phi}_{frac}(\dot{d}, \nabla \dot{d}; \alpha) := g_c f(\alpha) \frac{d}{dt} \gamma(d, \nabla d) \quad \text{and} \quad \widehat{\Phi}_{vis}(\dot{d}) := \frac{\eta_d}{2} \dot{d}^2. \quad (47)$$

Here, $\widehat{\Phi}_{vis}$ denotes the dissipative power density due to viscous resistance forces. Here, η_d is the material parameter that characterize the viscous response of the fracture evolution. Here, g_c is Griffith's critical elastic energy release rate. This parameter is scaled by a non-negative fatigue degradation function $f(\alpha)$. In fact, $f(\alpha)$ helps to account additional stress concentration due lithiation/delithiation (load/unloading) process during the charge/discharge process. The second axiom of thermodynamics for the fatigue response is satisfied by the non-negativity of the dissipation rate, i.e.,

$$\widehat{\Phi}_{frac}(\dot{d}, \nabla \dot{d}; \alpha) \geq 0. \quad (48)$$

Following [94], the following possible form, where k is a constant to adapt the rate of decay of the fatigue degradation function.

$$f(\alpha) = \begin{cases} 1 & \alpha(\mathbf{x}, t) \leq \alpha_c, \\ [1 - k_f \log \frac{\alpha(\mathbf{x}, t)}{\alpha_c}]^2 & \alpha(\mathbf{x}, t) \leq \alpha_c 10^{1/k_f}, \\ 0 & \text{otherwise.} \end{cases} \quad (49)$$

Here, $\alpha_c \geq 0$ is a material threshold parameter, which below that no fatigue effects are triggered. Also, k_f is the fatigue model parameter. Figure (5) delivers fatigue degradation function $f(\alpha)$ given in (49). It is trivial by varying the fatigue model parameter k_f the slop of the $f(\alpha)$ could be turned, so helping to have more calibration when simulating material modeling. The fatigue variable α is defined as an accumulation of strain energy density W_{elas} during loading stages, thus:

$$\alpha(\mathbf{x}, t) := \int_0^t \dot{\Lambda}(\mathbf{x}, s) \bar{H}(\dot{\Lambda}(\mathbf{x}, s)) dA \quad \text{with} \quad \Lambda(\boldsymbol{\varepsilon}^e, \mu, d) := W_{elas}(\boldsymbol{\varepsilon}, \boldsymbol{\varepsilon}^c, d), \quad (50)$$

that is

$$\alpha(\mathbf{x}, t) = \alpha_n(\mathbf{x}, t) + (\Lambda - \Lambda_n)\bar{H}(\Lambda - \Lambda_n). \quad (51)$$

Here, \bar{H} refers to standard Heaviside function. So, $\alpha(\mathbf{x}, t)$ depends on both mechanical deformation and chemical lithium concentration.

Accordingly, the local evolution of the crack phase-field equation represented for the *third* PDE in the given domain \mathcal{B} with its homogeneous NBC, i.e. $f(\alpha)\nabla d \cdot \mathbf{n} = 0$ on $\partial\mathcal{B}$ yields

$$\eta_d \dot{d} = (1 - d)f(\alpha)\mathcal{H} - \left[f(\alpha)\omega'(d) - 2l_d^2 \operatorname{div}[f(\alpha).\nabla d] \right], \quad (52)$$

Here, the maximum positive crack driving force \mathcal{H} in $t \in [0, t_n]$ as a source of the fatigue fracture has been used, see Section 2.7.3. Finally, the dissipation potential for fatigue evolution reads

$$\mathcal{D}_{frac}(\dot{d}; \alpha) = \int_{\mathcal{B}} \left(\widehat{\Phi}_{frac} + \widehat{\Phi}_{vis}(\dot{d}) + I_+(\dot{d}) \right) dV. \quad (53)$$

To complete our derivation, let us now define the fracture yield function by

$$\beta^d(s^d, h^d; d) := -\delta_d \widehat{W} = s^d - g_c h^d. \quad (54)$$

Where, \widehat{W} is energetic-dissipative decomposition of the energy defined as $\widehat{W} := W_{elas} + \gamma(d, \nabla d)$. Thus, a driving force reads:

$$s^d = -\frac{\partial W}{\partial d} = -\left[\frac{\partial g(d)}{\partial d} \psi_e^+ \right], \quad \text{and} \quad h^d = \delta_d \gamma_{l_d} \geq 0. \quad (55)$$

The Euler equations of the maximization principle follow the fracture evolution rule through

$$\dot{d} = \lambda^d \frac{\partial \beta^d}{\partial s^d}, \quad (56)$$

which yields the KKT conditions for fracture:

$$\beta^d \leq 0, \quad \lambda^d \geq 0, \quad \text{and} \quad \beta^d \lambda^d = 0. \quad (57)$$

Formulation 2.1 (Energy functional for the fracturing chemo-elasticity media). Consider an open bounded domain \mathcal{B} with boundary $\partial\mathcal{B} = \partial^u\mathcal{B} \cup \partial^\mu\mathcal{B}$. Let constants $(K, \mu, g_c, l_d, \eta_d, D, R, \Omega_c, N_L) \geq 0$ at the constant ambient temperature ϑ be given with the initial conditions $\dot{\mathbf{u}}_0 = \dot{\mathbf{u}}(\mathbf{x}, 0)$, $\dot{d}_0 = d(\mathbf{x}, 0)$, $\dot{c}_0 = \dot{p}(\mathbf{x}, 0)$, and $\dot{c}_0 = \dot{c}(\mathbf{x}, 0)$. For the loading increments $n = 1, 2, \dots, N$, find $\dot{\mathbf{u}} \in \mathcal{W}_{\dot{\mathbf{u}}}^{\dot{\mathbf{u}}}$, $d \in \mathcal{W}_d^d$, $\mathbb{H} \in \mathcal{W}_{\mathbb{H}}^{\mathbb{H}}$, and $\mathbb{B} \in \mathcal{W}^{\mathbb{B}}$ such that the following potential:

$$\underbrace{\Pi(\dot{\boldsymbol{\varepsilon}}^e, \dot{d}, \mathbb{B}, \mathbb{H})}_{\text{rate of potential}} := \underbrace{\frac{d}{dt} \widehat{\mathcal{E}}(\boldsymbol{\varepsilon}^e, d, c)}_{\text{rate of energy}} + \underbrace{\mathcal{D}(\mathbb{B}, \mathbb{H}, \dot{d}; d, \alpha)}_{\text{dissipation}} - \underbrace{\mathcal{E}_{ext}(\dot{\mathbf{u}}, c)}_{\text{external power}}, \quad (58)$$

at the given state is minimized. Herein, the rate of the energy potential reads:

$$\frac{d}{dt} \widehat{\mathcal{E}}(\boldsymbol{\varepsilon}^e, d, c) = \int_{\mathcal{B}} \left(\frac{\partial W}{\partial \boldsymbol{\varepsilon}^e} : \dot{\boldsymbol{\varepsilon}} - \frac{\partial W}{\partial c} \operatorname{Div}[\mathbb{H}] + \frac{\partial W}{\partial d} \dot{d} + \frac{\partial W}{\partial \nabla d} \cdot \nabla \dot{d} \right) dV,$$

and total dissipation potential is:

$$\mathcal{D}(\mathbb{B}, \mathbb{H}, \dot{d}; d, \alpha) = \mathcal{D}_{Li-ion}(\mathbb{B}, \mathbb{H}; d) + \mathcal{D}_{frac}(\dot{d}; \alpha),$$

with external loading potential is:

$$\mathcal{E}_{ext}(\dot{\mathbf{u}}, \mathbb{H}) = \mathcal{E}_{ext}^u(\dot{\mathbf{u}}) + \mathcal{E}_{ext}^\mu(\mathbb{H}).$$

The minimization problem for the energy functional of the crack phase-field chemo-elastic media is given in Formulation 2.2 takes the following compact form:

$$(\dot{\boldsymbol{\varepsilon}}^e, \dot{d}, \mathbb{B}, \mathbb{H}) = \arg \left\{ \inf_{\mathbf{u} \in \mathcal{W}_u^u} \inf_{\mathbb{B} \in \mathcal{W}^B} \sup_{\mathbb{H} \in \mathcal{W}_{\mathbb{H}}^H} \inf_{d \in \mathcal{W}_{dn}^d} \Pi(\dot{\boldsymbol{\varepsilon}}^e, \dot{d}, \mathbb{B}, \mathbb{H}) \right\}, \quad (59)$$

that is the rate-type mixed variational saddle-point principle for four fields problems $(\dot{\boldsymbol{\varepsilon}}^e, \dot{d}, \mathbb{B}, \mathbb{H})$, with *mixed four-field total potential functional* for dual conjugated vector fields (\mathbb{B}, \mathbb{H}) which reads:

$$\begin{aligned} \Pi(\dot{\boldsymbol{\varepsilon}}^e, \dot{d}, \mathbb{B}, \mathbb{H}) &= \int_{\mathcal{B}} \left(\frac{\partial W}{\partial \boldsymbol{\varepsilon}^e} : \dot{\boldsymbol{\varepsilon}} - \frac{\partial W}{\partial c} \text{Div}[\mathbb{H}] + \frac{\partial W}{\partial d} \dot{d} + \frac{\partial W}{\partial \nabla d} \cdot \nabla \dot{d} \right) \, dV \\ &\quad + \int_{\mathcal{B}} \left(\mathbb{B} \cdot \mathbb{H} - \widehat{\Phi}_{Li-ion}(\mathbb{B}, d) + \widehat{\Phi}_{frac} + \widehat{\Phi}_{vis}(\dot{d}) + I_+(\dot{d}) \right) \, dV \quad (60) \\ &\quad - \int_{\mathcal{B}} \bar{\mathbf{f}} \cdot \dot{\mathbf{u}} \, dV - \int_{\partial_N^u \mathcal{B}} \bar{\boldsymbol{\tau}} \cdot \dot{\mathbf{u}} \, dA + \int_{\partial_N^\mu \mathcal{B}} \bar{\mu} H \, dA. \end{aligned}$$

A rate-type mixed variational principle is obtained by exchanging the dissipation potential functional $\mathcal{D}^*_{Li-ion}(\mathbb{H}, d)$ in (45) by the extended dissipation potential function $\mathcal{D}_{Li-ion}(\mathbb{B}, \mathbb{H}, d)$ introduced in (44). We note that for the second term in the $\Pi(\dot{\boldsymbol{\varepsilon}}^e, \dot{d}, \mathbb{B}, \mathbb{H})$, the balance of chemical mass (29) has been used in order to express the rate of relative lithium concentration field c by the chemical flux vector \mathbb{H} . The potential $\Pi(\dot{\boldsymbol{\varepsilon}}^e, \dot{d}, \mathbb{B}, \mathbb{H})$ is linear with respect to the rate of deformation gradient $\dot{\boldsymbol{\varepsilon}}^e$ and the chemical mass flow vector \mathbb{H} and concave with respect to the chemical potential vector field \mathbb{B} .

The necessary condition of the variational principle (58) is that its variation vanishes, i.e., $\delta \Pi_\bullet = 0$ for all $\bullet \in \{\dot{\boldsymbol{\varepsilon}}^e, \dot{d}, \mathbb{B}, \mathbb{H}\}$. So, we define the additional spaces for the set of (\mathbb{B}, \mathbb{H}) by:

$$\mathcal{W}_{\mathbb{H}}^H := \{H^1(\text{Div}, \mathcal{B}) : \mathbb{H} \cdot \mathbf{n} = \bar{H} \text{ on } \partial_N^H \mathcal{B}\}, \quad \text{and} \quad \mathcal{W}^B := \{\mathbb{B} \in L^2(\mathcal{B})\}. \quad (61)$$

Taking the variation of the potential (58) in Formulation (2.1) yields the following Euler equations of the variational principle by:

Balance of linear momentum : $\delta\Pi_{\dot{\varepsilon}^e} \equiv -\operatorname{div}\left[\frac{\partial W}{\partial \dot{\varepsilon}^e}\right] = \bar{\mathbf{f}}$ in \mathcal{B} ,

Constitutive driving force: $\delta\Pi_{\mathbb{H}} \equiv \nabla \frac{\partial W}{\partial c} + \mathbb{B} = 0$ in \mathcal{B} ,

Chemical flow equation: $\delta\Pi_{\mathbb{B}} \equiv \mathbb{H} - \frac{\partial \hat{\Phi}_{Li-ion}(\mathbb{B}, d)}{\partial \mathbb{B}} = 0$ in \mathcal{B} ,

Fracture evolution: $\delta\Pi_d \equiv \frac{\partial W}{\partial d} - \operatorname{div}\left[\frac{\partial \hat{\Phi}_{frac}}{\partial \nabla d}\right] + \frac{\partial \hat{\Phi}_{frac}}{\partial \dot{d}} + \frac{\partial \hat{\Phi}_{vis}}{\partial \ddot{d}} \ni 0$ in \mathcal{B} ,

Traction boundary condition: $\delta\Pi_{\dot{\varepsilon}^e} \equiv \frac{\partial W}{\partial \dot{\varepsilon}^e} \cdot \mathbf{n} = \bar{\tau}$ on $\partial_N^u \mathcal{B}$,

Flux boundary condition: $\delta\Pi_{\mathbb{H}} \equiv \frac{\partial W_{Li-ion}}{\partial c} = \bar{\mu}$ on $\partial_D^\mu \mathcal{B}$,

Phase-field boundary conditions: $\delta\Pi_d \equiv \frac{\partial \hat{\Phi}_{frac}}{\partial \nabla d} \cdot \mathbf{n} = 0$ on $\partial \mathcal{B}$,

which manifest as the governing equations (26), (41)₂, the chemical flow equation (42), and the phase-field evolution equation (52), along with the Neumann boundary conditions for fracture phase-field.

We now aim to derive a reduced form of the (44) which will simplify the minimization problem given in Formulation 2.1. So, by using the identity $\dot{c} + \operatorname{Div}[\mathbb{H}] = 0$ from the (29) and in the absence of the imposed chemical source, we have:

$$\mu\dot{c} + \mu\operatorname{Div}[\mathbb{H}] = \rightarrow \int_{\mathcal{B}} \mu\operatorname{Div}[\mathbb{H}] = \int_{\partial_N^u \mathcal{B}} \mu\mathbb{H} \cdot \mathbf{n} \, dA + \int_{\mathcal{B}} \mathbb{B} \cdot \mathbb{H} \, dV, \quad (62)$$

which results in

$$\int_{\mathcal{B}} (-\mu\dot{c}) \, dV = \int_{\partial_N^u \mathcal{B}} \mu\mathbb{H} \cdot \mathbf{n} \, dA + \int_{\mathcal{B}} \mathbb{B} \cdot \mathbb{H} \, dV, \quad (63)$$

therefore dissipation potential functional for lithium-ion concentration flow reads

$$\hat{\mathcal{D}}_{Li-ion}(\dot{c}, \mu, d) = \int_{\mathcal{B}} \left(-\mu\dot{c} - \hat{\Phi}_{Li-ion}(\mathbb{B}, d) \right) \, dV - \int_{\partial_N^u \mathcal{B}} \mu\mathbb{H} \cdot \mathbf{n} \, dA, \quad (64)$$

then, by imposing $\mu = \bar{\mu}$ on $\partial_D^\mu \mathcal{B}$ as flux boundary condition which is derived earlier for the necessary condition of the variational principle (60), we end up with:

$$\hat{\mathcal{D}}_{Li-ion}(\dot{c}, \mu, d) = \int_{\mathcal{B}} \left(-\mu\dot{c} - \hat{\Phi}_{Li-ion}(\mathbb{B}, d) \right) \, dV, \quad (65)$$

which is also called as an *extended dissipation potential functional*. We note that the chemical flux vector by means of (BC.F), finally results in $\int_{\partial_N^u \mathcal{B}} \mu\mathbb{H} \cdot \mathbf{n} = \int_{\partial_N^u \mathcal{B}} H\bar{\mu}(\mathbf{x}, t)$, see (39). So, we have:

$$\mathcal{D}_{Li-ion}(\mathbb{B}, \mathbb{H}, d) \equiv \hat{\mathcal{D}}_{Li-ion}(\dot{c}, \mu, d). \quad (66)$$

Thus, we are able now to change the minimization set-up for the multi-field potential functional from $\Pi(\dot{\varepsilon}^e, \dot{d}, \mathbb{B}, \mathbb{H})$ toward $\Pi(\dot{\varepsilon}^e, \dot{d}, \dot{c}, \mu)$. This results in the following formulation for the minimization of the reduced energy functional.

Formulation 2.2 (Reduced energy functional for the fracturing chemo-elasticity media). Consider an open bounded domain \mathcal{B} with boundary $\partial\mathcal{B} = \partial^u\mathcal{B} \cup \partial^\mu\mathcal{B}$. Let constants $(K, \mu, g_c, l_d, \eta_d, D, R, \Omega_c, N_L) \geq 0$ at the constant ambient temperature ϑ be given with the initial conditions $\dot{\mathbf{u}}_0 = \dot{\mathbf{u}}(\mathbf{x}, 0)$, $\dot{d}_0 = \dot{d}(\mathbf{x}, 0)$, $\dot{c}_0 = \dot{c}(\mathbf{x}, 0)$, and $\dot{\dot{c}}_0 = \dot{c}(\mathbf{x}, 0)$. For the loading increments $n = 1, 2, \dots, N$, find $\dot{\mathbf{u}} \in \mathcal{W}_{\dot{\mathbf{u}}}^n$, $d \in \mathcal{W}_d^n$, $\mu \in \mathcal{W}_\mu^n$, and $\dot{c} \in \mathcal{W}^c$ such that the following potential:

$$\underbrace{\Pi(\dot{\boldsymbol{\varepsilon}}^e, \dot{d}, \dot{c}, \mu)}_{\text{rate of potential}} := \underbrace{\frac{d}{dt} \widehat{\mathcal{E}}(\boldsymbol{\varepsilon}^e, d, c)}_{\text{rate of energy}} + \underbrace{\mathcal{D}(\dot{c}, \mu, \dot{d}; d, \alpha)}_{\text{dissipation}} - \underbrace{\mathcal{E}_{ext}(\dot{\mathbf{u}}, c)}_{\text{external power}}, \quad (67)$$

at the given state is minimized. Herein, the rate of the energy potential reads:

$$\frac{d}{dt} \widehat{\mathcal{E}}(\boldsymbol{\varepsilon}^e, d, c) = \int_{\mathcal{B}} \left(\frac{\partial W}{\partial \boldsymbol{\varepsilon}^e} : \dot{\boldsymbol{\varepsilon}} + \frac{\partial W}{\partial c} \dot{c} + \frac{\partial W}{\partial d} \dot{d} + \frac{\partial W}{\partial \nabla d} \cdot \nabla \dot{d} \right) dV,$$

and total dissipation potential is:

$$\mathcal{D}(\dot{c}, \mu, \dot{d}; d, \alpha) = \widehat{\mathcal{D}}_{Li-ion}(\dot{c}, \mu; d) + \mathcal{D}_{frac}(\dot{d}; \alpha),$$

with external loading potential is:

$$\mathcal{E}_{ext}(\dot{\mathbf{u}}, \mu) = \mathcal{E}_{ext}^u(\dot{\mathbf{u}}) + \mathcal{E}_{ext}^\mu(\mu).$$

The minimization problem for the energy functional of the crack phase-field chemo-elastic media given in Formulation 2.2 takes the following compact form:

$$(\dot{\boldsymbol{\varepsilon}}^e, \dot{d}, \dot{c}, \mu) = \arg \left\{ \inf_{\mathbf{u} \in \mathcal{W}_{\dot{\mathbf{u}}}^n} \inf_{\dot{c} \in \mathcal{W}^c} \sup_{\mu \in \mathcal{W}_\mu^n} \inf_{d \in \mathcal{W}_d^n} \Pi(\dot{\boldsymbol{\varepsilon}}^e, \dot{d}, \dot{c}, \mu) \right\}, \quad (68)$$

that is the reduced rate-type variational saddle-point principle for four fields problems $(\dot{\boldsymbol{\varepsilon}}^e, \dot{d}, \dot{c}, \mu)$, with reduced mixed four-field total potential functional which is:

$$\begin{aligned} \Pi(\dot{\boldsymbol{\varepsilon}}^e, \dot{d}, \dot{c}, \mu) &= \int_{\mathcal{B}} \left(\frac{\partial W}{\partial \boldsymbol{\varepsilon}^e} : \dot{\boldsymbol{\varepsilon}} + \frac{\partial W}{\partial c} \dot{c} + \frac{\partial W}{\partial d} \dot{d} + \frac{\partial W}{\partial \nabla d} \cdot \nabla \dot{d} \right) dV \\ &\quad + \int_{\mathcal{B}} \left(-\mu \dot{c} - \widehat{\Phi}_{Li-ion}(\mathbb{B}, d) + \widehat{\Phi}_{frac} + \widehat{\Phi}_{vis}(\dot{d}) + I_+(\dot{d}) \right) dV \\ &\quad - \int_{\mathcal{B}} \bar{\mathbf{f}} \cdot \dot{\mathbf{u}} dV - \int_{\partial_N^u \mathcal{B}} \bar{\boldsymbol{\tau}} \cdot \dot{\mathbf{u}} dA - \int_{\partial_N^H \mathcal{B}} \bar{H} \mu dA. \end{aligned} \quad (69)$$

We note that following [95], the external potential for the reduced energy functional for the fracturing chemo-elasticity media, takes the following form:

$$\mathcal{E}_{ext}^\mu(\mathbb{H}) = \int_{\partial_N^H \mathcal{B}} \bar{H} \mu dA. \quad (70)$$

The solution of this stationary principle of (68) is obtained through the Gâteaux derivative of functional (67) with respect to $\dot{\mathbf{u}}$, the lithium chemical potential μ , the relative lithium concentration mass content \dot{c} , and the crack phase-field \dot{d} subject to the irreversibility condition $\dot{d} \geq 0$ provide the governing equations for the elasticity problem,

and the fracture problem, respectively. Such a variational structure results in a convenient numerical implementation based on incremental energy minimization, for which an algorithmic representation of the energy functional is required. This will be discussed in detail in next section.

The necessary condition of the variational principle (58) is that its variation vanishes, i.e., $\delta\Pi_{\bullet} = 0$ for all $\bullet \in \{\dot{\boldsymbol{\varepsilon}}^e, \dot{d}, \dot{c}, \mu\}$. Taking the variation of the potential (67) in Formulation (2.2) yields the following Euler equations of the variational principle by:

$$\begin{aligned}
\text{Balance of linear momentum : } \quad \delta\Pi_{\dot{\boldsymbol{\varepsilon}}^e} &\equiv -\operatorname{div}\left[\frac{\partial W}{\partial \dot{\boldsymbol{\varepsilon}}^e}\right] = \bar{\mathbf{f}} & \text{in } \mathcal{B}, \\
\text{Constitutive of lithium chemical: } \quad \delta\Pi_{\dot{c}} &\equiv \frac{\partial W}{\partial c} - \mu = 0 & \text{in } \mathcal{B}, \\
\text{Balance of lithium-ion diffusion: } \quad \delta\Pi_{\mu} &\equiv -\operatorname{div}\left[\frac{\partial \hat{\Phi}_{Li-ion}}{\partial \mathbb{B}}\right] - \dot{c} = 0 & \text{in } \mathcal{B}, \\
\text{Fracture evolution: } \quad \delta\Pi_d &\equiv \frac{\partial W}{\partial d} - \operatorname{div}\left[\frac{\partial \hat{\Phi}_{frac}}{\partial \nabla d}\right] + \frac{\partial \hat{\Phi}_{frac}}{\partial \dot{d}} + \frac{\partial \hat{\Phi}_{vis}}{\partial \dot{d}} \ni 0 & \text{in } \mathcal{B}, \\
\text{Traction boundary condition: } \quad \delta\Pi_{\dot{\boldsymbol{\varepsilon}}^e} &\equiv \frac{\partial W}{\partial \dot{\boldsymbol{\varepsilon}}^e} \cdot \mathbf{n} = \bar{\boldsymbol{\tau}} & \text{on } \partial_N^u \mathcal{B}, \\
\text{Flux boundary condition: } \quad \delta\Pi_{\mu} &\equiv \frac{\partial \hat{\Phi}_{Li-ion}}{\partial \mathbb{B}} \cdot \mathbf{n} = \mathbb{H} \cdot \mathbf{n} = \bar{H} & \text{on } \partial_N^H \mathcal{B}, \\
\text{Phase-field boundary conditions: } \quad \delta\Pi_d &\equiv \frac{\partial \hat{\Phi}_{frac}}{\partial \nabla d} \cdot \mathbf{n} = 0 & \text{on } \partial \mathcal{B}.
\end{aligned}$$

We note that to derive balance of lithium-ion diffusion as well as flux boundary condition, following identity has been used:

$$\begin{aligned}
\int_{\mathcal{B}} \delta_{\mu} \hat{\Phi}_{Li-ion}(\mathbb{B}, d) \, dV &= \int_{\mathcal{B}} \frac{\partial \hat{\Phi}_{Li-ion}(\mathbb{B}, d)}{\partial \mathbb{B}} \delta_{\mu} \mathbb{B} \, dV = - \int_{\mathcal{B}} \frac{\partial \hat{\Phi}_{Li-ion}(\mathbb{B}, d)}{\partial \mathbb{B}} \delta \nabla \mu \, dV \\
&= \int_{\mathcal{B}} \nabla \frac{\partial \hat{\Phi}_{Li-ion}(\mathbb{B}, d)}{\partial \mathbb{B}} \delta \mu \, dV - \int_{\partial_N^H \mathcal{B}} \frac{\partial \hat{\Phi}_{Li-ion}(\mathbb{B}, d)}{\partial \mathbb{B}} \cdot \mathbf{n} \delta \mu \, dA
\end{aligned} \tag{71}$$

2.6. Incremental energy, dissipation and load functionals for the reduced incremental minimization principle

In this Section, an incremental minimization principles for a class of gradient-type dissipative materials are used to derive the governing equations. Let, the loading interval $\mathcal{T} := (t_0, T)$ is discretized using the discrete time (loading) points

$$0 = t_0 < t_1 < \dots < t_n < t_{n+1} < \dots < t_N = T, \tag{72}$$

with the end time value $T > 0$. The parameter $t \in \mathcal{T}$ denotes for rate-dependent problems due the time, for rate-independent problems an incremental loading parameter. In order to advance the solution within a specific time step, we focus on the finite time increment $[t_n, t_{n+1}]$, with

$$\tau = t_{n+1} - t_n > 0, \tag{73}$$

denotes the time step length. To formulate the incremental variational principles at the current time t_{n+1} associated with known fields at t_n , we need to elaborate the incremental energy storage, dissipation potential and external work done at a finite time step $[t_n, t_{n+1}]$ within chemo-elastic media. This is the main discussion in the next Sections.

2.6.1. Incremental energy. Let us define an increment form of the energy stored in the medium, according to the assumed time interval given in (73), for the chemo-elastic response by:

$$\widehat{\mathcal{E}}^\tau(\boldsymbol{\varepsilon}^e, d, c) = \int_{t_n}^{t_{n+1}} \left[\frac{d}{dt} \widehat{\mathcal{E}}(\boldsymbol{\varepsilon}^e, d, c) \right] dt = \int_{\mathcal{B}} (W(\mathbf{C}) - W(\mathbf{C}_n)) dV, \quad (74)$$

at the given state \mathbf{C}_n . The incremental energy functional $\widehat{\mathcal{E}}^\tau$ of the field variables \mathbf{C} at the current time t_{n+1} , is governed based on the free energy function W described in (36).

2.6.2. Incremental potential of external loading. Additionally, according to the assumed time interval given in (72), let us define the increment of the external work for the multi-field problem through the following expression for mechanical load:

$$\mathcal{E}_{ext}^{\mathbf{u}, \tau}(\mathbf{u}) := \int_{t_n}^{t_{n+1}} \left[\mathcal{E}_{ext}^{\mathbf{u}, \tau}(\dot{\mathbf{u}}) \right] dt = \int_{\mathcal{B}} \bar{\mathbf{f}} \cdot (\mathbf{u} - \mathbf{u}_n) dV + \int_{\partial_N^{\mathbf{u}} \mathcal{B}} \bar{\boldsymbol{\tau}} \cdot (\mathbf{u} - \mathbf{u}_n) dA, \quad (75)$$

and the external load functional due to the lithium-ion concentration flow contributions by

$$\mathcal{E}_{ext}^{\mu, \tau}(\mu) = \int_{t_n}^{t_{n+1}} \left[\mathcal{E}_{ext}^{\mu, \tau}(\mu) \right] dt = - \int_{\partial_N^\mu \mathcal{B}} \tau \bar{H} \mu dA, \quad (76)$$

which results in the total external loading fro chemical potential through:

$$\mathcal{E}_{ext}^\tau(\mathbf{u}, \mu) = \mathcal{E}_{ext}^{\mathbf{u}, \tau}(\mathbf{u}) + \mathcal{E}_{ext}^{\mu, \tau}(\mu). \quad (77)$$

2.6.3. Incremental dissipation-potential for lithium-ions diffusion. Next, we formulate an incremental dissipation potential in the chemo-elastic medium due to the lithium-ion concentration flow according to the assumed time interval. Note that the convective lithium concentration dissipation potential $\widehat{\Phi}_{Li-ion}(\mathbb{B}, d)$ is evaluated at frozen state d_n of symmetric strain tensor, and fracture phase-field at time t_n , so we have:

$$\widehat{\Phi}_{Li-ion}^\tau(\mathbb{B}, d) \approx \widehat{\Phi}_{Li-ion}^\tau(\mathbb{B}; d_n) = \frac{1}{2} \mathbf{K}(d_n) : (\mathbb{B} \otimes \mathbb{B}), \quad (78)$$

as a result, the incremental dissipation potential functional for lithium-ion concentration flow reads:

$$\mathcal{D}_{Li-ion}^\tau = \int_{t_n}^{t_{n+1}} \left[\int_{\mathcal{B}} -p\dot{c} - \widehat{\Phi}_{Li-ion}(\mathbb{B}, d_n) \right] dt = \int_{\mathcal{B}} -\mu(c - c_n) - \tau \widehat{\Phi}_{Li-ion}^\tau(\mathbb{B}; d_n), \quad (79)$$

at the given state fields d_n . The canonical dissipation functional is governed by the incremental lithium-ion concentration dissipation function $\widehat{\Phi}_{Li-ion}^\tau$ of the field variables $\{c, \mu, d\}$ at the current time t_{n+1} .

2.6.4. Incremental dissipation-potential for fracture. A third incremental dissipation functional is due to the failure mode of chemo-elastic media, in which the incremental dissipation-potential density for fracture evolution reads:

$$\widehat{\Phi}_{frac}^\tau(d, \nabla d; d_n, \nabla d_n) := g_c f(\alpha) \frac{1}{\tau} \left(\gamma(d, \nabla d) - \gamma(d_n, \nabla d_n) \right), \quad (80)$$

and the incremental setting for the viscous response of the fracture evolution expressed through:

$$\widehat{\Phi}_{vis}^\tau(d, \nabla d; d_n, \nabla d_n) := \frac{\eta_d}{2\tau^2} (d - d_n)^2, \quad (81)$$

as a result, the incremental dissipation potential functional for the fracture evolution reads:

$$\begin{aligned} \mathcal{D}_{frac}^\tau(d; d_n) &= \int_{t_n}^{t_{n+1}} \left[\int_{\mathcal{B}} \left(\widehat{\Phi}_{frac} + \widehat{\Phi}_{vis} + I_+(\dot{d}) \right) dV \right] dt \\ &= \int_{\mathcal{B}} \left(\tau \widehat{\Phi}_{frac}^\tau + \tau \widehat{\Phi}_{vis}^\tau + I_+(d - d_n) \right) dV, \end{aligned} \quad (82)$$

at the given state fields $\{d_n, \nabla d_n\}$. The canonical dissipation functional is governed by the incremental fracture evolution dissipation function of the field variables $\{d\}$ at the current time t_{n+1} . Additionally, associated incremental form of KKT conditions at the given time interval for fracture evolution, takes the following form:

$$\beta^d \leq 0, \quad (d - d_n)\beta^d = 0 \quad \text{and} \quad d - d_n \geq 0, \quad \text{with} \quad \nabla d \cdot \mathbf{n}_c = 0 \quad \text{on} \quad \partial\mathcal{B}. \quad (83)$$

Thus, the total incremental dissipation potential due to the lithium-ion concentration flow, and fracture evolution becomes:

$$\mathcal{D}^\tau(c, \mu, d) = \mathcal{D}_{Li-ion}^\tau(c, \mu; d) + \mathcal{D}_{frac}^\tau(d).$$

Formulation 2.3 (Reduced incremental energy functional for the fracturing chemo-elastic media). Consider an open bounded domain \mathcal{B} with boundary $\partial\mathcal{B} = \partial^u\mathcal{B} \cup \partial^\mu\mathcal{B}$. Let constants $(K, \mu, g_c, l_d, \eta_d, D, R, \Omega_c, N_L) \geq 0$ at the constant ambient temperature ϑ be given with the initial conditions $\mathbf{u}_0 = \mathbf{u}(\mathbf{x}, 0)$, $d_0 = d(\mathbf{x}, 0)$, $\mu_0 = \mu(\mathbf{x}, 0)$, and $c_0 = c(\mathbf{x}, 0)$. For the loading increments $n = 1, 2, \dots, N$, find $\mathbf{u} := \mathbf{u}_{n+1} \in \mathcal{W}_u^u$, $d := d_{n+1} \in \mathcal{W}_{d_{n-1}}^d$, $\mu := \mu_{n+1} \in \mathcal{W}_\mu^\mu$, and $c := c_{n+1} \in \mathcal{W}^c$ such that the following incremental potential on the finite time increment $[t_n, t_{n+1}]$:

$$\begin{aligned} \Pi^\tau(\boldsymbol{\varepsilon}^e, d, c, p) &:= \int_{t_n}^{t_{n+1}} \Pi(\boldsymbol{\varepsilon}^e, \dot{d}, \dot{c}, p) dt \\ &= \widehat{\mathcal{E}}^\tau(\boldsymbol{\varepsilon}^e, d, c) + \mathcal{D}^\tau(\boldsymbol{\varepsilon}^e, d, \dot{c}) + \mathcal{E}_{ext}^\tau(\mathbf{u}, p) \\ &= \int_{\mathcal{B}} \left(W(\mathbf{C}) - W(\mathbf{C}_n) \right) dV \\ &\quad + \int_{\mathcal{B}} -\mu(c - c_n) - \tau \widehat{\Phi}_{Li-ion}^\tau(\mathbb{B}; \boldsymbol{\varepsilon}_n^e, d_n) \\ &\quad + \int_{\mathcal{B}} \left(\tau \widehat{\Phi}_{frac}^\tau + \tau \widehat{\Phi}_{vis}^\tau + I_+(d - d_n) \right) dV \\ &\quad - \int_{\mathcal{B}} \bar{\mathbf{f}} \cdot (\mathbf{u} - \mathbf{u}_n) dV - \int_{\partial_N^u \mathcal{B}} \bar{\boldsymbol{\tau}} \cdot (\mathbf{u} - \mathbf{u}_n) dA \\ &\quad - \int_{\partial_N^\mu \mathcal{B}} \tau [\mathbb{H} \cdot \mathbf{n} - \bar{H}] \mu dA, \end{aligned}$$

at the given state is minimized.

Through the incremental potential given in Formulation (2.3) at hand, the time-discrete counterpart of the canonical rate-dependent variational principle in (67) takes the following compact form:

$$(\boldsymbol{\varepsilon}^e, d, c, \mu) = \arg \left\{ \inf_{\mathbf{u} \in \mathcal{W}_u^u} \inf_{\theta \in \mathcal{W}^\theta} \sup_{\mu \in \mathcal{W}_\mu^\mu} \inf_{d \in \mathcal{W}_{dn}^d} \Pi^\tau(\boldsymbol{\varepsilon}^e, d, c, \mu) \right\}, \quad (84)$$

that is the incremental reduced mixed variational saddle-point principle for the crack phase-field chemo-elastic media. Taking the variation of the potential given in Formulation (2.3) yields the incremental form of the Euler equations of the variational principle by:

Balance of linear momentum :	$\delta \Pi_{\boldsymbol{\varepsilon}^e} \equiv -\operatorname{div}\left[\frac{\partial W}{\partial \boldsymbol{\varepsilon}^e}\right] = \bar{\mathbf{f}}$	in \mathcal{B} ,
Constitutive of lithium chemical:	$\delta \Pi_c \equiv \frac{\partial W}{\partial c} - \mu = 0$	in \mathcal{B} ,
Balance of lithium-ion diffusion:	$\delta \Pi_\mu \equiv -\tau \operatorname{div}\left[\frac{\partial \hat{\Phi}_{Li-ion}^\tau}{\partial \mathbb{B}}\right] - (c - c_n) = 0$	in \mathcal{B} ,
Fracture evolution:	$\delta \Pi_d \equiv \frac{\partial W}{\partial d} - \operatorname{div}\left[\frac{\partial \hat{\Phi}_{frac}^\tau}{\partial \nabla d}\right] + \frac{\partial \hat{\Phi}_{frac}^\tau}{\partial \dot{d}} + \frac{\partial \hat{\Phi}_{vis}^\tau}{\partial d} \ni 0$	in \mathcal{B} ,
Traction boundary condition:	$\delta \Pi_{\boldsymbol{\varepsilon}^e} \equiv \frac{\partial W}{\partial \boldsymbol{\varepsilon}^e} \cdot \mathbf{n} = \bar{\boldsymbol{\tau}}$	on $\partial_N^u \mathcal{B}$,
Flux boundary condition:	$\delta \Pi_\mu \equiv \tau \frac{\partial \hat{\Phi}_{Li-ion}^\tau}{\partial \mathbb{B}} \cdot \mathbf{n} = \tau \mathbb{H} \cdot \mathbf{n} = \tau \bar{H}$	on $\partial_N^H \mathcal{B}$,
Phase-field boundary conditions:	$\delta \Pi_d \equiv \frac{\partial \hat{\Phi}_{frac}^\tau}{\partial \nabla d} \cdot \mathbf{n} = 0$	on $\partial \mathcal{B}$.

2.7. Variational equations through reduced incremental energy functional

Now we are able to elaborate the variational equations through reduced incremental energy functional for the fracturing chemo-elastic media. This would be lithium-ion concentration flow, elasticity equation and finally follows with fatigue fracture.

2.7.1. Lithium-ion concentration flow. First, we describe the governing equations and variational formulation for the lithium-ion concentration flow.

Governing equations. By employing the Coleman-Noll inequality condition in thermodynamics, the lithium chemical potential μ is derived from the first-order derivative of the pseudo-energy density function W given in (36) with the elastic part in (24), and lithium-ion density function in (30), so

$$\mu(\boldsymbol{\varepsilon}^e, c) \approx \mu(\boldsymbol{\varepsilon}, \boldsymbol{\varepsilon}^c, \Theta_L) := \frac{\partial W}{\partial c} = \mu_0 + R\vartheta \left(\ln \Theta_L - \ln(1 - \Theta_L) \right) - \Omega_c \sigma_h. \quad (85)$$

Here, σ_h is the hydrostatic stress that is defined through $\sigma_h = \frac{1}{3} \operatorname{tr}(\boldsymbol{\sigma})$. For a detailed derivation see Appendix A. It has been shown that, the hydrostatic stress has the potential

to boost both the acceleration and improvement of lithium diffusion, resulting in a higher state of charge, which serves as a representative measure of the percentage of full capacity [96]. However, by means of (85) and (27) lithium-ion flux vector reads:

$$\mathbb{H} = -\mathbf{K}(c, d) \nabla \mu = -\frac{g(d)D}{1 - \Theta_L} c \left(\frac{\nabla c}{c} - \frac{\nabla N_L}{N_L} \right) + \frac{g(d)D}{R\vartheta} c \Omega_c \nabla \sigma_h. \quad (86)$$

Thus, we have the following:

$$\mathbb{H} = \mathbf{K}\mathbb{B} = -g(d)D\nabla c + \frac{g(d)D}{R\vartheta} c \Omega_c \nabla \sigma_h. \quad (87)$$

where, as mentioned before constant interstitial sites concentration, and $\Theta_L \ll 1$ is imposed. For a detailed derivation see Appendix A. Employing the above-mentioned identity between lithium flux vector and lithium concentration field in addition to the (29), the conservation of mass takes the following form

$$\frac{c - c_n}{\tau} - \text{Div}[\mathbb{H}] = \frac{c - c_n}{\tau} + \text{Div}[D\nabla c] - \text{Div}\left[\frac{D}{R\vartheta} c \Omega_c \nabla \sigma_h\right] = 0, \quad (88)$$

which now *fully* depends on the lithium-ion field (c, c_n) and not lithium-ion chemical potential μ . Note that here the identity (42) is used.

Variational equation. The directional derivative of Π^τ given in Formulation(2.3) with respect to the lithium chemical potential μ reads:

$$\begin{aligned} \Pi_\mu^\tau(\mathfrak{U}, \delta\mu) &= \int_{\mathcal{B}} \left[\left((c - c_n) \right) \delta\mu + (\tau \mathbf{K}\mathbb{B}) \cdot \delta\nabla\mu \right] dV \\ &\quad + \int_{\partial_N^{\mu} \mathcal{B}} \tau \bar{H} \delta\mu dA = 0, \quad \forall \delta\mu \in \mathcal{W}_0^\mu, \end{aligned} \quad (\text{C})$$

which is solved for on lithium-ion concentration field.

2.7.2. Elasticity. Next, we illustrate the governing equations and variational formulation for the mechanical counterpart.

Governing equations. Following the Coleman-Noll procedure, the stress tensor is obtained from the potential W_{elas} in (24) as

$$\boldsymbol{\sigma} = \frac{\partial W}{\partial \boldsymbol{\varepsilon}} = \frac{\partial W_{elas}}{\partial \boldsymbol{\varepsilon}} = g(d) \tilde{\boldsymbol{\sigma}}_+ + \tilde{\boldsymbol{\sigma}}_-, \quad (89)$$

where damageable $\tilde{\boldsymbol{\sigma}}_+$ and undamageable $\tilde{\boldsymbol{\sigma}}_-$ contributions of stress are given by

$$\begin{aligned} \tilde{\boldsymbol{\sigma}}_+ &:= \frac{\partial \psi_e^+}{\partial \boldsymbol{\varepsilon}} = KH^+[I_1](\boldsymbol{\varepsilon}^e : \mathbf{I})\mathbf{I} + 2\mu \boldsymbol{\varepsilon}^{e,dev}, \\ \tilde{\boldsymbol{\sigma}}_- &:= \frac{\partial \psi_e^-}{\partial \boldsymbol{\varepsilon}} = K(1 - H^+[I_1])(\boldsymbol{\varepsilon}^e : \mathbf{I})\mathbf{I}. \end{aligned} \quad (90)$$

Variational equation. The minimization with respect to the displacement field in the variational principle (84) yields

$$\begin{aligned} \Pi_u^\tau(\mathfrak{U}; \delta\mathbf{u}) &= \int_{\mathcal{B}} [\delta_{\boldsymbol{\varepsilon}}(W_{elast} + W_{Li-ion}) : \boldsymbol{\varepsilon}(\delta\mathbf{u})] dV \\ &= \int_{\mathcal{B}} [\boldsymbol{\sigma} : \boldsymbol{\varepsilon}(\delta\mathbf{u}) - \bar{\mathbf{f}} \cdot \delta\mathbf{u}] dV - \int_{\partial \mathcal{B}_N^u} \bar{\boldsymbol{\tau}} \cdot \delta\mathbf{u} dA = 0 \quad \forall \delta\mathbf{u} \in \mathcal{W}_0^u, \end{aligned} \quad (\text{E})$$

which corresponds to the weak form of the mechanical balance equations, with \mathcal{W}_0^u denotes the function space for the virtual displacement fields, i.e., with homogeneous kinematic boundary conditions.

2.7.3. Damage. Since, we have $\widehat{\Phi}_{Li-ion}(\mathbb{B}, d) \approx \widehat{\Phi}_{Li-ion}(\mathbb{B}; d_n)$ which results in the identity $\delta_d \widehat{\Phi}_{Li-ion}(\mathbb{B}; d_n) = 0$. The directional derivative of (37) with respect to the crack phase-field can be written as

$$\begin{aligned}\Pi_d^\tau(\mathbf{U}; \delta d) &= \int_{\mathcal{B}} \left[\partial_d (W_{elas} + \widehat{\Phi}_{vis}^\tau) : \delta \boldsymbol{\varepsilon} + \delta_d \widehat{\Phi}_{frac}^\tau \delta d \right] dV \\ &= \int_{\mathcal{B}} \left[\left(\frac{\partial g(d)}{\partial d} \psi_e^+ + \frac{\eta_d}{\tau} (d - d_n) + \frac{g_c f(\alpha)}{c_d l_d} \omega'(d) + \partial I_+(d - d_n) \right) \delta d \right. \\ &\quad \left. + \frac{2g_c f(\alpha)}{c_d} l_d (\nabla d \cdot \nabla(\delta d)) \right] dV \ni 0 \quad \forall \delta d \in \mathcal{W}^d,\end{aligned}\quad (91)$$

where the indicator function $I_+ : \mathbb{R} \rightarrow \mathbb{R} \cup \{+\infty\}$ has been introduced to impose the irreversibility condition embedded in $d \in \mathcal{W}_{d_n}^d$, so

$$\partial I_+(d - d_n) = \begin{cases} \{0\} & \text{if } d > d_n, \\ \mathbb{R}_- & \text{if } d = d_n, \\ \emptyset & \text{otherwise.} \end{cases} \quad (92)$$

To enforce the crack irreversibility condition, we define the history field based on maximum crack driving force in time as

$$\mathcal{H}(\mathbf{x}, t) := \max_{s \in [0, t]} \widetilde{D}(\mathbf{C}(\mathbf{x}, s)) \quad \text{with} \quad \widetilde{D} := \zeta \frac{2c_d l_d}{f(\alpha) g_c} \psi_e^+(I_1, I_2) \geq 0, \quad (93)$$

Additionally, $\zeta \geq 0$ is a scaling parameter to further providing relaxation of the formulation, allowing to tune the post-critical range [97]. We note that alternative approach to impose crack irreversibility could be find in [98, 99]

So, (91) is reduced to the following equality equation as:

$$\begin{aligned}\Pi_d^\tau(\mathbf{U}; \delta d) &= \int_{\mathcal{B}} \left[\left((1-d)\mathcal{H} - d + \frac{\eta_d}{\tau} (d - d_n) \right) \delta d - l_d^2 \nabla d \cdot \nabla(\delta d) \right] dV = 0 \\ &\quad \delta d \in \mathcal{W}^d.\end{aligned}\quad (\text{D})$$

We note that to derive above formulation, we divided (91) by $f(\alpha)g_c$ and we further assumed that $\eta_d = \eta_d^0/(f(\alpha)g_c)$ with $\eta_d^0 \ll 1$, which result in choosing η_d as a small quantity similar as a classical phase-field modeling. Therefore, here we set η_d as a small quantity.

2.8. Variational formulations derived for the coupled multi-field problem

The fully coupled variational multi-field problem to describe mechanically induced fatigue fractures in chemo-elasticity media is formulated in (E)-(C)-(D). Thus, the following equation associated with finite time increment $[t_n, t_{n+1}]$ has to be solved. To do so, we need to find, the global primary fields at time t_{n+1} for $\mathbf{u} := \mathbf{u}_{n+1} \in \mathcal{W}_{\bar{u}}^u$, $c := c_{n+1} \in \mathcal{W}_{\bar{c}}^c$,

and $d := d_{n+1} \in \mathcal{W}_{d_{n-1}}^d$ as the solution of the following incremental coupled problem:

$$\Pi^\tau(\boldsymbol{\mathfrak{U}}, \delta\boldsymbol{\mathfrak{U}}) = \underbrace{\Pi^\tau(\boldsymbol{\mathfrak{U}}, \delta\boldsymbol{u})}_{(E)} + \underbrace{\Pi^\tau(\boldsymbol{\mathfrak{U}}, \delta c)}_{(C)} + \underbrace{\Pi^\tau(\boldsymbol{\mathfrak{U}}, \delta d)}_{(D)} = 0 \quad \forall (\delta\boldsymbol{u}, \delta c, \delta d) \in (\mathcal{W}_0^u, \mathcal{W}_0^c, \mathcal{W}^d). \quad (94)$$

In order to solve the chemo-mechanical model that undergoes fatigue failure (94), we first solve (E)-(C) equations monolithically (simultaneously obtain (\boldsymbol{u}, c)). Then, a staggered approach is used to obtain the phase-field fracture d by means of (D). To that end, we fix alternately (\boldsymbol{u}, c) and estimate d and vice versa. The procedure is continued until its convergence (using a given TOL_{Stag}). We provide a summary of the algorithm steps in Algorithm 1.

3. Numerical examples

This section demonstrates the performance of the proposed fatigue failure theory in lithium-ion battery electrode particles. Different boundary value problems are investigated, in which the electrode particles with built-in defects in the form of initial cracks and micro cavities are considered. In order to assess the influence of these defects on the crack behavior, the distribution, size and number of defects are varied. To initiate the fatigue crack, the lithium concentration at the particle surface is cyclically increased and reduced (corresponds to lithiation/delithiation) back to the initial concentration. In general, we have a free boundary condition for the displacement in all directions and the phase-field variable was set equal to 1 at the initial crack surfaces \mathcal{C} .

The material parameters listed in Table 1 are considered, which are used based on [20]. Here, we present quantitative and qualitative indicators to highlight the role of considering fatigue failure for lithium diffusion induced fracture in lithium-ion battery electrode particles. These indicators correspond to: (i) The curve of the accumulated elastic energy-cycles to examine the maximum energy capacity before cracking. (ii) We also look at the crack volume-cycle curve, to examine the final fracture volume within the electrode particle. (iii) Qualitative response of crack phase-field pattern to highlight the effects of the damage response over time. This is augmented with the lithium concentration solution within the electrode particle. (iv) Lastly, to investigate the softening process during lithiation/delithiation, the fatigue degradation function for a point around the crack tip within the electrode particle is examined.

Space discretization. In the numerical simulations, the global primary variables are discretized using finite element basis functions, with bilinear quadrilateral Q_1 elements for the two-dimensional problems, and trilinear hexahedral H_1 elements for the three-dimensional problems.

Model parameters. To promote stability, an artificial residual stiffness is introduced and set to $\kappa_d = 1 \times 10^{-8}$. The length scale is defined as $l_d = 2h_{\min}$, where h_{\min} is the smallest element size.

Solution of the nonlinear problems. Here, the Krylov method solver is used in which the linear equation systems are solved with a generalized minimal residual method (GMRES), while the LU factorization is used as a preconditioner. Here the default solver

Algorithm 1 *The staggered iterative solution process for (94) at a fixed time-step n .*

Input: loading data $(\bar{\mathbf{f}}, \bar{\mathbf{t}}_n)$ on \mathcal{C} and Γ_N , respectively;

solution $(\mathbf{u}_{n-1}, c_{n-1}, d_{n-1}; \alpha_{n-1})$ from step $n - 1$.

Initialization, $k = 1$:

- set $(\mathbf{u}_0, c_0, d_0) := (\mathbf{u}_{n-1}, c_{n-1}, d_{n-1})$.

Staggered iteration between (\mathbf{u}, c) and d :

- solve following system of equations for (E)-(C) in a monolithic manner given d_{k-1} ,

$$\begin{cases} \Pi_{\boldsymbol{\varepsilon}_e}^\tau(\mathbf{u}, c, d_{k-1}; \delta \mathbf{u}) = 0, \\ \Pi_\mu^\tau(\mathbf{u}, c, d_{k-1}; \delta \mu) = 0, \end{cases}$$

for (\mathbf{u}, c) , set $(\mathbf{u}, c) =: (\mathbf{u}_k, c_k)$,

- given (\mathbf{u}_k, c_k) , obtain μ from (85),
- given (c_k, d_k) , obtain $\mathbb{H} = -\mathbf{K}(c, d) \nabla \mu = \mathbf{K}\mathbb{B}$ from (87),
- given (\mathbf{u}_k, c_k) , solve (D) by $\Pi_d^\tau(\mathbf{u}_k, c_k, d; \delta d) = 0$ for d , set $d =: d_k$,
- given (\mathbf{u}_k, c_k, d_k) , determine $\vartheta(\boldsymbol{\varepsilon}, c, d)$ to find α from (51) set $\alpha =: \alpha_k$,
- for the obtained pair (\mathbf{u}_k, c_k, d) , check staggered residual by

$$\text{Res}_{\text{Stag}}^k := |\Pi_{\boldsymbol{\varepsilon}}^\tau(\mathbf{u}_k, c_k, d_k; \delta \mathbf{u})| + |\Pi_\mu^\tau(\mathbf{u}_k, c_k, d_k; \delta \mu)| \leq \text{TOL}_{\text{Stag}}, \quad \forall (\delta \mathbf{u}, \delta \mu) \in (\mathcal{W}_0^\mathbf{u}, \mathcal{W}_0^\mu),$$

- if fulfilled, set $(\mathbf{u}_k, c_k, d_k) =: (\mathbf{u}_n, c_n, d_n)$ then stop;

else $k + 1 \rightarrow k$.

Output: solution $(\mathbf{u}_n, c_n, d_n; \alpha_n)$ at n^{th} time-step.

tolerances and maximum number of iterations are used (see Table 2). The matrix type is managed by the *multifrontal massively parallel sparse* direct solver package (MUMPS), which is well suited for distributed matrices and systems with huge numbers of degrees of freedom. For a more detailed discussion, see [100, 101].

Software. The implementation is based on FEniCSx 0.6.1 and the imported mesh is created via GMSH 4.11.4. The FEniCSx docker container already includes MPICH and is fundamentally developed for parallel processing on laptops, workstations and also HPC clusters. The user can define the PDEs in PYTHON that FEniCSx translates via FFCx into a low-level C code, enabling the compilation of highly efficient simulations. The workload in the LUIS HPC cluster is managed by SLURM 22.05.3.

Table 1: Material/model parameters used in the numerical examples based on [20]

No.	Parameter	Name	Value	Unit
1.	K	Bulk modulus	77.5	GPa
2.	μ	Shear modulus	35.77	GPa
3.	D	Lithium diffusion coefficient	7.08×10^{-15}	$\text{m}^2 \cdot \text{s}^{-1}$
4.	R	Universal Gas constant	8.314	$\text{J} \cdot \text{K}^{-1} \cdot \text{mol}^{-1}$
5.	Ω_c	Partial molar volume of lithium	$2.4 \cdot 10^{-6}$	$\text{m}^3 \times \text{mol}^{-1}$
6.	N_L	Number of moles of lattice sites	6.022×10^{23}	mol^{-1}
7.	ϑ	Ambient temperature	300	K
8.	g_c	Griffith's energy release rate	1	MPa · mm
9.	ζ	Scaling factor	1	—
10.	η_d	Fracture viscosity	10^{-6}	$\text{N}/\text{m}^2\text{s}$
11.	κ_d	Stabilization parameter	10^{-8}	MPa
12.	l_f	Fracture length-scale	5×10^{-6}	mm
13.	k_f	Fatigue model parameter	0.5	mm
14.	α_c	Fatigue threshold parameter	3.333×10^3	mm
15.	c_0	Initial concentration	300	$\text{mol} \cdot \text{m}^{-3}$
16.	Δt	Time increment	200	s

Table 2: Numerical parameters for the used Krylov method solver.

No.	Parameter	value
1.	relative convergence tolerance	1×10^{-5}
2.	absolute convergence tolerance	1×10^{-50}
3.	divergence tolerance	1×10^4
4.	maximum number of iterations	1×10^4

3.1. Example 1: Lithium diffusion induced crack driven for single notch

In the first numerical example, the influence of the electrode particle shape on the cracking behavior is investigated by varying the height or width of the particle, thus varying the aspect ratio. We define the aspect ratio of the ellipsoidal shape through $\chi = D_{long}/D_{trans}$ which represents the ratio of the longitudinal diameter D_{long} versus the transverse diameter D_{trans} . In the first example, the radius of the electrode particle

equals $r = 6 \times 10^{-5}$ mm. Also, an initial crack is located in the center of the particle with a length of $C_1 = 3 \times 10^{-5}$ mm, see Figure 6(a). In the cyclic charge and discharge, the lithium concentration reaches a maximum value of $c_{max} = 510000$ mol/m³ with an increment of $\Delta c = 170000$ mol/m³ (see Figure 7). The number of quadrilateral elements ranges from 19800 up to 25100 as the area of electrode particles varies with changing aspect ratio and since the length scale, i.e., l_f , should be kept approximately the same.

The evolution of the crack phase-field and normalized lithium concentration c/c_{max} distributions up to complete failure are shown in Figures 8 and 9. It is evident from the crack patterns that the electrode particle geometry has a great impact on the cracking behavior. In general, it can be observed that the cracks develop at the surface and grow towards the center. This is because the lithium concentration at the surface is increased rapidly in a short time so that the concentration in the core of the domain remains almost unchanged. In contrast, a large concentration gradient can be seen at the edges, which leads to a high local tensile stress. The crack at particle's aspect ratios below $\chi \leq 0.8$ grows vertically and propagates horizontally at ratios with more than $\chi > 0.8$. At the end of the simulation with particle's aspect ratios of 0.6 and 0.8, the nucleation of the secondary cracks can be observed. From the results in Figure 9 it can be seen that the lithium concentration is lowest along the cracks. Additionally, a radially increasing lithium concentration can be observed along the crack path, as shown in Figure 9. In fact, the lithium concentration gradient is much smaller along the crack than perpendicular to the crack, resulting in a uniform shape in the fracture domain.

The evolution of the corresponding crack volume and fatigue degradation functions are shown in Figure 10. Investigating different aspect ratios of electrode particles confirms that $\chi = 0.6$ shows the lowest crack propagation and thus demonstrates its superiority in comparison to others. The fastest crack propagation is at aspect ratio $\chi = 1$. However, the aspect ratio of $\chi = 0.8$ generally exhibits the highest crack volume. In line with the findings of the crack volumes, it can also be seen from the fatigue degradation functions that the softening process is slowest for the aspect ratio $\chi = 0.6$.

The accumulated elastic energy is represented in Figure 11 which indicates that the electrode particle with an aspect ratio of $\chi = 0.6$ requires significantly more cycles compared to the other aspect ratios in order to reduce the elastic energy due to the crack propagation. For instance, aspect ratio $\chi = 0.6$ requires over 15000 cycles, whereas aspect ratio $\chi = 1$ shows a rapid drop in elastic energy even before 2000 cycles.

It is noteworthy that the crack phase-field indicated in Figure 8 with aspect ratio $\chi = 1.2$ has a similar pattern compared to the CT results provided by the experiment shown in the top right corner of Figure 2. The same can be said for the results in Figure 3 when compared to different aspect ratios.

3.2. Example 2: Lithium diffusion-induced crack driven for single notch with distributed micro cavities

In the second example, in addition to the crack in the center of the electrode particle, micro cavities (micro pores) are considered, which are randomly distributed, see Figure 6. In this example, the radius of the electrode particle is $r = 6 \times 10^{-5}$ mm, the same as the first example, with a pre-defined notch located in the center of a particle with the length of $C_1 = 3 \times 10^{-5}$. In Case 1, the micro cavities have a uniform radius of $r_1 = 5 \times 10^{-6}$ which are distributed randomly in the particle. In Case 2, the positions of

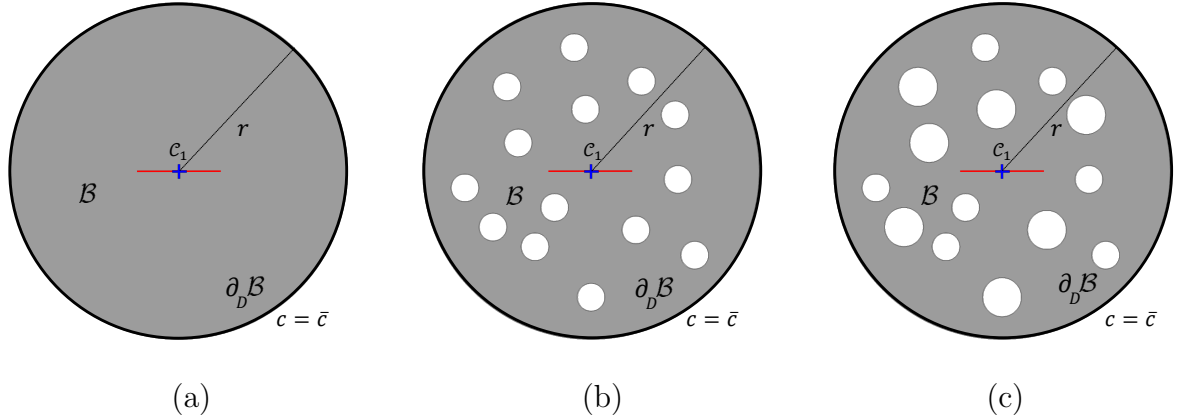


Figure 6: The representation of the geometry and boundary conditions for (a) Example 1, (b) Example 2 (Case 1), and (c) Example 2 (Case 2).

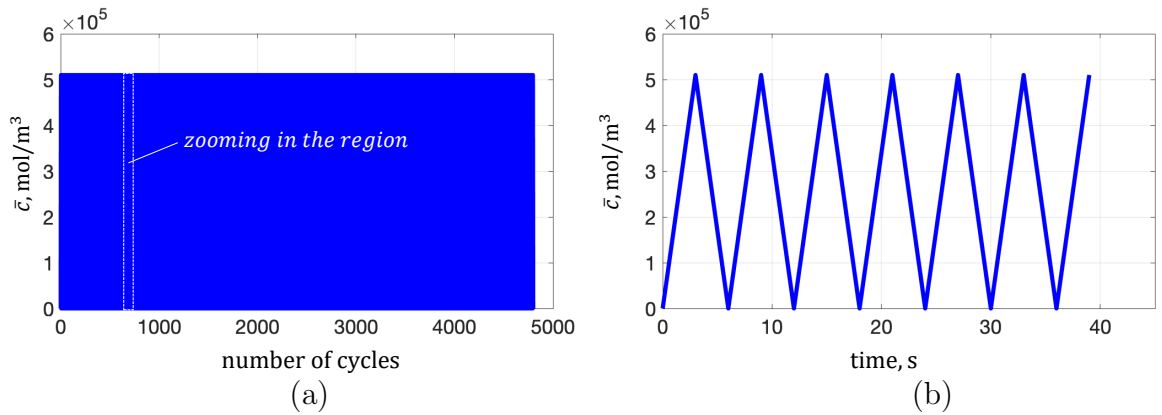


Figure 7: Example 1. Cyclic lithium concentration load (lithiation/delithiation) for (a) the entire time steps, and (b) zooming into the specific time to indicate lithiation/delithiation process.

the micro cavities are not changed, while two different sizes of micro cavities are chosen. As a result, two micro cavities with a radius of $r_1 = 5 \times 10^{-6}$, and $r_2 = 7 \times 10^{-6}$ are considered. This is to illustrate the influence of the pore size on the crack pattern, without the pore position being decisive. At the boundary, the electrode particles are cyclically charged due to lithiation with an lithium concentration increment of $\Delta c = 123333 \text{ mol/m}^3$ until the maximum concentration of $c_{max} = 370000 \text{ mol/m}^3$. A following discharging process decreases the lithium concentration back to the initial stage, see Figure 12. In this example, the number of bilinear quadrilateral elements for Case 1 and Case 2 is 23300.

The evolution of the crack pattern and of the normalized lithium concentration c/c_{max} distribution are shown in Figure 13 for Case 1, and in Figure 14 for Case 2. In both cases, cracks initiate from the pre-defined crack and also micro cavities, which merge later on. In Case 2, another impacting factor that should be noted is the nucleation of cracks around the bigger cavities that merged with the main crack. It is also observed that the lithium concentration again has the lowest values along the crack paths. The crack volumes, fatigue degradation functions and the storage elastic energy of both Case 1 and Case 2 are depicted in Figure 15 and Figure 16, respectively.

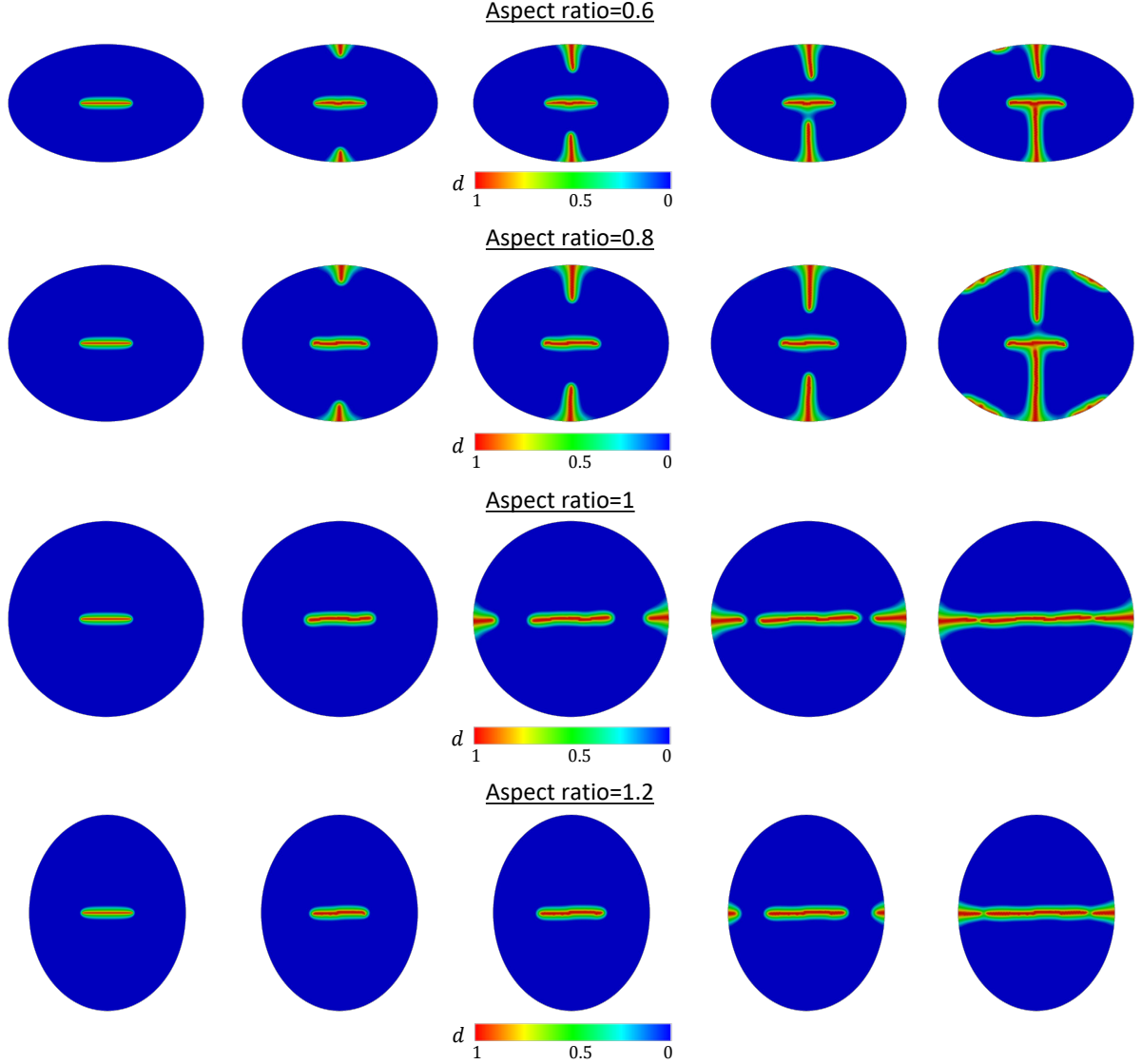


Figure 8: Example 1. Evolution of crack phase-field in electrode particles with different aspect ratios $\chi \in \{0.6, 0.8, 1, 1.2\}$.

3.3. Example 3: Lithium diffusion-induced crack driven for distributed micro notches

In the third example, we investigate the influence of several randomly distributed pre-defined cracks, see Figure 17. In this example, the radius of the electrode particle is $r = 6 \times 10^{-5}$ mm, identical to the other examples. Here, we encounter three different cases. In Case 1, we have 4 symmetrically pre-defined cracks of length $C = 3 \times 10^{-5}$ mm. In Case 2, 4 pre-defined cracks are randomly distributed with the same length as in Case 1. In the last case, we have twice as many cracks of half length, i.e., $C = 1.5 \times 10^{-5}$ mm. These are also randomly distributed. By doing so, we can clarify the influence of initial cracks on the electrode particles and on the lifespan of the lithium-ion battery. In this example, the electrode particles are cyclically loaded at the boundary with an lithium concentration increment of $\Delta c = 86666$ mol/m³ up to $c_{max} = 260000$ mol/m³ and unloaded again to the initial concentration, see Figure 12. Accordingly, the number of bilinear quadrilateral elements for all meshes is approximately 24500 elements.

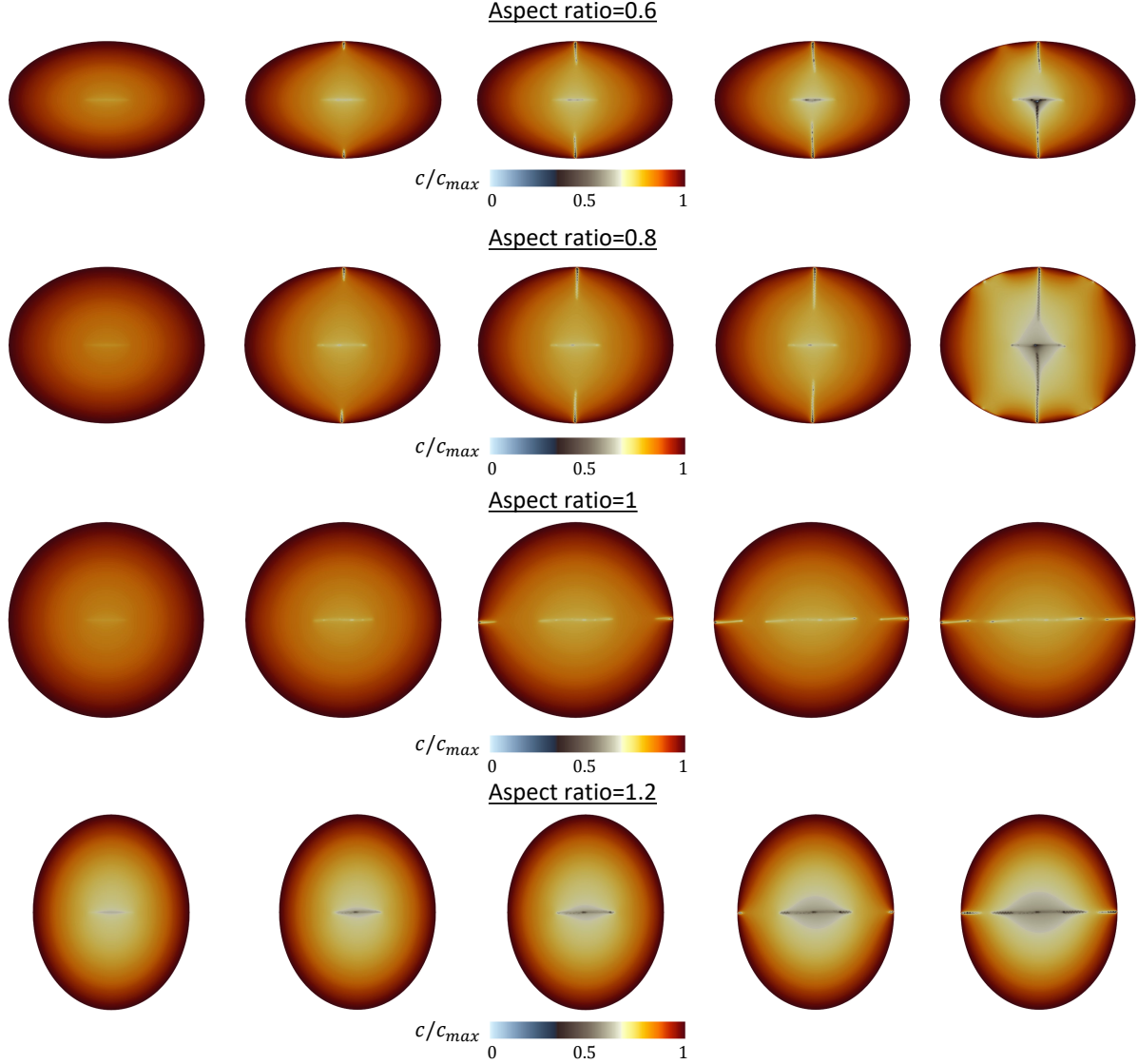


Figure 9: Example 1. Development of the lithium concentration in electrode particles with different aspect ratios $\chi \in \{0.6, 0.8, 1, 1.2\}$.

The nucleation and evolution of the crack phase-field and the normalized lithium concentration c/c_{max} for the different cases are depicted in Figure 18 and Figure 19. In Case 1, it can be grasped that the crack formation not only initiates at the boundary, but now also propagates between the initial cracks. In Case 2, no crack nucleation arising from the boundary can be seen, but propagation and merging through pre-defined cracks can be observed, which eventually grow towards the surface.

In Case 3, crack nucleation occurs where the initial crack is near the boundary of the electrode particle. Upon reaching complete failure, branching of the crack can be observed. So, the mathematical framework proposed here is capable to simulate complex fracture phenomena, such as merging and branching of the crack surface. Additionally, it is evident that the lithium concentration has the lowest values especially along the crack region, which is in agreement with the previous examples.

In Figures 20 and Figure 21 the crack volumes, fatigue degradation functions, as well

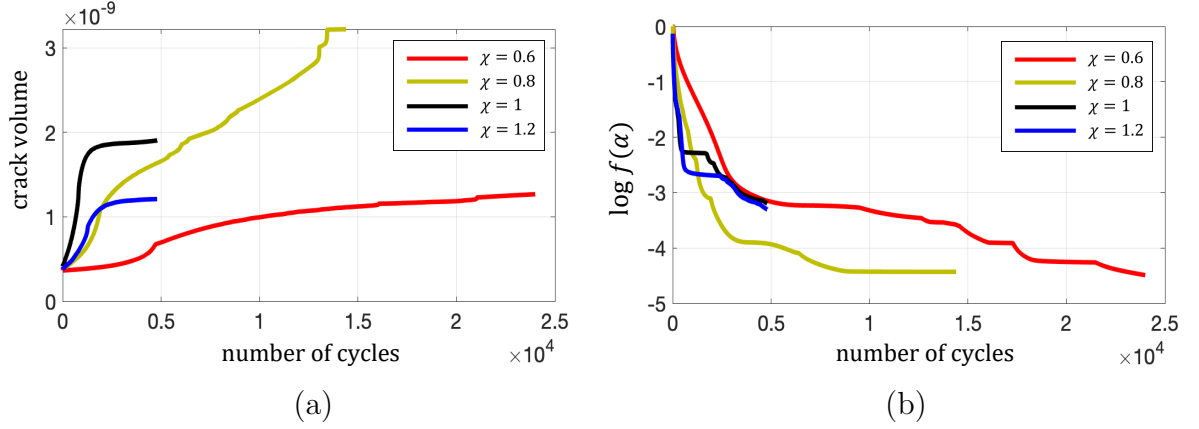


Figure 10: Example 1. Evaluation of (a) the crack volumes and (b) fatigue degradation functions for an arbitrary Gaussian integration point for electrode particles with different aspect ratios.

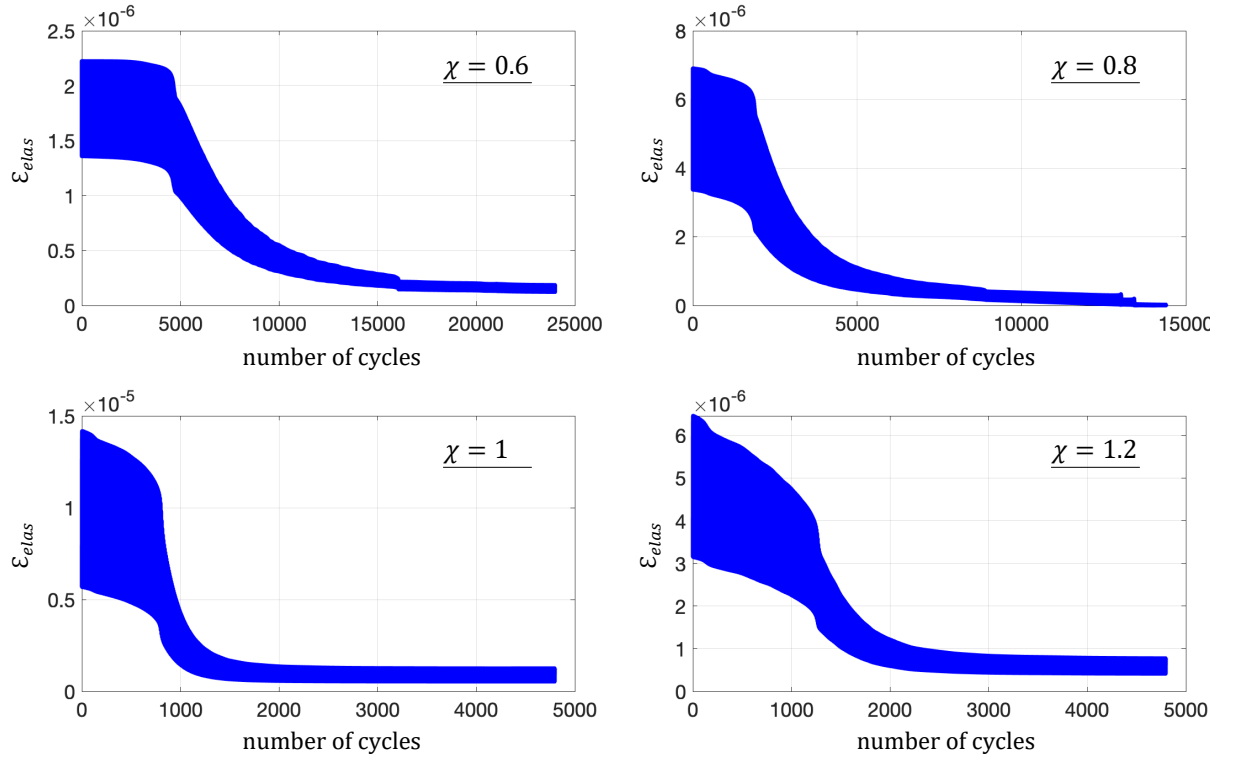


Figure 11: Example 1. The accumulated elastic energy functional for electrode particles with different aspect ratios.

as accumulated the elastic energy are depicted. It is worth noting that in Case 1, a sudden increase in crack volume is observed due to the micro notches/defects being closer to each other compared to the other cases. This rapid crack propagation can also be recognized by the rapid drop in elastic energy. Following the sudden changes in crack volume, a steady state is quickly reached, with no further discernible alterations in crack volume.

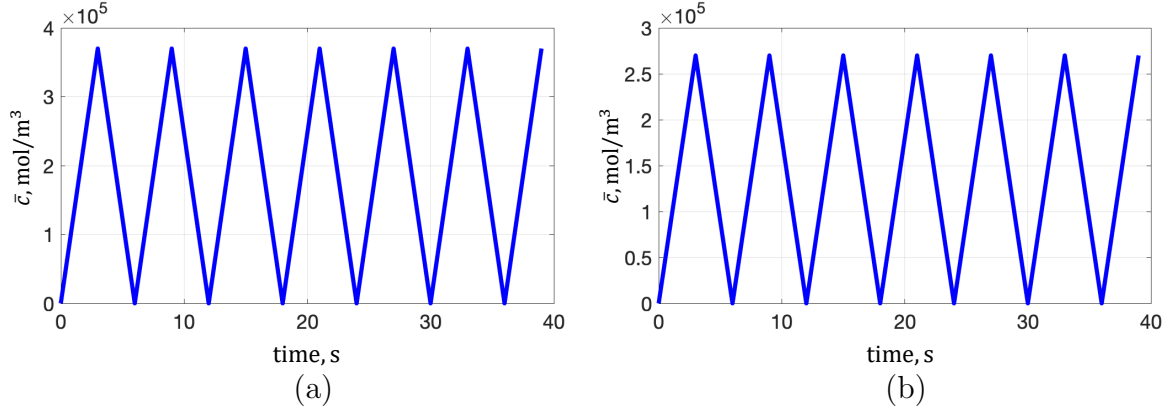


Figure 12: Cyclic lithiation/delithiation concentration load for (a) Example 2, and (b) Example 3.

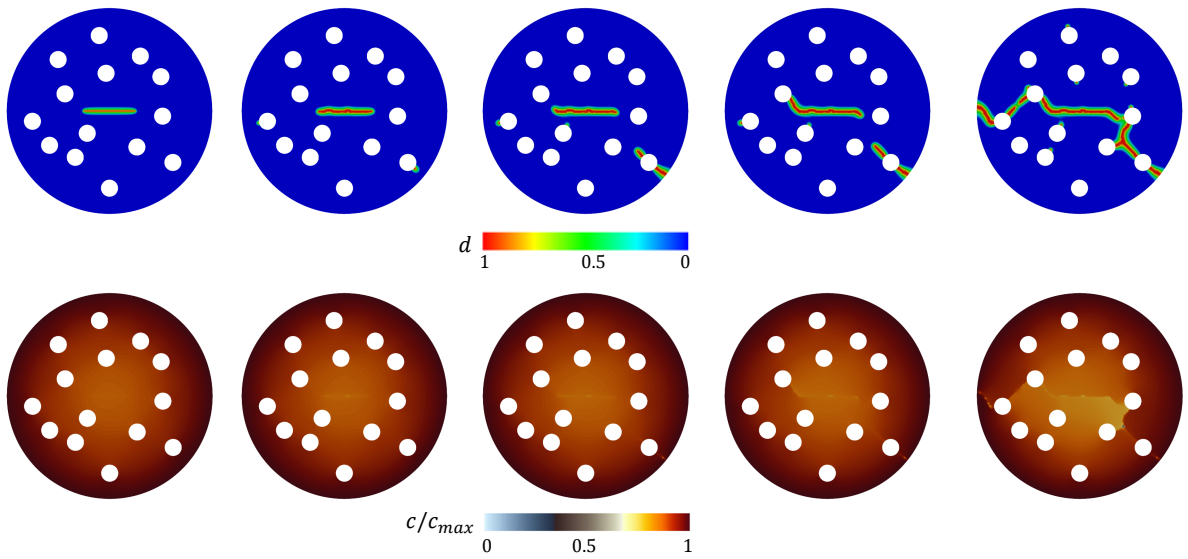


Figure 13: Example 2 (Case 1). Evolution of crack phase-field and lithium concentration in electrode particles with cavities of one size.

3.4. Example 4: Three-dimensional Lithium diffusion-induced crack driven for multiple distributed notches

Finally, the last example examines the results achieved with the proposed model in the three-dimensional environment. Here, lithium diffusion-induced crack, driven by multiple distributed notches, is considered, see Figure 22. In this example, the radius of the electrode particle is $r = 6 \times 10^{-5}$ mm, identical to the two-dimensional examples. Here, two different cases are considered. We investigated 8 randomly distributed circular cracks in Case 1 (Figure 22(a)) and 14 in Case 2 (Figure 22(b)). These micro cavities are randomly placed with a radius of $r_1 = 7.5 \times 10^{-6}$ mm, so $\mathcal{C} = 1.76 \times 10^{-10}$ mm². In this example, the electrode particles are cyclically loaded at the boundary with a lithium concentration increment $\Delta c = 120000$ mol/m³ to $c_{max} = 480000$ mol/m³ and unloaded again to the initial concentration, see Figure 22 (c). Accordingly, we have used for Case 1, 248 726, and Case 2, 255 511 H_1 elements for this setup. Since the rate-dependent problem

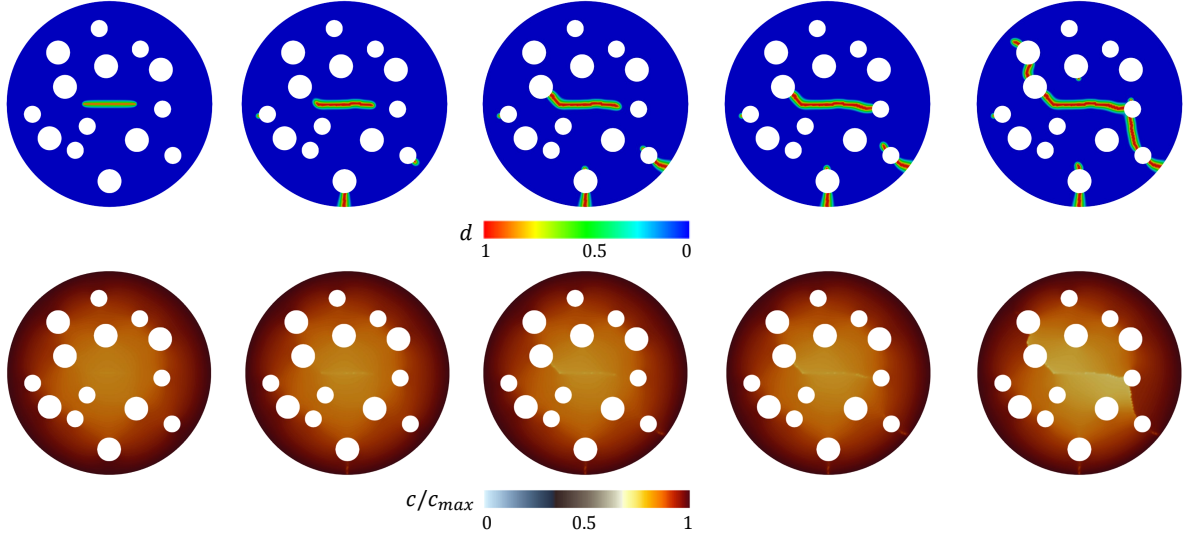


Figure 14: Example 2 (Case 2). Evolution of crack phase-field and lithium concentration in electrode particles with cavities of two sizes.

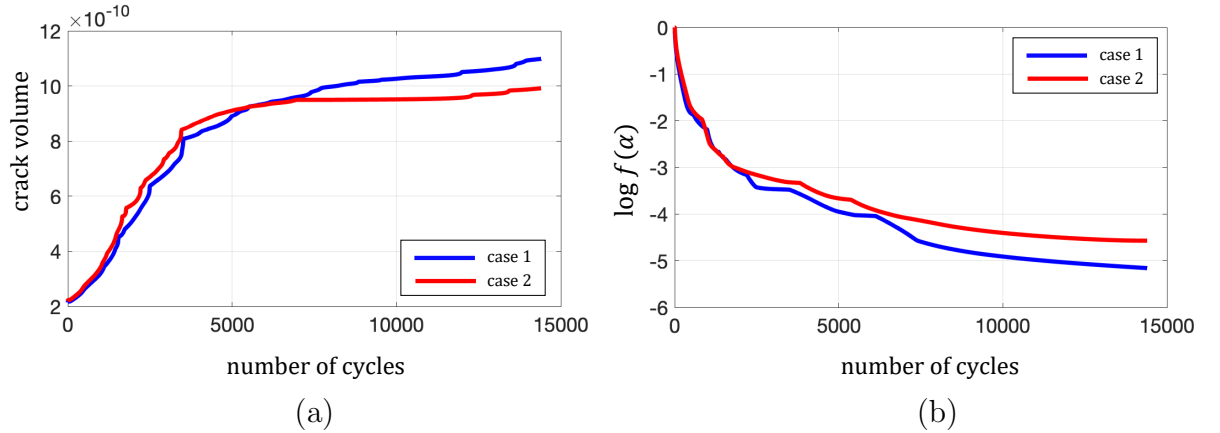


Figure 15: Example 2. Evaluation of the crack volumes and fatigue degradation functions for an arbitrary Gaussian integration point for (a) Case 1 and (b) Case 2.

is considered here, we set $\Delta t = 500/\text{s}$ for the time increment of the cyclic charge/discharge process.

Our goal here is to investigate the performance of the proposed formulation in the three-dimensional setting. Specifically, the influence of the micro cavities in the real three-dimensional electrode particle on the lifespan of the lithium-ion battery is briefly reported. The evolution of the crack phase-field d as well as the normalized lithium concentration c/c_{max} are provided for Case 1 in Figure 23, and for Case 2 in Figure 24 at six deformation stages up to the final failure.

In both cases, the crack initiates at the tip of multiple pre-defined micro cavities and continues to propagate towards merging. But in Case 2 more micro notches are involved for nucleation and crack propagation. The crack branching at different stages can also be observed, with the complex three-dimensional crack structure being represented as an isosurface with $\{\hat{d} := 1 \text{ if } d \geq 0.99 \text{ otherwise } \hat{d} := 0\}$, see Figure 23, and Figure

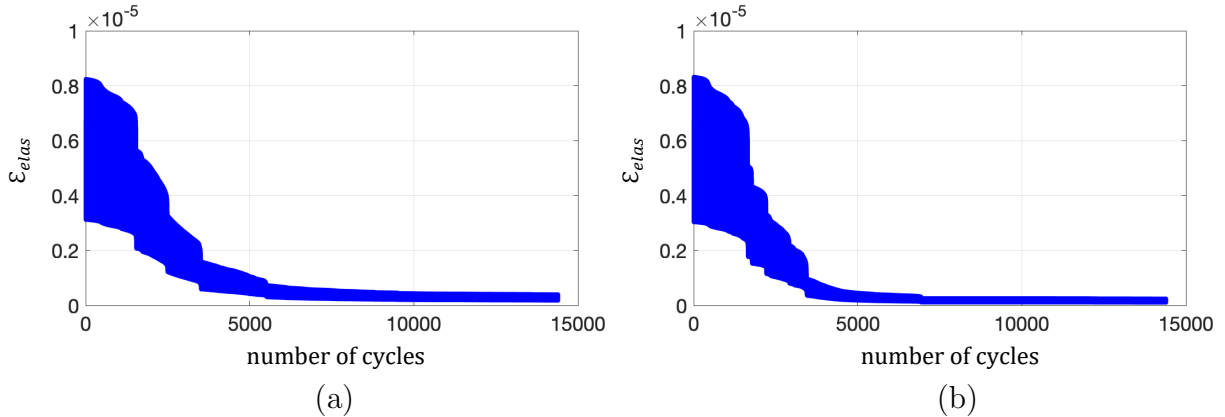


Figure 16: Example 2. The accumulated elastic energy functional for (a) Case 1, and (b) Case 2.

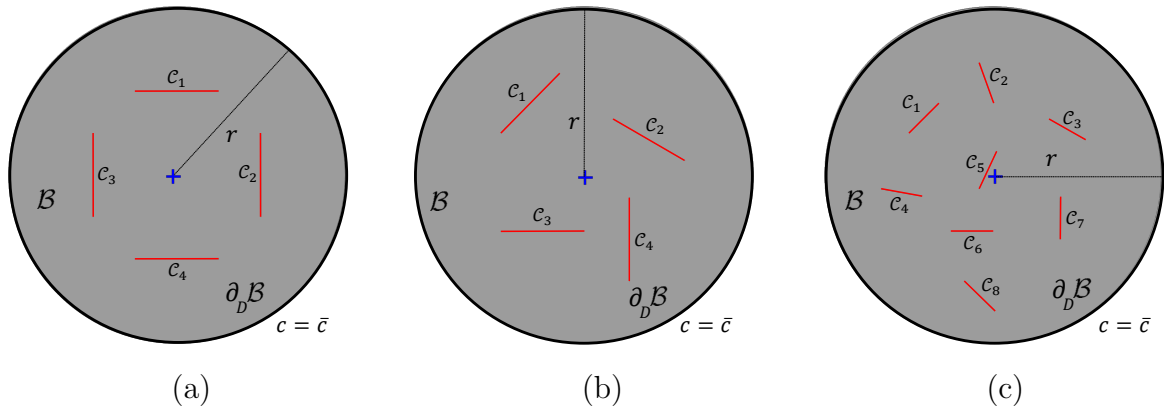


Figure 17: The representation of the geometry and boundary conditions for the Example 3 in (a) Case 1, (b) Case 2, and (c) Case 3.

24. Another impacting factor that should be noted is that the concentration of lithium increases significantly near the tip of a crack in the electrode particle, primarily because the intense hydrostatic stresses in that region drive the diffusion of lithium towards the crack tip. These hydrostatic stresses (as shown in (86)) play a crucial role in promoting the diffusion of lithium, causing it to migrate towards the crack tip and accumulate there. Additionally, high concentration gradients result in high stresses which lead to the nucleation of new cracks. This is in line with the experimental observation reported in [96]. Also, the resulting lithiation for Case 1, and Case 2 are depicted in Figure 23 and Figure 24, for six deformation stages up to complete fatigue failure. The lithium concentration is presented with a slice through the middle of the electrode particle.

The presence of cracks significantly impairs the integrity and structure of the electrode particle, which significantly affects its functionality and overall performance. These cracks contribute to the degradation and destabilization of the electrode, potentially impeding its efficiency in various applications. Therefore, providing a mathematical framework and modeling the lithium diffusion-induced fatigue cracking is crucial for the further development of lithium-ion batteries and the improvement of their lifetime.

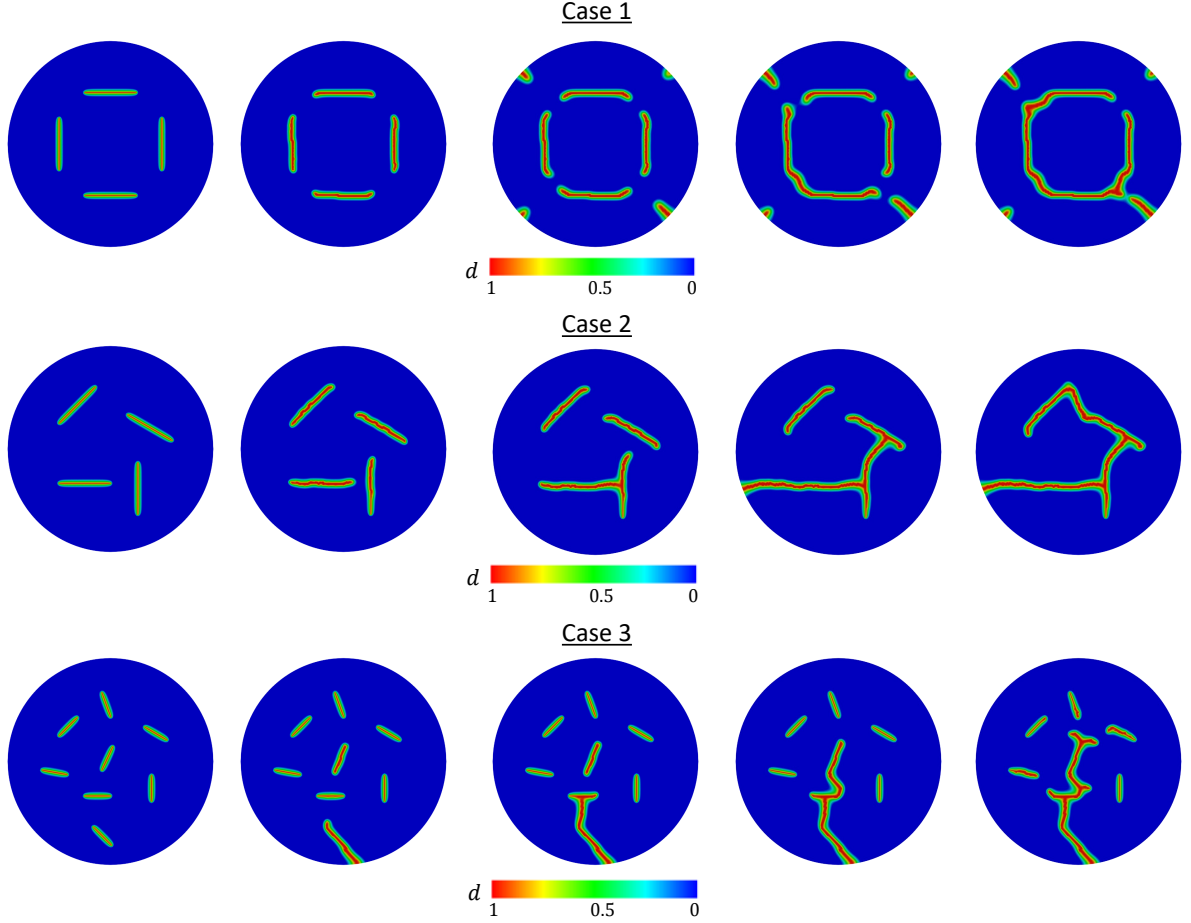


Figure 18: Example 3. Evolution of the crack phase-field in electrode particles for Case 1, 2 and 3.

3.4.1. Evaluation of using different multi-CPUs on computational time. The phase-field formulation of fracture is non-linear and calls for the resolution of small length scales. Its single-scale treatment is nowadays well-established and shown to be computationally demanding [102, 103, 104]. So, this type of regularized method (based on non-local theorem) usually requires large-scale computation, and parallel computing is particularly important at this time. In this manuscript, we have used multi-CPU sub regional computing in order to implement parallel computing. The Krylov Vectors are restarted after 30 iterations to prevent the accumulation of too many Krylov vectors, which can lead to storage issues. So, we take the BVP shown in Figure 22 to study the efficiency of parallel computing in fatigue degradation mechanisms for electrode particles. In this example, we have used for Case 1, 248 726, and for Case 2, 255 511 H_1 elements. To carry out parallel computation, we divided the whole geometry according to the number of CPUs. The mesh partitioning is shown in Figure 25 for Case 1, and correspondingly for Case 2 in Figure 26. According to [105] a rough guideline of 12 000 elements per CPU is given. The average number of GMRES iterations for solving the chemo-elasticity equation, i.e., $\Pi_u^\tau(\mathfrak{U}, \delta\mu) + \Pi_\mu^\tau(\mathfrak{U}, \delta\mu) = 0$ (see Algorithm 1) per Newton cycle for different states including linear region, fracture onset, fracture propagation, and fracture stabilization is shown in Table 3.

Additionally, the wall time of the model for different numbers of CPUs for Case 2

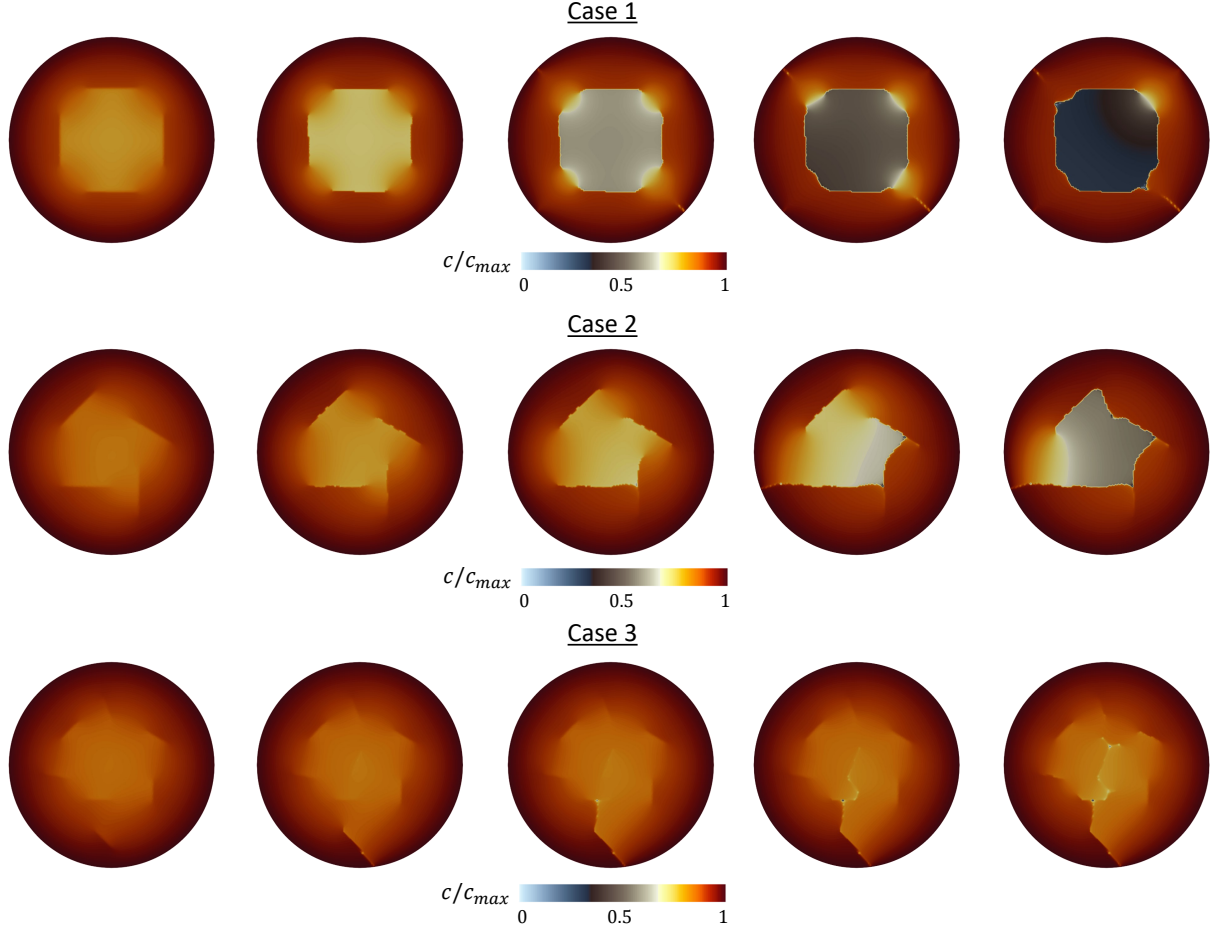


Figure 19: Example 3. Development of the lithium concentration in electrode particles for Case 1, 2 and 3.

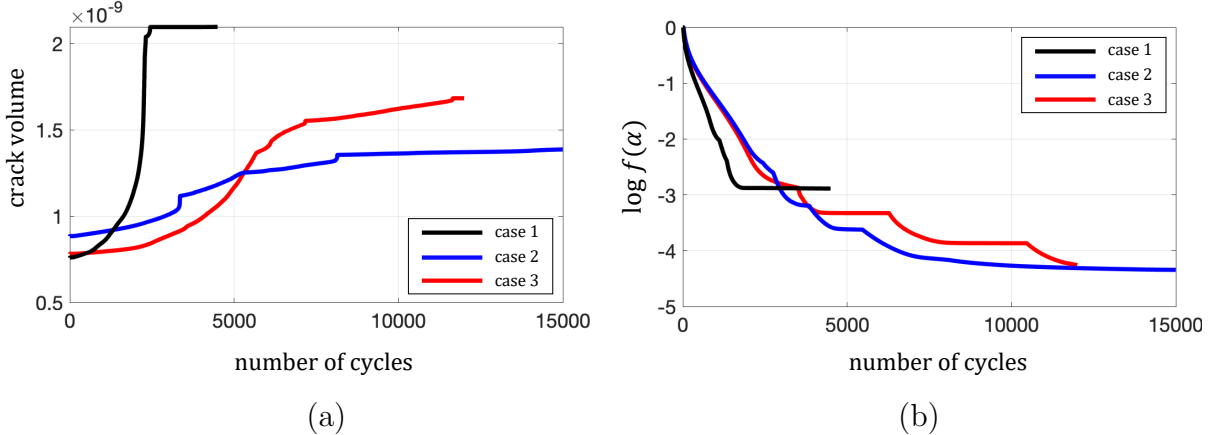


Figure 20: Example 3. Evaluation of (a) the crack volumes and (b) fatigue degradation functions for an arbitrary Gaussian integration point for Case 1, 2 and 3.

is further investigated, see Figure 27. Here we have accounted for 4 to 64 CPUs. Evidently, increasing the number of CPUs reduces the workload of each core, thus resulting in increased efficiency. Therefore, substantial time savings on CPU usage can be realized through efficient parallel computation and a well-defined solver. However, a more detailed

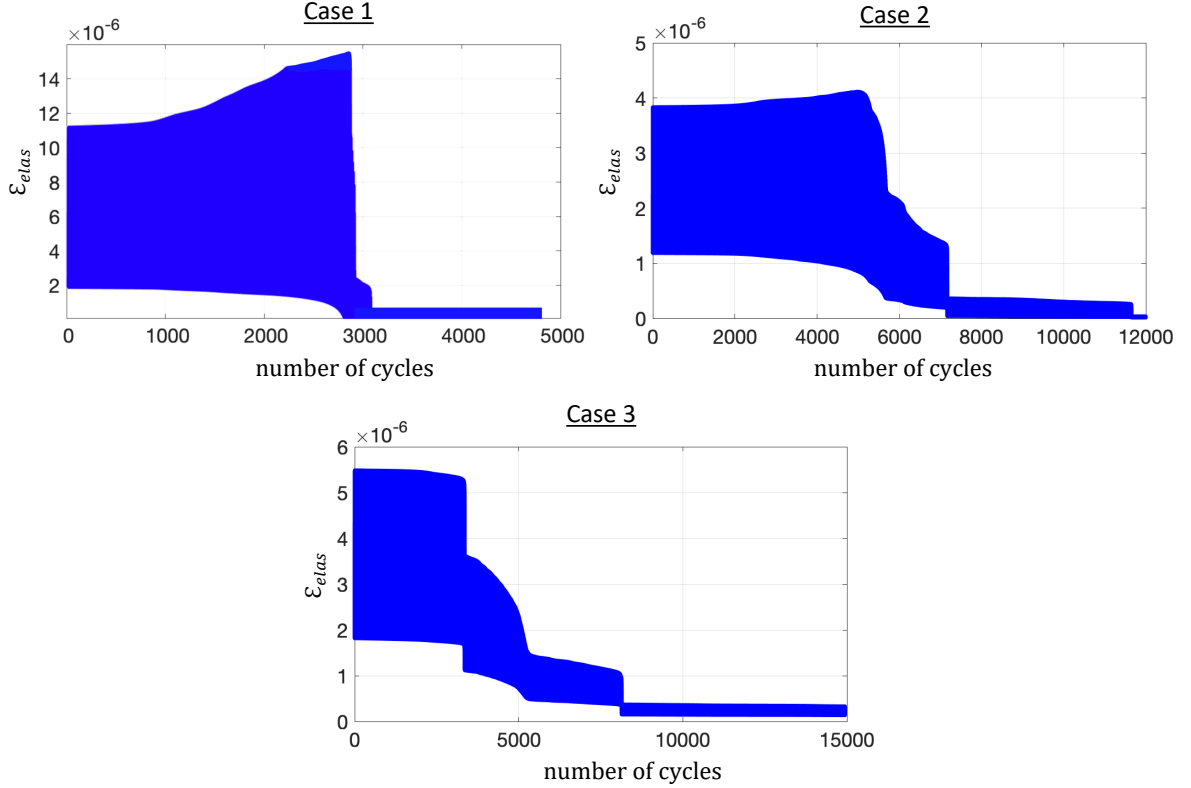


Figure 21: Example 3. The accumulated elastic energy functional for Case 1, 2 and 3.

exploration can be undertaken, particularly by employing distinct setups for the preconditioner, as it has been discussed in [106]. Almost the same behavior for Case 1 is also observed. Additionally, we note that using 64 CPUs slightly reduced the computational time, because of the needed time for the communication between different subdomains.

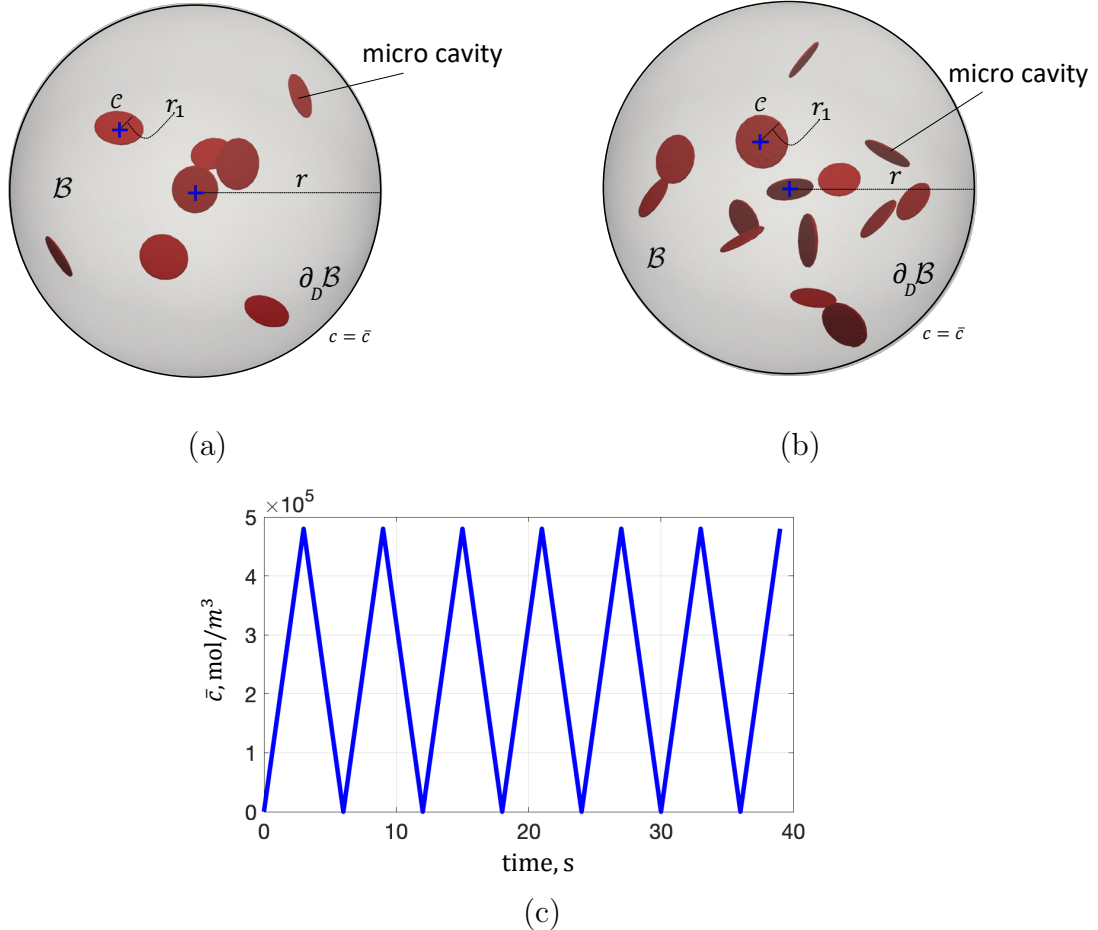


Figure 22: Example 4. The representation of the spherical electrode particle with geometry and boundary conditions for (a) Case 1 with 8, and (b) Case 2 with 14 randomly distributed micro cavities, whereas (c) cyclic lithiation/delithiation concentration load is imposed on electrode particle.

Table 3: Example 4. Average number of GMRES iterations for one Newton cycle for four different state of solving chemo-elasticity: $\Pi_u^\tau(\mathfrak{U}, \delta\mu) + \Pi_\mu^\tau(\mathfrak{U}, \delta\mu) = 0$, see Algorithm 1.

Time step	Case 1	Case 2
linear region	2	2
fracture onset	4	6
fracture propagation	6	10
fracture stabilization	4	5

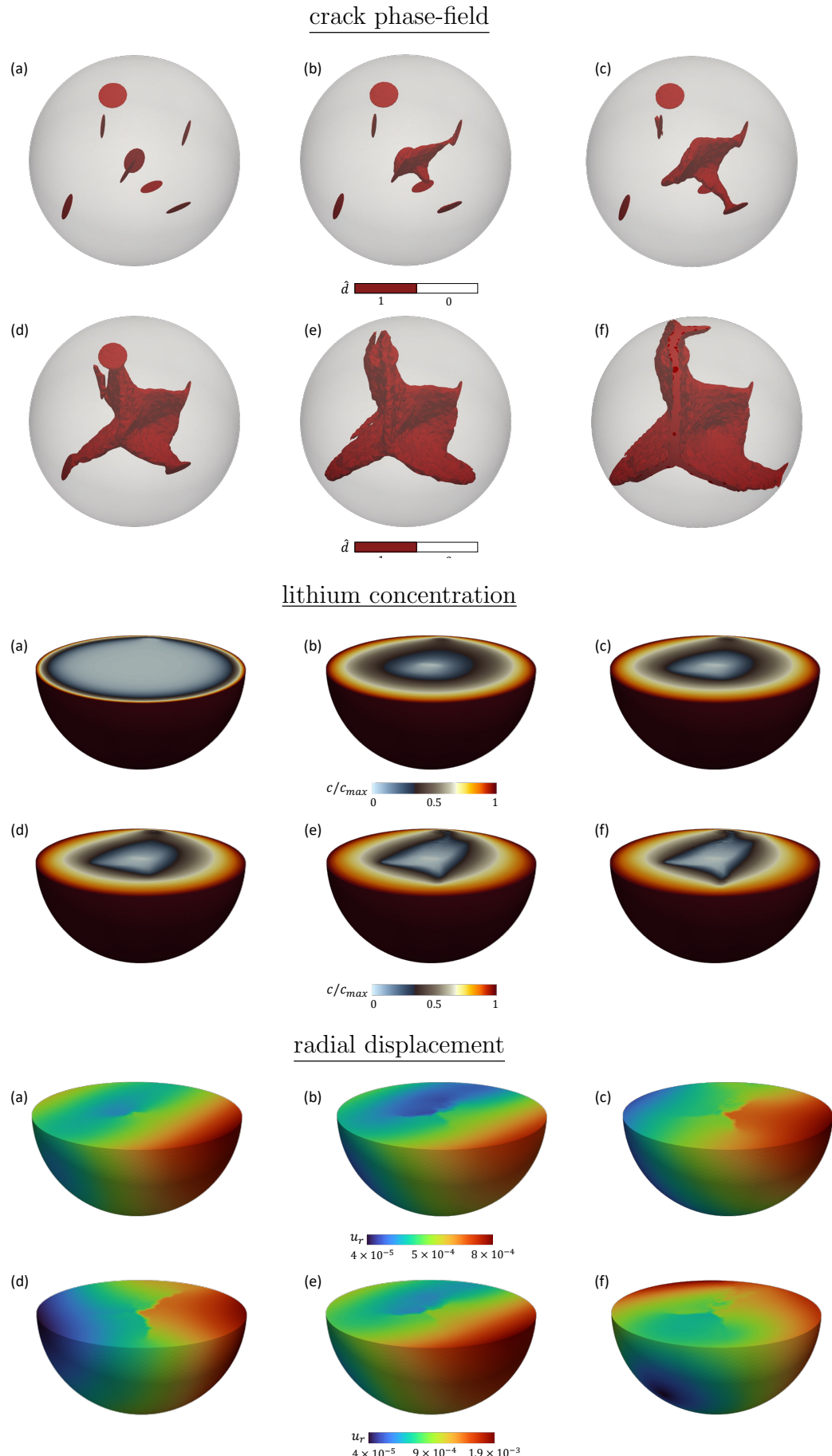


Figure 23: Example 4 (Case 1). Evaluation of the fracture pattern with crack isosurface evolution with $\{\hat{d} := 1 \text{ if } d \geq 0.99 \text{ otherwise } \hat{d} := 0\}$, normalized lithium concentration for six radial deformation from (a) nucleation, (b)-(e) fracture propagation, and (f) stabilization of the crack.

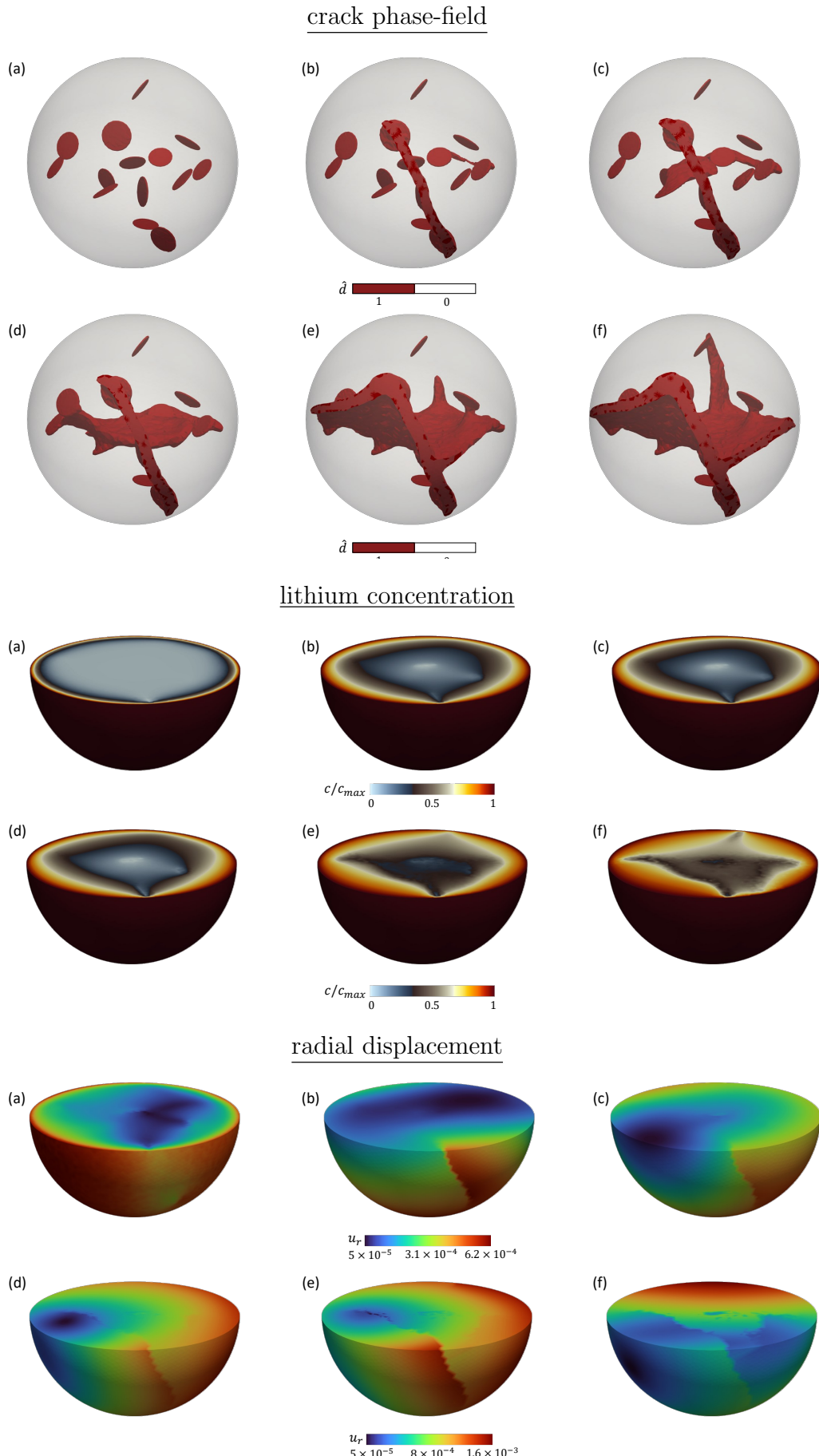


Figure 24: Example 4 (Case 2). Evaluation of the fracture pattern with crack isosurface evolution with $\{\hat{d} := 1 \text{ if } d \geq 0.99 \text{ otherwise } \hat{d} := 0\}$, normalized lithium concentration for six radial deformation from (a) nucleation, (b)-(e) fracture propagation, and (f) stabilization of the crack.

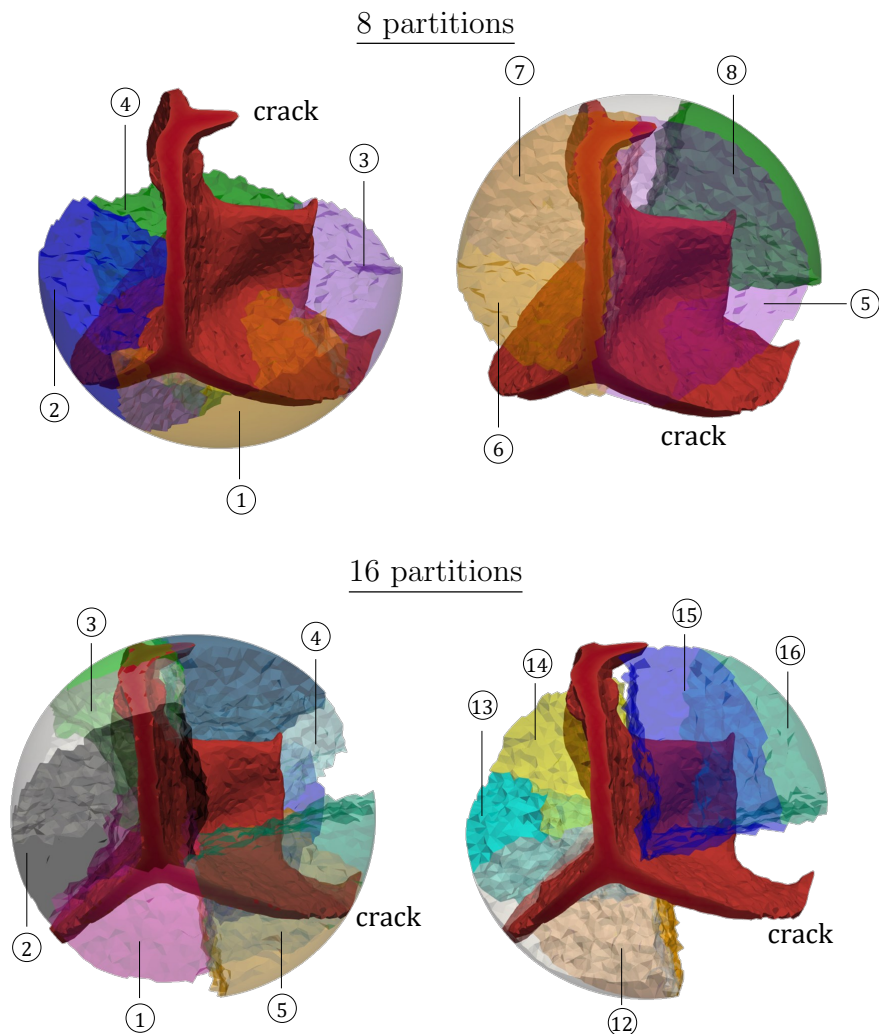


Figure 25: Example 4 (Case 1). The representation of the three-dimensional electrode particle with 8 randomly distributed micro cavitie in lithium-ion battery simulated with mesh partitioned for 8 cores (top side), and 16 cores (bottom side) for complete failure.

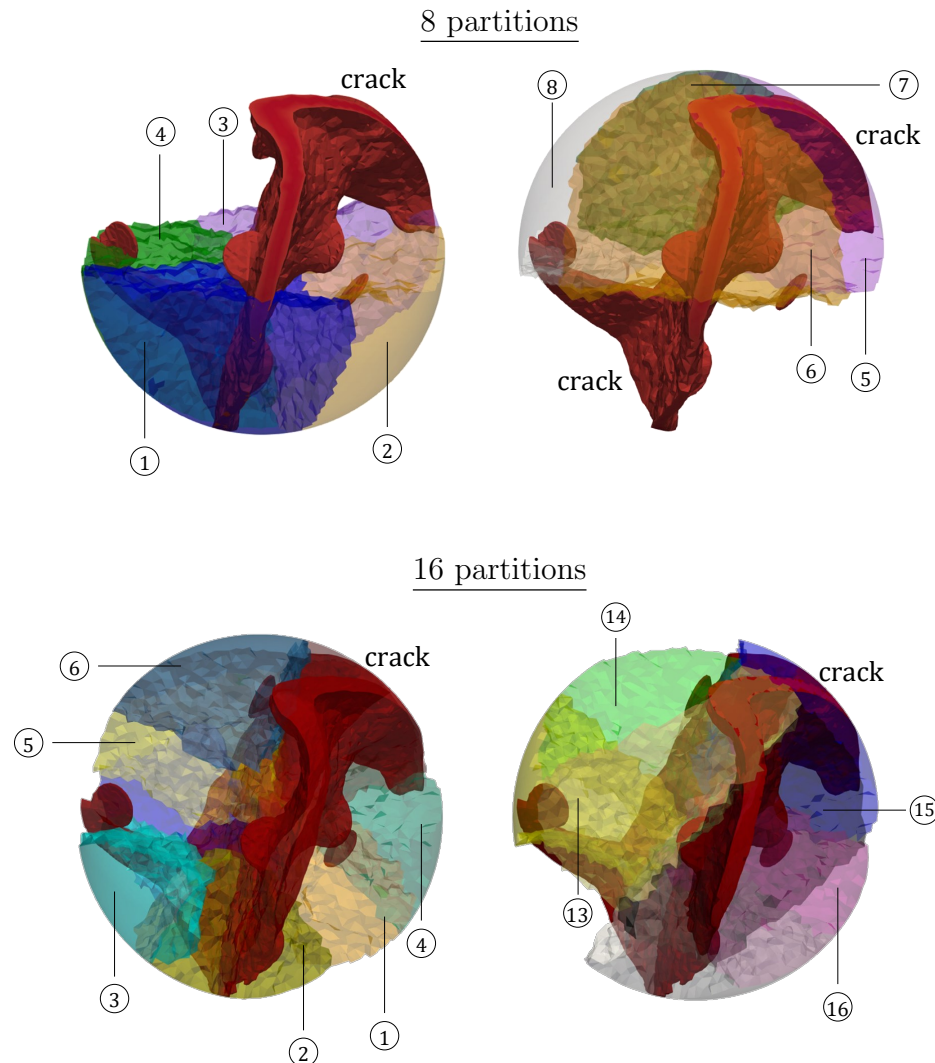


Figure 26: Example 4 (Case 2). The representation of the three-dimensional electrode particle with 14 randomly distributed micro cavities in lithium-ion battery simulated with mesh partitioned for 8 cores (top side), and 16 cores (bottom side) for complete failure.

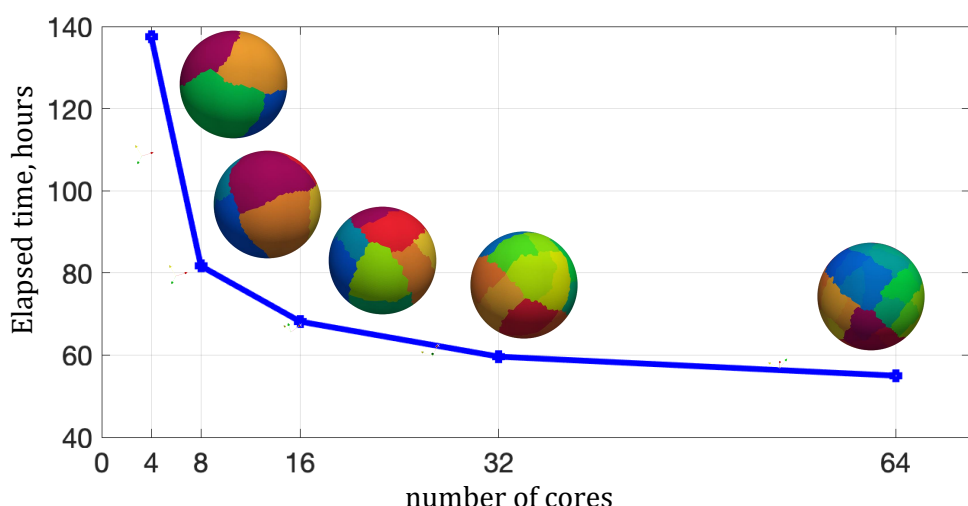


Figure 27: Example 4 (Case 2). Performance of parallel computing for different number of CPUs (cores) applied to the three-dimensional setting due to cyclic loading.

4. Conclusion

This study outlined a robust and rigorous mathematical formulation for fatigue failure theory in lithium-ion battery electrode particles for lithium diffusion induced fracture. Here, a variational formulation for cyclic charge and discharge processes, based on variational principles, rooted in incremental energy minimization, for gradient-extended dissipative solids has been established. The formulation has been derived to a coupled system of PDEs that governs the gradient-extended elastic-chemo damage response. To do so, the incremental energy, the incremental potential of the external load, the incremental dissipation potential for the lithium-ion diffusion and fracture are adopted for the incremental minimization principle. With this knowledge, we can estimate the degradation mechanism of the electrode particles and, thus, help *to enhance the fracture resistance of lithium-ion batteries.*

Here, four numerical examples with different boundary value problems including various test cases were presented to substantiate our algorithmic developments. Our main goal with these numerical examples is to investigate the effect of the random distribution of micro cavities (voids) and micro notches on the fracture resistance within electrode particle during lithiation/delithiation. It has been shown, that the radius of micro pores and also micro cavities results in different crack pattern. It has been found that the presence of cracks significantly impairs the integrity and structure of the electrode particle, significantly degrading its functionality and overall performance. These cracks contribute to the degradation and destabilization of the electrode, potentially impeding its efficiency in various applications. In addition, the influence of the geometric shape of the electrode particle, i.e. the longitudinal and transverse diameter ($\chi = D_{long}/D_{trans}$), on the complete failure was investigated. It has been found that with a reduction in χ , a higher number of cycles is required for complete fatigue, which can extend the lifetime of the batteries. Additionally, the storage elastic energy will be reduced by reducing the aspect ratio of geometrical shape of the electrode particle. Meanwhile, the concentration of lithium increases significantly near the tip of a crack in a electrode particle, primarily because the intense hydrostatic stresses in that region drive the diffusion of lithium towards the crack tip. So, in all the examples, it has been observed that the lithium concentration is highest near the crack zone. These hydrostatic stresses play a crucial role in promoting the diffusion of lithium so that it migrates to the vicinity of the crack tip and accumulates there. Additionally, high-concentration gradients result in high stresses which lead to the nucleation of new cracks. In conclusion, the proposed formulation improves our understanding of the fracture mechanics of lithium-ion battery electrodes and will provide valuable insights into the design of next-generation electrode structures.

Acknowledgment

A. Khodadadian acknowledges the support by FWF (Austrian Science Fund) Standalone Project No P-36520, entitled Using Single Atom Catalysts as Nanozymes in FET Sensors. Also, high performance computing was supported by the Leibniz Universität Hannover, the Lower Saxony Ministry of Science and Culture (MWK) and the German Research Association (DFG).

Appendix A. Derivation of the μ , and \mathbb{H}

The objective of this Appendix is to derive lithium chemical potential μ , and lithium-ion flux vector \mathbb{H} . Following the constitutive equation given in (15) or through the necessary condition of the variational principle given for Formulation 2.2, we have

$$\mu(\boldsymbol{\varepsilon}^e, c) \approx \mu(\boldsymbol{\varepsilon}, \boldsymbol{\varepsilon}^c, \Theta_L) := \frac{\partial W}{\partial c} = \frac{\partial W_{Li-ion}}{\partial c} + \frac{\partial W_{elas}}{\partial c}. \quad (\text{A.1})$$

Since, for a given scalar-valued function $f(c)$, the following derivative for the natural logarithm $[\ln(f(c))]' = f(c)'/f(c)$ holds, thus the first term in (A.1) results in:

$$\begin{aligned} \frac{\partial W_{Li-ion}}{\partial c} &= \left[\mu_0 c + R\vartheta N_L \left(\Theta_L \ln \Theta_L + (1 - \Theta_L) \ln(1 - \Theta_L) \right) \right]' \\ &= \mu_0 + R\vartheta N_L \left(\Theta'_L \ln \Theta_L + \Theta_L \ln \Theta'_L - \Theta'_L \ln(1 - \Theta_L) \right. \\ &\quad \left. + (1 - \Theta_L) \ln(1 - \Theta_L)' \right), \end{aligned} \quad (\text{A.2})$$

with the identity $\Theta_L = c/N_L$ such that $0 < \Theta_L \ll 1$, and $\Theta'_L = 1/N_L$, thus

$$\begin{aligned} \frac{\partial W_{Li-ion}}{\partial c} &= \mu_0 + R\vartheta N_L \left(\frac{1}{N_L} \ln \Theta_L + \Theta_L \frac{\frac{1}{N_L}}{\Theta_L} - \frac{1}{N_L} \ln(1 - \Theta_L) + (1 - \Theta_L) \frac{\frac{-1}{N_L}}{1 - \Theta_L} \right) \\ &= \mu_0 + R\vartheta \left(\ln \Theta_L + 1 - \ln(1 - \Theta_L) - 1 \right) \\ &= \mu_0 + R\vartheta \left(\ln \Theta_L - \ln(1 - \Theta_L) \right). \end{aligned} \quad (\text{A.3})$$

Next, to derive the elastic contribution of the lithium chemical potential that is the second term of the (A.1), we have:

$$\frac{\partial W_{elas}}{\partial c} = \frac{\partial W_{elas}}{\partial \boldsymbol{\varepsilon}_e} : \frac{\partial \boldsymbol{\varepsilon}_e}{\partial c} = -\boldsymbol{\sigma} : \frac{\Omega_c}{3} \mathbf{I} = -\Omega_c \sigma_h \quad \text{with} \quad \sigma_h = \frac{1}{3} \text{tr}(\boldsymbol{\sigma}), \quad (\text{A.4})$$

with $\boldsymbol{\sigma}$ given in (89). Thus, the lithium chemical potential μ reads:

$$\mu(\boldsymbol{\varepsilon}^e, c) = \frac{\partial W}{\partial c} = \mu_0 + R\vartheta \left(\ln \Theta_L - \ln(1 - \Theta_L) \right) - \Omega_c \sigma_h, \quad (\text{A.5})$$

that is (85), and our derivation is now completed.

Next, we aim to derive lithium-ion flux vector $\mathbb{H} := \mathbf{K}\mathbb{B}$. To do so, we need to derive the gradient of the lithium chemical potential μ , which results in:

$$\begin{aligned} \nabla \mu &= R\vartheta \nabla \left(\ln \Theta_L - \ln(1 - \Theta_L) \right) - \Omega_c \nabla \sigma_h = -R\vartheta \partial_{\mathbf{x}} \left(\ln \left(\frac{1}{\Theta_L} - 1 \right) \right) - \Omega_c \nabla \sigma_h \\ &= -R\vartheta \Theta_L \partial_{\mathbf{x}} \left(\frac{N_L}{c} - 1 \right) / (1 - \Theta_L) - \Omega_c \nabla \sigma_h \\ &= -\frac{R\vartheta \Theta_L}{1 - \Theta_L} \left(\frac{\partial_{\mathbf{x}} N_L \cdot c - \partial_{\mathbf{x}} c \cdot N_L}{c^2} \right) - \Omega_c \nabla \sigma_h \\ &= -\frac{R\vartheta}{1 - \Theta_L} \left(\frac{\partial_{\mathbf{x}} N_L \cdot c - \partial_{\mathbf{x}} c \cdot N_L}{c \cdot N_L} \right) - \Omega_c \nabla \sigma_h \\ &= \frac{R\vartheta}{1 - \Theta_L} \left(\frac{\partial_{\mathbf{x}} c}{c} - \frac{\partial_{\mathbf{x}} N_L}{N_L} \right) - \Omega_c \nabla \sigma_h. \end{aligned} \quad (\text{A.6})$$

We now impose gradient of the lithium chemical potential given in (A.6) to the lithium-ion flux vector \mathbb{H} along with isotropic concentration diffusivity tensor \mathbf{K} , that is:

$$\mathbb{H} = -\mathbf{K}(c, d) \nabla \mu \quad \text{and} \quad \mathbf{K}(c, d) = g(d) \frac{D}{R\vartheta} c \mathbf{I}, \quad (\text{A.7})$$

so, by assuming that $\nabla N_L = 0$ (see Section 2.3.2), finally we have the following:

$$\mathbb{H} = \mathbf{K}\mathbb{B} = -g(d)D\nabla c + \frac{g(d)D}{R\vartheta} c\Omega_c \nabla \sigma_h. \quad (\text{A.8})$$

that is (87), and our derivation is now completed.

References

- [1] Q. Wang, G. Zhang, Y. Li, Z. Hong, D. Wang, and S. Shi, “Application of phase-field method in rechargeable batteries,” *npj Computational Materials*, vol. 6, no. 1, p. 176, 2020.
- [2] P. Zuo and Y.-P. Zhao, “A phase field model coupling lithium diffusion and stress evolution with crack propagation and application in lithium ion batteries,” *Physical Chemistry Chemical Physics*, vol. 17, no. 1, pp. 287–297, 2015.
- [3] J.-H. Zhu, W.-H. Zhang, and L. Xia, “Topology optimization in aircraft and aerospace structures design,” *Archives of Computational Methods in Engineering*, vol. 23, no. 4, pp. 595–622, 2016.
- [4] N. Aage, E. Andreassen, B. S. Lazarov, and O. Sigmund, “Giga-voxel computational morphogenesis for structural design,” *Nature*, vol. 550, no. 7674, pp. 84–86, 2017.
- [5] S. Chu and A. Majumdar, “Opportunities and challenges for a sustainable energy future,” *nature*, vol. 488, no. 7411, pp. 294–303, 2012.
- [6] M. Armand, P. Axmann, D. Bresser, M. Copley, K. Edström, C. Ekberg, D. Guyomard, B. Lestriez, P. Novák, M. Petranikova, *et al.*, “Lithium-ion batteries—current state of the art and anticipated developments,” *Journal of Power Sources*, vol. 479, p. 228708, 2020.
- [7] C. P. Grey and D. S. Hall, “Prospects for lithium-ion batteries and beyond—a 2030 vision,” *Nature communications*, vol. 11, no. 1, p. 6279, 2020.
- [8] R. Korthauer, *Lithium-ion batteries: basics and applications*. Springer, 2018.
- [9] M. Wakihara and O. Yamamoto, *Lithium ion batteries: fundamentals and performance*. John Wiley & Sons, 2008.
- [10] C. Lin, A. Tang, H. Mu, W. Wang, C. Wang, *et al.*, “Aging mechanisms of electrode materials in lithium-ion batteries for electric vehicles,” *Journal of Chemistry*, vol. 2015, 2015.
- [11] R. Xu and K. Zhao, “Corrosive fracture of electrodes in li-ion batteries,” *Journal of the Mechanics and Physics of Solids*, vol. 121, pp. 258–280, 2018.
- [12] K. Zhao, M. Pharr, L. Hartle, J. J. Vlassak, and Z. Suo, “Fracture and debonding in lithium-ion batteries with electrodes of hollow core–shell nanostructures,” *Journal of Power Sources*, vol. 218, pp. 6–14, 2012.
- [13] M. R. Palacín and A. de Guibert, “Why do batteries fail?,” *Science*, vol. 351, no. 6273, p. 1253292, 2016.

- [14] N. Lin, Z. Jia, Z. Wang, H. Zhao, G. Ai, X. Song, Y. Bai, V. Battaglia, C. Sun, J. Qiao, *et al.*, “Understanding the crack formation of graphite particles in cycled commercial lithium-ion batteries by focused ion beam-scanning electron microscopy,” *Journal of power sources*, vol. 365, pp. 235–239, 2017.
- [15] H. Zheng, L. Zhang, G. Liu, X. Song, and V. S. Battaglia, “Correlationship between electrode mechanics and long-term cycling performance for graphite anode in lithium ion cells,” *Journal of Power Sources*, vol. 217, pp. 530–537, 2012.
- [16] S. Müller, P. Pietsch, B.-E. Brandt, P. Baade, V. De Andrade, F. De Carlo, and V. Wood, “Quantification and modeling of mechanical degradation in lithium-ion batteries based on nanoscale imaging,” *Nature communications*, vol. 9, no. 1, p. 2340, 2018.
- [17] S. Li, Z. Jiang, J. Han, Z. Xu, C. Wang, H. Huang, C. Yu, S.-J. Lee, P. Pianetta, H. Ohldag, *et al.*, “Mutual modulation between surface chemistry and bulk microstructure within secondary particles of nickel-rich layered oxides,” *Nature communications*, vol. 11, no. 1, p. 4433, 2020.
- [18] R. Xu, Y. Yang, F. Yin, P. Liu, P. Cloetens, Y. Liu, F. Lin, and K. Zhao, “Heterogeneous damage in li-ion batteries: Experimental analysis and theoretical modeling,” *Journal of the Mechanics and Physics of Solids*, vol. 129, pp. 160–183, 2019.
- [19] M. Makki, G. Ayoub, C. W. Lee, C. Bae, and X. Colin, “Effect of battery fast cyclic charging on the mechanical and fracture behavior of the lithium-ion battery separator,” *Polymer Degradation and Stability*, vol. 216, p. 110469, 2023.
- [20] W. Ai, B. Wu, and E. Martínez-Pañeda, “A coupled phase field formulation for modelling fatigue cracking in lithium-ion battery electrode particles,” *Journal of Power Sources*, vol. 544, p. 231805, 2022.
- [21] I. Laresgoiti, S. Käbitz, M. Ecker, and D. U. Sauer, “Modeling mechanical degradation in lithium ion batteries during cycling: Solid electrolyte interphase fracture,” *Journal of Power Sources*, vol. 300, pp. 112–122, 2015.
- [22] M. Liang, B. Luo, and L. Zhi, “Application of graphene and graphene-based materials in clean energy-related devices,” *International Journal of Energy Research*, vol. 33, no. 13, pp. 1161–1170, 2009.
- [23] S. N. Hapuarachchi, Z. Sun, and C. Yan, “Advances in in situ techniques for characterization of failure mechanisms of li-ion battery anodes,” *Advanced Sustainable Systems*, vol. 2, no. 8-9, p. 1700182, 2018.
- [24] T. Bernthaler, A. Kopp, A. Nagel, J. Niedermeier, G. Schneider, and F. Trier, “Microscopy analysis for green energy solutions,” *Microscopy*, 2022.
- [25] D.-S. Ko, J.-H. Park, S. Park, Y. N. Ham, S. J. Ahn, J.-H. Park, H. N. Han, E. Lee, W. S. Jeon, and C. Jung, “Microstructural visualization of compositional changes induced by transition metal dissolution in ni-rich layered cathode materials by high-resolution particle analysis,” *Nano energy*, vol. 56, pp. 434–442, 2019.
- [26] S. Xia, L. Mu, Z. Xu, J. Wang, C. Wei, L. Liu, P. Pianetta, K. Zhao, X. Yu, F. Lin, *et al.*, “Chemomechanical interplay of layered cathode materials undergoing fast charging in lithium batteries,” *Nano energy*, vol. 53, pp. 753–762, 2018.
- [27] Z. Zhu, A. Gao, Y. Liang, F. Yi, T. Meng, J. Ling, J. Hao, and D. Shu, “Dual-functional tungsten boosted lithium-ion diffusion and structural integrity of $\text{Li}_{10}\text{Ni}_{0.8}\text{Co}_{0.1}\text{Mn}_{0.1}\text{O}_2$ cathodes for high performance lithium-ion batteries,” *ACS Sustainable Chemistry & Engineering*, vol. 10, no. 1, pp. 50–60, 2021.
- [28] P. Teichert, G. G. Eshetu, H. Jahnke, and E. Figgemeier, “Degradation and aging routes of ni-rich cathode based li-ion batteries,” *Batteries*, vol. 6, no. 1, p. 8, 2020.

- [29] I. Ryu, J. W. Choi, Y. Cui, and W. D. Nix, “Size-dependent fracture of si nanowire battery anodes,” *Journal of the Mechanics and Physics of Solids*, vol. 59, no. 9, pp. 1717–1730, 2011.
- [30] X. Zhu, Y. Chen, H. Chen, and W. Luan, “The diffusion induced stress and cracking behaviour of primary particle for li-ion battery electrode,” *International Journal of Mechanical Sciences*, vol. 178, p. 105608, 2020.
- [31] B. Bourdin, G. A. Francfort, and J.-J. Marigo, “The variational approach to fracture,” *Journal of elasticity*, vol. 91, no. 1, pp. 5–148, 2008.
- [32] M. Ambati, T. Gerasimov, and L. De Lorenzis, “A review on phase-field models of brittle fracture and a new fast hybrid formulation,” *Computational Mechanics*, vol. 55, no. 2, pp. 383–405, 2015.
- [33] J.-Y. Wu, V. P. Nguyen, C. T. Nguyen, D. Sutula, S. Sinaie, and S. P. Bordas, “Chapter one - phase-field modeling of fracture,” vol. 53 of *Advances in Applied Mechanics*, pp. 1–183, Elsevier, 2020.
- [34] C. McAuliffe and H. Waisman, “A unified model for metal failure capturing shear banding and fracture,” *International Journal of Plasticity*, vol. 65, pp. 131–151, 2015.
- [35] G. Francfort and J.-J. Marigo, “Revisiting brittle fracture as an energy minimization problem,” *Journal of the Mechanics and Physics of Solids*, vol. 46, no. 8, pp. 1319–1342, 1998.
- [36] B. Bourdin, G. Francfort, and J.-J. Marigo, “Numerical experiments in revisited brittle fracture,” *Journal of the Mechanics and Physics of Solids*, vol. 48, no. 4, pp. 797–826, 2000.
- [37] B. Bourdin, J.-J. Marigo, C. Maurini, and P. Sicsic, “Morphogenesis and propagation of complex cracks induced by thermal shocks,” *Physical review letters*, vol. 112, no. 1, p. 014301, 2014.
- [38] C. Miehe, L.-M. Schaenzel, and H. Ulmer, “Phase field modeling of fracture in multi-physics problems. part i. balance of crack surface and failure criteria for brittle crack propagation in thermo-elastic solids,” *Computer Methods in Applied Mechanics and Engineering*, vol. 294, pp. 449–485, 2015.
- [39] C. Miehe, M. Hofacker, L.-M. Schänzel, and F. Aldakheel, “Phase field modeling of fracture in multi-physics problems. part ii. coupled brittle-to-ductile failure criteria and crack propagation in thermo-elastic-plastic solids,” *Computer Methods in Applied Mechanics and Engineering*, vol. 294, pp. 486–522, 2015.
- [40] L.-P. Yi, H. Waisman, Z.-Z. Yang, and X.-G. Li, “A consistent phase field model for hydraulic fracture propagation in poroelastic media,” *Computer Methods in Applied Mechanics and Engineering*, vol. 372, p. 113396, 2020.
- [41] M. F. Wheeler, T. Wick, and W. Wollner, “An augmented-lagrangian method for the phase-field approach for pressurized fractures,” *Computer Methods in Applied Mechanics and Engineering*, vol. 271, pp. 69–85, 2014.
- [42] T. Wick, S. Lee, and M. Wheeler, “3d phase-field for pressurized fracture propagation in heterogeneous media,” pp. 605–613, 2015.
- [43] T. Wick, “Goal functional evaluations for phase-field fracture using pu-based dwr mesh adaptivity,” *Computational Mechanics*, vol. 57, no. 6, pp. 1017–1035, 2016.
- [44] S. Lee, A. Mikelić, M. F. Wheeler, and T. Wick, “Phase-field modeling of proppant-filled fractures in a poroelastic medium,” *Computer Methods in Applied Mechanics and Engineering*, vol. 312, pp. 509–541, 2016.

- [45] A. Mikelić, M. F. Wheeler, and T. Wick, “A phase-field method for propagating fluid-filled fractures coupled to a surrounding porous medium,” *Multiscale Modeling & Simulation*, vol. 13, no. 1, pp. 367–398, 2015.
- [46] S. Lee, M. F. Wheeler, and T. Wick, “Pressure and fluid-driven fracture propagation in porous media using an adaptive finite element phase field model,” *Computer Methods in Applied Mechanics and Engineering*, vol. 305, pp. 111–132, 2016.
- [47] C. Miehe, S. Mauthe, and S. Teichtmeister, “Minimization principles for the coupled problem of darcy–biot-type fluid transport in porous media linked to phase field modeling of fracture,” *Journal of the Mechanics and Physics of Solids*, vol. 82, pp. 186–217, 2015.
- [48] C. Miehe and S. Mauthe, “Phase field modeling of fracture in multi-physics problems. part iii. crack driving forces in hydro-poro-elasticity and hydraulic fracturing of fluid-saturated porous media,” *Computer Methods in Applied Mechanics and Engineering*, vol. 304, pp. 619–655, 2016.
- [49] B. Markert and Y. Heider, “Coupled multi-field continuum methods for porous media fracture,” in *Recent Trends in Computational Engineering - CE2014* (M. Mehl, M. Bischoff, and M. Schäfer, eds.), vol. 105 of *Lecture Notes in Computational Science and Engineering*, pp. 167–180, Cham and Heidelberg and New York and Dordrecht and London: Springer, 2015.
- [50] Y. Heider and B. Markert, “A phase-field modeling approach of hydraulic fracture in saturated porous media,” *Mechanics Research Communications*, vol. 80, pp. 38–46, 2017.
- [51] Z. A. Wilson and C. M. Landis, “Phase-field modeling of hydraulic fracture,” *Journal of the Mechanics and Physics of Solids*, vol. 96, pp. 264–290, 2016.
- [52] M. J. Borden, C. V. Verhoosel, M. A. Scott, T. J. Hughes, and C. M. Landis, “A phase-field description of dynamic brittle fracture,” *Computer Methods in Applied Mechanics and Engineering*, vol. 217-220, pp. 77–95, 2012.
- [53] E. Tanné, T. Li, B. Bourdin, J.-J. Marigo, and C. Maurini, “Crack nucleation in variational phase-field models of brittle fracture,” *Journal of the Mechanics and Physics of Solids*, vol. 110, pp. 80–99, 2018.
- [54] A. Schlüter, A. Willenbücher, C. Kuhn, and R. Müller, “Phase field approximation of dynamic brittle fracture,” *Computational Mechanics*, vol. 54, no. 5, pp. 1141–1161, 2014.
- [55] J. Carlsson and P. Isaksson, “Dynamic crack propagation in wood fibre composites analysed by high speed photography and a dynamic phase field model,” *International Journal of Solids and Structures*, vol. 144-145, pp. 78–85, 2018.
- [56] M. Ambati and L. de Lorenzis, “Phase-field modeling of brittle and ductile fracture in shells with isogeometric nurbs-based solid-shell elements,” *Computer Methods in Applied Mechanics and Engineering*, vol. 312, pp. 351–373, 2016.
- [57] M. J. Borden, T. J. Hughes, C. M. Landis, A. Anvari, and I. J. Lee, “A phase-field formulation for fracture in ductile materials: Finite deformation balance law derivation, plastic degradation, and stress triaxiality effects,” *Computer Methods in Applied Mechanics and Engineering*, vol. 312, pp. 130–166, 2016.
- [58] C. McAuliffe and H. Waisman, “A coupled phase field shear band model for ductile–brittle transition in notched plate impacts,” *Computer Methods in Applied Mechanics and Engineering*, vol. 305, pp. 173–195, 2016.

- [59] P. Shanthraj, L. Sharma, B. Svendsen, F. Roters, and D. Raabe, “A phase field model for damage in elasto-viscoplastic materials,” *Computer Methods in Applied Mechanics and Engineering*, vol. 312, pp. 167–185, 2016.
- [60] V. P. Nguyen and J.-Y. Wu, “Modeling dynamic fracture of solids with a phase-field regularized cohesive zone model,” *Computer Methods in Applied Mechanics and Engineering*, vol. 340, pp. 1000–1022, 2018.
- [61] C. V. Verhoosel and R. de Borst, “A phase-field model for cohesive fracture,” *International Journal for Numerical Methods in Engineering*, vol. 96, no. 1, pp. 43–62, 2013.
- [62] J. Vignollet, S. May, R. de Borst, and C. V. Verhoosel, “Phase-field models for brittle and cohesive fracture,” *Mecanica*, vol. 49, no. 11, pp. 2587–2601, 2014.
- [63] Hirshikesh, S. Natarajan, and R. K. Annabattula, “Modeling crack propagation in variable stiffness composite laminates using the phase field method,” *Composite Structures*, vol. 209, pp. 424–433, 2019.
- [64] Hirshikesh, S. Natarajan, R. K. Annabattula, and E. Martínez-Pañeda, “Phase field modelling of crack propagation in functionally graded materials,” *Composites Part B: Engineering*, vol. 169, pp. 239–248, 2019.
- [65] K. Seleš, T. Lesičar, Z. Tonković, and J. Sorić, “A residual control staggered solution scheme for the phase-field modeling of brittle fracture,” *Engineering Fracture Mechanics*, vol. 205, pp. 370–386, 2019.
- [66] P. K. Kristensen and E. Martínez-Pañeda, “Phase field fracture modelling using quasi-newton methods and a new adaptive step scheme,” *Theoretical and Applied Fracture Mechanics*, vol. 107, p. 102446, 2020.
- [67] N. Noii, A. Khodadadian, J. Ulloa, F. Aldakheel, T. Wick, S. François, and P. Wriggers, “Bayesian inversion with open-source codes for various one-dimensional model problems in computational mechanics,” *Archives of Computational Methods in Engineering*, pp. 1–34, 2022.
- [68] Z. Khalil, A. Y. Elghazouli, and E. Martinez-Paneda, “A generalised phase field model for fatigue crack growth in elastic-plastic solids with an efficient monolithic solver,” *Computer Methods in Applied Mechanics and Engineering*, vol. 388, p. 114286, 2022.
- [69] Y. Navidtehrani, C. Betegón, and E. Martínez-Pañeda, “A simple and robust abaqus implementation of the phase field fracture method,” *Applications in Engineering Science*, vol. 6, p. 100050, 2021.
- [70] Y. Zhao, B.-X. Xu, P. Stein, and D. Gross, “Phase-field study of electrochemical reactions at exterior and interior interfaces in li-ion battery electrode particles,” *Computer Methods in Applied Mechanics and Engineering*, vol. 312, pp. 428–446, 2016.
- [71] X. Zhang, A. Krischok, and C. Linder, “A variational framework to model diffusion induced large plastic deformation and phase field fracture during initial two-phase lithiation of silicon electrodes,” *Computer methods in applied mechanics and engineering*, vol. 312, pp. 51–77, 2016.
- [72] B.-X. Xu, Y. Zhao, and P. Stein, “Phase field modeling of electrochemically induced fracture in li-ion battery with large deformation and phase segregation,” *GAMM-Mitteilungen*, vol. 39, no. 1, pp. 92–109, 2016.
- [73] S. Rezaei, J. N. Okoe-Amon, C. A. Varkey, A. Asheri, H. Ruan, and B.-X. Xu, “A cohesive phase-field fracture model for chemo-mechanical environments: Studies on degradation in battery materials,” *Theoretical and Applied Fracture Mechanics*, vol. 124, p. 103758, 2023.

- [74] C. Miehe, M. Hofacker, L.-M. Schänzel, and F. Aldakheel, “Phase field modeling of fracture in multi-physics problems. Part II. brittle-to-ductile failure mode transition and crack propagation in thermo-elastic-plastic solids,” *Computer Methods in Applied Mechanics and Engineering*, vol. 294, pp. 486–522, 2015.
- [75] B. Halphen and Q. Nguyen, “Generalized standard materials,” *Journal de Mécanique*, vol. 14, no. 1, pp. 39–63, 1975.
- [76] G. Maugin, “Infernal variables and dissipative structures,” *Journal of Non-Equilibrium Thermodynamics*, vol. 15, no. 2, pp. 173–192, 1990.
- [77] M. E. Gurtin and B. D. Reddy, “Alternative formulations of isotropic hardening for mises materials, and associated variational inequalities,” *Continuum Mechanics and Thermodynamics*, vol. 21, pp. 237–250, 2009.
- [78] A. Khodadadian, N. Noii, M. Parvizi, M. Abbaszadeh, T. Wick, and C. Heitzinger, “A bayesian estimation method for variational phase-field fracture problems,” *Computational Mechanics*, vol. 66, no. 4, pp. 827–849, 2020.
- [79] Q. Wang, Y. Feng, W. Zhou, Y. Cheng, and G. Ma, “A phase-field model for mixed-mode fracture based on a unified tensile fracture criterion,” *Computer Methods in Applied Mechanics and Engineering*, vol. 370, p. 113270, 2020.
- [80] Q. Wang, Q. Yue, W. Zhou, Y. Feng, and X. Chang, “Modeling of both tensional-shear and compressive-shear fractures by a unified phase-field model,” *Applied Mathematical Modelling*, vol. 117, pp. 162–196, 2023.
- [81] M. Fan, Y. Jin, and T. Wick, “A quasi-monolithic phase-field description for mixed-mode fracture using predictor–corrector mesh adaptivity,” *Engineering with Computers*, vol. 38, no. Suppl 4, pp. 2879–2903, 2022.
- [82] L. Anand, “2014 drucker medal paper: A derivation of the theory of linear poroelasticity from chemoelasticity,” *Journal of Applied Mechanics*, vol. 82, no. 11, p. 111005, 2015.
- [83] J. Ågren, “The onsager reciprocity relations revisited,” *Journal of Phase Equilibria and Diffusion*, vol. 43, no. 6, pp. 640–647, 2022.
- [84] C. V. Di Leo and L. Anand, “Hydrogen in metals: a coupled theory for species diffusion and large elastic–plastic deformations,” *International Journal of Plasticity*, vol. 43, pp. 42–69, 2013.
- [85] E. Martínez-Pañeda, A. Golahmar, and C. F. Niordson, “A phase field formulation for hydrogen assisted cracking,” *Computer Methods in Applied Mechanics and Engineering*, vol. 342, pp. 742–761, 2018.
- [86] P. Sofronis and R. M. McMeeking, “Numerical analysis of hydrogen transport near a blunting crack tip,” *Journal of the Mechanics and Physics of Solids*, vol. 37, no. 3, pp. 317–350, 1989.
- [87] F. Aldakheel, *Mechanics of Nonlocal Dissipative Solids: Gradient Plasticity and Phase Field Modeling of Ductile Fracture*. PhD thesis, Institute of Applied Mechanics (CE), Chair I, University of Stuttgart, 2016. <http://dx.doi.org/10.18419/opus-8803>.
- [88] C. Kuhn, A. Schlüter, and R. Müller, “On degradation functions in phase field fracture models,” *Computational Materials Science*, vol. 108, pp. 374–384, 2015.
- [89] J.-Y. Wu, “A unified phase-field theory for the mechanics of damage and quasi-brittle failure,” *Journal of the Mechanics and Physics of Solids*, vol. 103, pp. 72–99, 2017.

- [90] J.-Y. Wu, V. Nguyen, C. Nguyen, D. Sutula, S. Bordas, and S. Sinaie, “Phase field modeling of fracture,” *Advances in Applied Mechanics: Multi-Scale Theory and Computation*, vol. 52, 2018.
- [91] N. Noii and T. Wick, “A phase-field description for pressurized and non-isothermal propagating fractures,” *Computer Methods in Applied Mechanics and Engineering*, vol. 351, pp. 860 – 890, 2019.
- [92] C. Miehe, “A multi-field incremental variational framework for gradient-extended standard dissipative solids,” *Journal of the Mechanics and Physics of Solids*, vol. 59, no. 4, pp. 898–923, 2011.
- [93] S. A. Mauthe, *Variational multiphysics modeling of diffusion in elastic solids and hydraulic fracturing in porous media*. Stuttgart: Institut fur Mechanik (Bauwesen), 2017.
- [94] P. Carrara, M. Ambati, R. Alessi, and L. De Lorenzis, “A framework to model the fatigue behavior of brittle materials based on a variational phase-field approach,” *Computer Methods in Applied Mechanics and Engineering*, vol. 361, p. 112731, 2020.
- [95] L. Böger, M.-A. Keip, and C. Miehe, “Minimization and saddle-point principles for the phase-field modeling of fracture in hydrogels,” *Computational Materials Science*, vol. 138, pp. 474–485, 2017.
- [96] A. Bagheri, J. Arghavani, and R. Naghdabadi, “On the effects of hydrostatic stress on li diffusion kinetics and stresses in spherical active particles of li-ion battery electrodes,” *Mechanics of Materials*, vol. 137, p. 103134, 2019.
- [97] N. Noii, A. Khodadadian, J. Ulloa, F. Aldakheel, T. Wick, S. François, and P. Wriggers, “Bayesian inversion for unified ductile phase-field fracture,” *Computational Mechanics*, vol. 68, no. 4, pp. 943–980, 2021.
- [98] N. Noii, M. Fan, T. Wick, and Y. Jin, “A quasi-monolithic phase-field description for orthotropic anisotropic fracture with adaptive mesh refinement and primal–dual active set method,” *Engineering Fracture Mechanics*, vol. 258, p. 108060, 2021.
- [99] N. Noii and T. Wick, “A phase-field description for pressurized and non-isothermal propagating fractures,” *Computer Methods in Applied Mechanics and Engineering*, vol. 351, pp. 860–890, 2019.
- [100] J. ne Zeller, J.-P. D. M. Kuhn, J. Saak, and M. Blesel, “Performance analysis of mpi-based fenics/petsc models in pymor,” 2021.
- [101] J. M. Maljaars, C. N. Richardson, and N. Sime, “Leopard: A particle library for fenics,” *Computers & Mathematics with Applications*, vol. 81, pp. 289–315, 2021.
- [102] T. Gerasimov and L. De Lorenzis, “A line search assisted monolithic approach for phase-field computing of brittle fracture,” *Computer Methods in Applied Mechanics and Engineering*, vol. 312, pp. 276–303, 2016.
- [103] T. Wang, X. Ye, Z. Liu, D. Chu, and Z. Zhuang, “Modeling the dynamic and quasi-static compression-shear failure of brittle materials by explicit phase field method,” *Computational Mechanics*, vol. 64, pp. 1537–1556, 2019.
- [104] P. Farrell and C. Maurini, “Linear and nonlinear solvers for variational phase-field models of brittle fracture,” *International Journal for Numerical Methods in Engineering*, vol. 109, no. 5, pp. 648–667, 2017.
- [105] A. Hamzehloo, M. Bahlali, P. Salinas, C. Jacquemyn, C. Pain, A. Butler, and M. Jackson, “Modelling saline intrusion using dynamic mesh optimization with parallel processing,” *Advances in Water Resources*, vol. 164, p. 104189, 2022.

- [106] L. Svolos, L. Berger-Vergiat, and H. Waisman, “Updating strategy of a domain decomposition preconditioner for parallel solution of dynamic fracture problems,” *Journal of Computational Physics*, vol. 422, p. 109746, 2020.